WATER SPLITTING ELECTROCATALYSTS IN ACIDIC MEDIA: IN THE SEARCH OF NON-NOBLE METAL ALTERNATIVES

Jiahao Yu

ADVERTIMENT. L'accés als continguts d'aquesta tesi doctoral i la seva utilització ha de respectar els drets de la persona autora. Pot ser utilitzada per a consulta o estudi personal, així com en activitats o materials d'investigació i docència en els termes establerts a l'art. 32 del Text Refós de la Llei de Propietat Intel·lectual (RDL 1/1996). Per altres utilitzacions es requereix l'autorització prèvia i expressa de la persona autora. En qualsevol cas, en la utilització dels seus continguts caldrà indicar de forma clara el nom i cognoms de la persona autora i el títol de la tesi doctoral. No s'autoritza la seva reproducció o altres formes d'explotació efectuades amb finalitats de lucre ni la seva comunicació pública des d'un lloc aliè al servei TDX. Tampoc s'autoritza la presentació del seu contingut en una finestra o marc aliè a TDX (framing). Aquesta reserva de drets afecta tant als continguts de la tesi com als seus resums i índexs.

ADVERTENCIA. El acceso a los contenidos de esta tesis doctoral y su utilización debe respetar los derechos de la persona autora. Puede ser utilizada para consulta o estudio personal, así como en actividades o materiales de investigación y docencia en los términos establecidos en el art. 32 del Texto Refundido de la Ley de Propiedad Intelectual (RDL 1/1996). Para otros usos se requiere la autorización previa y expresa de la persona autora. En cualquier caso, en la utilización de sus contenidos se deberá indicar de forma clara el nombre y apellidos de la persona autora y el título de la tesis doctoral. No se autoriza su reproducción u otras formas de explotación efectuadas con fines lucrativos ni su comunicación pública desde un sitio ajeno al servicio TDR. Tampoco se autoriza la presentación de su contenido en una ventana o marco ajeno a TDR (framing). Esta reserva de derechos afecta tanto al contenido de la tesis como a sus resúmenes e índices.

WARNING. Access to the contents of this doctoral thesis and its use must respect the rights of the author. It can be used for reference or private study, as well as research and learning activities or materials in the terms established by the 32nd article of the Spanish Consolidated Copyright Act (RDL 1/1996). Express and previous authorization of the author is required for any other uses. In any case, when using its content, full name of the author and title of the thesis must be clearly indicated. Reproduction or other forms of for profit use or public communication from outside TDX service is not allowed. Presentation of its content in a window or frame external to TDX (framing) is not authorized either. These rights affect both the content of the thesis and its abstracts and indexes.

UNIVERSITAT ROVIRA i VIRGILI

Water Splitting Electrocatalysts in Acidic Media: in the Search of Non-noble Metal Alternatives

JIAHAO YU

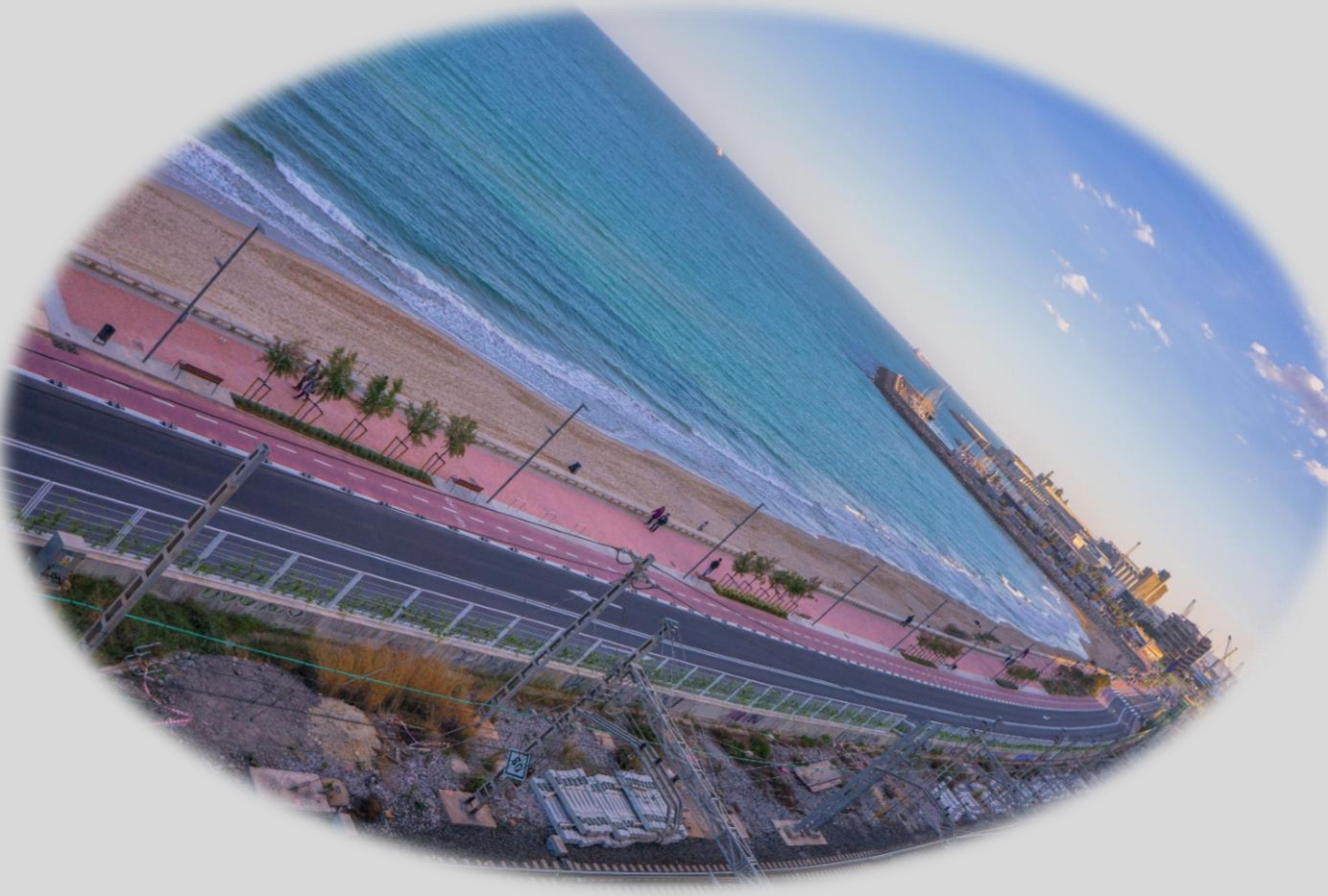

DOCTORAL THESIS

2023

DOCTORAL THESIS

Water Splitting Electrocatalysts in Acidic Media: in the Search of Non-noble Metal Alternatives

JIAHAO YU

Supervised by

Prof. Dr. José Ramón Galán Mascarós

Dr. Felipe Andrés Garcés Pineda

Tarragona, 2023

UNIVERSITAT ROVIRA i VIRGILI

ICIQ
Institute of Chemical Research of Catalonia

UNIVERSITAT ROVIRA i VIRGILI

ICIQ Institute of Chemical Research of Catalonia

Prof. Dr. José Ramón Galán Mascarós as Research Professor of Catalan Institution for Research and Advanced Studies (ICREA) and group Leader at the Institute of Chemical Research of Catalonia (ICIQ), and Dr. Felipe Andrés Garcés Pineda,

STATE that the present study, entitled "***Water Splitting Electrocatalysts in Acidic Media: in the Search of Non-noble Metal Alternatives***", presented by **Jiahao Yu** for the award of the degree of Doctor, has been carried out under supervision at Institute of Chemical Research of Catalonia (ICIQ) and the Department Chemical Science and Technology of this university, and that it fulfils all the requirements for an International Doctorate Mention.

Tarragona, 2023/01/30

Doctoral Thesis Supervisors:

Prof. José Ramón Galán Mascarós **Dr. Felipe Andrés Garcés Pineda**

“山穷水尽疑无路，柳暗花明又一村”

-陆游

“After endless mountains and rivers that leave doubt whether there is a path out, suddenly one encounters the shade of a willow, bright flowers and a lovely village”

In the spring of 1167

Acknowledgments

I told myself to be humble since I was a child, learning and waiting for growing up. But in an unlikely humble way, this genuine part will start with thanking myself, who made the right decision on this amazing 4-year journey. Surly it is not a matter of how many challenges I have overcome or how much feeling of self-satisfaction at the end of this journey but how much I have felt what you have delivered to me through the whole journey, to be a better man and then a good scientist.

Contradictory persons like me have opposite attitudes towards the same things. I hate autumn. This season took me 10000 kilometers away from my lovely hometown, Wuhan where Yangtze River brought me up, South Lake made my most friendships, East Lake started my career and Qingling Lake gave us another home. It was an afternoon and I thought I wouldn't shed a tear in the airport. When the separation came, I had to leave this beloved city and my harbor home. I cried when realizing that I would be literally far from my parents who gives the most supports and love in any condition, wouldn't have their shoulders and smiles often, couldn't enjoy mom's cooking and dad's driving. "*When the night has come, and the land is dark, and the moon is the only light we'll see. No, I won't be afraid. No, I won't be afraid just as long as you stand, stand by me*." 父母是山是海，是我永远的港湾。

Meanwhile, I love autumn. I like autumn most among four seasons when the land is sprinkled with golden yellow and the light glittering on the water. In the same season, the flight to Barcelona led me to a totally new world in which there is a sea called Mediterranean, a country named España and surrounding around are warm Spanish people. Before arriving here, I already could feel from the emails his being amiable and mannered. More than a supervisor helping your researching patiently, he is like a father, giving his children enough freedom to fly and holding them with good heart and encouragements when they fall down. There are endless thanks to JR (Prof. José Ramón Galán-Mascarós) for providing me this excellent platform to play and I am really enjoying. Although Felipe (Dr. Felipe Andrés Garcés Pineda) is my skillful co-supervisor with "magic hands" officially, I prefer to regarding him as my big bro. I don't have any brother or sister but he has

shown me what the brotherhood is, and how sincerely I am treated and cared as a little bro. I am sure this friendship between us will go through all my life. Please tell my love to your family too. In addition, I'd like to thank my big sister, Dr. Bahareh Khezri who has contributed a lot to my thesis as well. We both come from Asian countries so it seems we have similar characters and habits towards working at least. I admire your great kindness and manners like the flower fragrances filling the whole Girona in spring. Besides, I want to express my great gratitudes to every alumnus in this big family: Lijuan, Jesús, Mabel, David, Andrea, Irene, Álvaro, Breogán, Khalid, Juanjo, Franziska who even left, the current members: Vanesa, Stefano, Scott, llario, Lore, Santiago, Neus, Ulunay, Irene, Raiana and our sister group members: Katherine, Xiaojiao, Andres, Rebeca.

ICIQ is a great research center and community with fantastic people and strong function departments, such as excellent research supporting units, efficient logistics department etc. Without them, doing research would be more difficult and time-consuming. Also, the staffs in the Area of Microscopy and Nanometric Techniques of URV are very helpful in characterizations. Apart from the surrounding departments, our friends Prof. Jordi Arbiol from Barcelona, Prof. Sara Barja from San Sebastián and Prof. Sixto Gimenez Julia from Castelló are the masters in their regions. I would like to thank them for providing the effective tools to better understand how my catalyst works and am looking forward to a gathering together. Besides, I want to show my gratitude to Prof. Marc Koper from Leiden for hosting my 3-month stay funded by ICIQ-Severo Ochoa international mobility grant and opening a new gate for my research.

尽管远在数十万里的中国，那些我最亲近的朋友们也总能给予极大的支持。“相知无远近,万里尚为邻。”感谢思旭，卓彦，俊，禹，航军，彦。

感谢祖国，感谢中国留学基金委。我为身为一名中国人而感到自豪。

Please forgive me that I cannot express how greatly I am thankful to all of you in a word and allow me to speak it out when we meet.

Table of Contents

Summary

Hydrogen Economy" is a most promising option to support the penetration and consolidation of renewable energy sources including wind, solar etc., as a clean alternative to fossil fuels. In addition, Proton Exchange Membrane (PEM) electrolysis is a commercially mature and sustainable technology for hydrogen production in acid but the lack of non-noble metal-based materials on both anode and cathode hinders its application in a large scale. Therefore, to search for efficient electrocatalysts for hydrogen evolution and oxygen evolution working in acid is of great importance and urgency.

Proton-rich surrounding is favorable for hydrogen evolution reaction on the cathode, we firstly developed a new technique for creating a novel hybrid nanocomposite that include POM nanoparticles on 2D MXene nanosheets. Representatively, as-prepared Co_9-POM/Ti_3C_2 exhibited excellent HER electrocatalytic performance in 0.5 M H_2SO_4 solution with much higher activity compared with Ti_3C_2 MXene and good stability for a long time. It opens an avenue for designing a highly efficient and durable non-precious-metal HER electrocatalysts in acidic medium with unique heterostructures.

On the other hand, acidic oxygen evolution on the anode is a serious challenge for OER catalysts working under high potential, which leads to deactivation and dissolution. Both to keep the high activity of a catalyst and stabilize its performance in acid, we present a promising processing protocol, which combines in one single anode two powerful strategies: the incorporation of a nanostructured MOF-derived OER catalyst (Co_3O_4@C) from earth-abundant metals to maximize active surface area, and using a conducting, partially hydrophobic binder as the support made from paraffin oil and graphite powder for protection. This protocol delivers robust anodes that exhibit excellent acidic OER performances. Along with this viable and efficient strategy, an extensive survey of the activity and stability of monometallic, binary and ternary earth-abundant transition metal oxides based on earth abundant elements (Mn, Fe, Co, Ni, Zn) have also been conducted during electrocatalytic OER in strongly acidic conditions. Our results confirm the general validity of the strategy in using a partially hydrophobic electrode to confer high stability to common metal oxides

under these harsh conditions and open an alternative venue towards fast, energy efficient acid-media water oxidation electrodes.

These comprehensive and interesting findings would be helpful in the exploitation of earth-abundant electrocatalysts for acidic water splitting.

List of Publication

Yu, J., Garcés-Pineda, F.A., González-Cobos, J. *et al.* Sustainable oxygen evolution electrocatalysis in aqueous 1 M H_2SO_4 with earth abundant nanostructured Co_3O_4. *Nat. Commun.* **13**, 4341 (2022). https://doi.org/10.1038/s41467-022-32024-6

Abbreviations

Proton Exchange Membrane (PEM)

Anion Exchange Membrane (AEM)

Standard Hydrogen Electrode (SHE)

Reversible Hydrogen Electrode (RHE)

Hydrogen Evolution Reaction (HER)

Oxygen Evolution Reaction (OER)

Rate Determining Step (RDS)

Overpotential (η)

Onset Overpotential (η_{onset})

Thermodynamic Equilibrium Potential (E^0)

Current Density (j)

Temperature (T)

ChargeTransfer Coefficient (α)

Ideal Gas Constant (R)

Faraday Constant (F)

Electrochemical Impedance Spectroscopy (EIS)

Cyclic Voltammetry (CV)

Linear Sweep Voltammetry (LSV)

Accelerated Degradation Testing (ADT)

Faraday Efficiency (FE)

Oxygen Reduction Reaction (ORR)

Turnover Frequency (TOF)

Electrochemical Surface Area (ECSA)

Electrochemical Double-layer Capacitance (EDLC)

Stability number (S-number)

Activity-Stability Factor (ASF)

Fluorine-doped Tin Oxide (FTO)

Density Functional Theory (DFT)

Reduced GrapheneOxide (RGO)

Glassy Carbon (GC)

Polyoxometalate (POM)

Powder X-ray Diffraction (PXRD)

Scanning Electron Microscopy (SEM)

Transmission Electron Microscopy (SEM)

X-ray Photoelectron Spectrum (XPS)

High Resolution Transmission Electron Microscopy (HRTEM)

Scanning Transmission Electron Microscopy (STEM)

High Angle Annular Dark Field (HAADF)

Electron Energy Loss Spectroscopy in Scanning TEM mode (EELS-STEM)

Inductively Coupled Plasma Optical Emission Spectrometer (ICP-OES)

Ohmic Drop (R)

Current Interrupt (CI)

Open Circuit Potential (OCP)

Chapter 1. General introduction

1.1. Environmental issues

Since an unprecedentedly great economic booming in the Third Industrial Revolution, the global total population reached 3 billion mark in 1960 and was keeping growing in an approximate rate of ~80 million per year (Figure 1.1a). From United Nations department of Economic and Social Affairs, this number has overpassed 8 billion since the end of 2022.

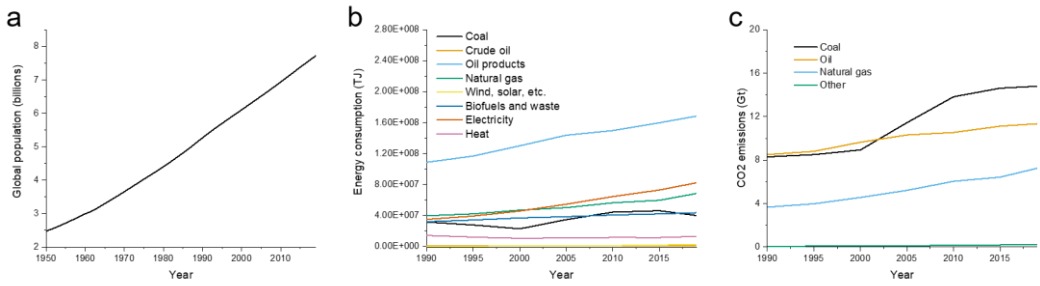

Figure 1.1. (a) Population growth in 1950-2019[1]; World energy consumption (b) and CO_2 emission (c) by energy source in the period 1990-2019[2].

To sustain the normal life of huge amount of populations, energy demand has seen great leaps yearly and corresponding, energy supply has become a critical and challenging issue for modern human development. As shown in figure 1.1b, in the 20 years between 1990 to 2019, global energy consumptions from oil products, electricity, natural gas, coal, biofuels and waste showed evidently yearly growth. Remarkably, from 109 million TJ in 1990, the energy consumption from oil products reached 168 million TJ in 2019, which was double of electricity consumption in the same year. However, the utilization of renewable energy source, wind, solar etc., was quite limited in very low level to contribute to increasing world energy demand.

The previous figure clearly implied the huge dependence of humanity on fossil fuels for energy production and slow progress of clean energy application in the last years. This seriously leaded to a significant global issue

with huge amount of CO_2 emissions of > 30 Gt since 2010, nearly 100% coming from fossil fuels of coal, oil and natural gas, as shown in Figure 1.1c.

It is well known that, CO_2 equilibrates largely between the atmosphere and the ocean and to remove CO_2 from the atmosphere involves complex and long-term processes[3-5]. Much higher concentration of CO_2 than preindustrial level has increased global average temperature and sea level which would be high up to 1.9 m if exceeding 1000 ppm[6]. Present CO_2 emission issues are making irreversible climate changes, and it would lead to further irreversible effects on earth and humanity.

1.2. Hydrogen economy for a renewable energy society

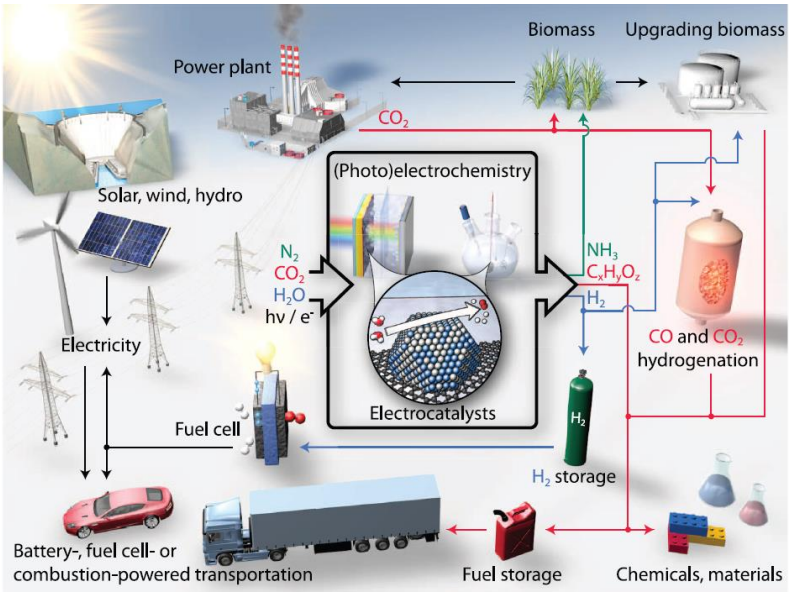

Figure 1.2. Scheme of a sustainable energy landscape based on electrocatalysis[7].

To balance the great amount of energy demand and increasingly serious environment issues due to CO_2 emissions, more sustainable technologies should be utilized to produce necessary chemicals and fuels, such as hydrogen and ammonia, in order to decrease or further replace conventional energy production. To reach future low-carbon target, Seh et al. proposed a sustainable energy future vision about how to take advantage of renewable energy sources including wind, solar and hydro etc., to generate electricity for the production of important chemicals and materials

in industries and transportations based on (photo)electrocatalysis using sufficient biomass, N_2, CO_2 and H_2O as reactants[7]. In this landscape, it is obvious that hydrogen plays a vital and indispensable role, as shown in Figure 1.2.

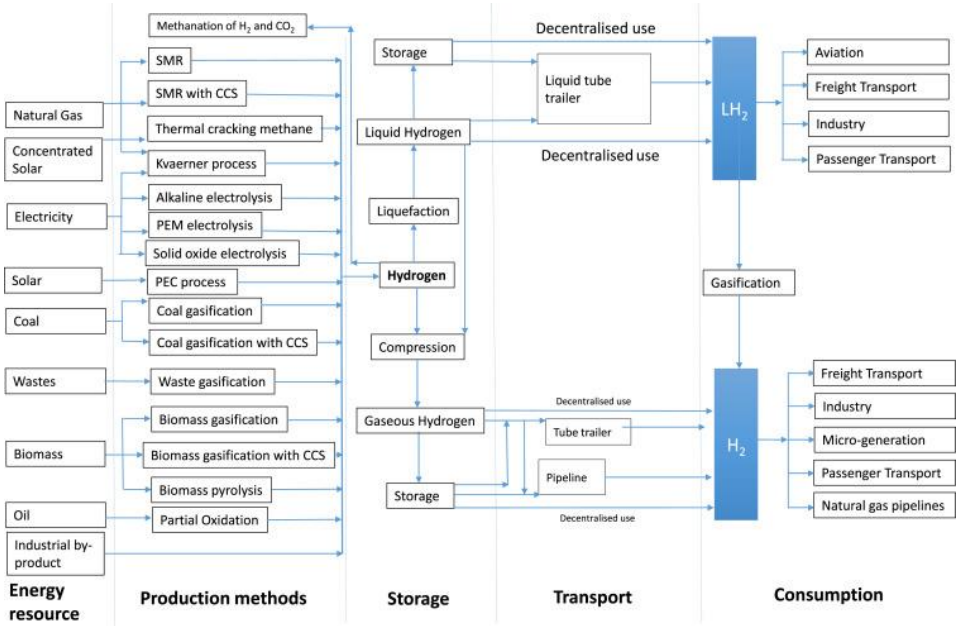

Figure 1.3. Potential hydrogen pathways towards 2050[8].

Hydrogen gas was first artificially produced in 1671 by the reaction of iron fillings and dilute acids. It has high mass energy density of 120 MJ kg^{-1}, around 3 times more than diesel or gasoline. Since that, it has been considered an ideal alternative to replace traditional fuels with producing water as the only byproduct. In the 1970s, the term “hydrogen economy” was originally coined by John Bockris and it described a green society where hydrogen would be electrolytically produced and used for major sectors in our lives, such as factories, transportations and homes. Hanley et al. further described the potential hydrogen pathways of production, storage, transport and consumption towards 2050 with net-zero greenhouse gas emission goal[8] (Figure 1.3). In some calculations, compared to the 88 Mt per year used in current level, it was projected that the global hydrogen demand could reach over 2.3 Gt annually[9,10], which showed a strong market value of hydrogen. However, although hydrogen as a non-emissive energy carrier, has the great potential to frame a 100% green future in the decarbonization

effort, current production methods consist of carbon-rich processes, with 96% of hydrogen generated from fossil fuels (48% natural gas, 30% oil, 18% coal).

It was compared quantitively in terms of costs from different hydrogen production methods in Table 1.1[11], and the rather higher price of per kg of H_2 production and capital cost were the major reasons to greatly restrict the wide applications of water electrolysis from clean wind and solar sources for hydrogen production with less than 4% in total, than those of the mature steam methane reforming technologies. But the declining expense of renewable energy resources, as well as the enhancing efficiency and technological advancement for electrolysis, contribute to the possibility of renewably sourced electrolytic H_2 in some cases.

Table 1.1. Comparison of various hydrogen production processes[11].

Process	Energy source	Feedstock	Capital cost (M$)	Hydrogen cost ($/kg)
SMR with CCS	Standard fossil fuels	Natural gas	226.4	2.27
SMR without CCS	Standard fossil fuels	Natural gas	180.7	2.08
CC with CCS	Standard fossil fuels	Coal	545.6	1.63
CG without CCS	Standard fossil fuels	Coal	435.9	1.34
ATR of methane with CCS	Standard fossil fuels	Natural gas	183.8	1.48
Methane pyrolysis	Internally generated steam	Natural gas	–	1.59–1.70
Biomass pyrolysis	Internally generated steam	Woody biomass	53.4–3.1	1.25–2.20
Biomass gasification	Internally generated steam	Woody biomass	149.3–6.4	1.77–2.05
Direct bio-photolysis	Solar	Water + algae	50 $/m^2	2.13
Indirect bio-photolysis	Solar	Water + algae	135 $/m^2	1.42
Dark fermentation	–	Organic biomass	–	2.57
Photo-fermentation	Solar	Organic biomass	–	2.83
Solar PV electrolysis	Solar	Water	12–54.5	5.78–23.27
Solar thermal electrolysis	Solar	Water	421–22.1	5.10–10.49
Wind electrolysis	Wind	Water	504.8–499.6	5.89–6.03
Nuclear electrolysis	Nuclear	Water	–	4.15–7.00
Nuclear thermolysis	Nuclear	Water	39.6–2107.6	2.17–2.63
Solar thermolysis	Solar	Water	5.7–16	7.98–8.40
Photo-electrolysis	Solar	Water	–	10.36

1.3. Water electrolysis

Water (H_2O) electrolysis is the electrochemical approach of splitting water into H_2 and O_2: $H_2O \rightarrow H_2 + 1/2\ O_2$. The main water electrolysis technologies are Alkaline Electrolysis (AEL), Proton Exchange Membrane (PEM) Electrolysis (PEMEL) commercially available and Solid Oxide Electrolysis (SOEL), Anion Exchange Membrane (AEM) Electrolysis (AEMEL) in the maturing level, shown in Figure 1.4. Correspondingly, the electrolyzer capacities of different technologies in 2019-2030 in Table 1.2 shows the major contribution from AEL and PEMEL currently.

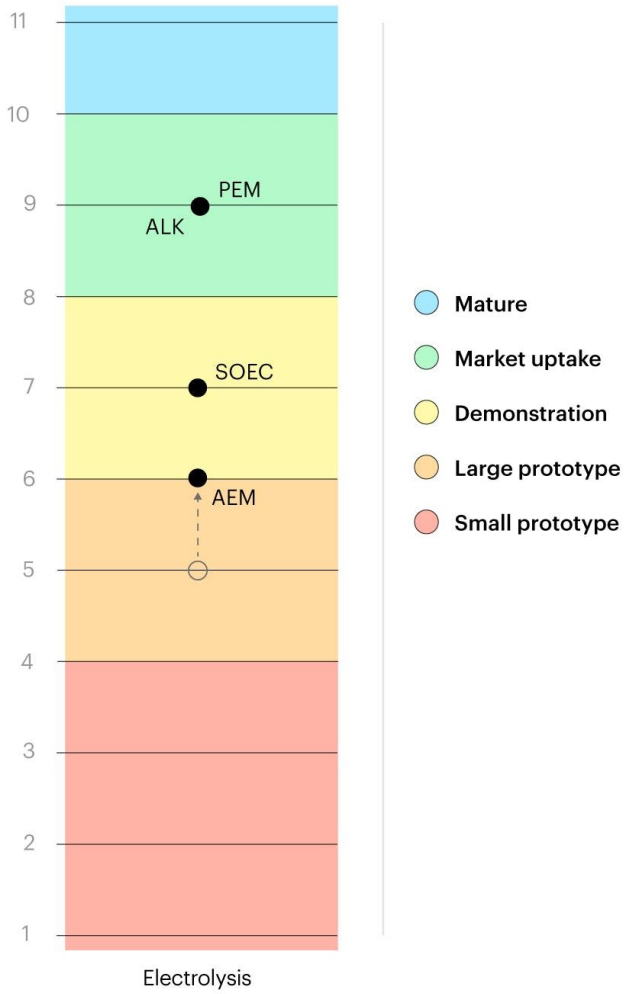

Figure 1.4. Electrolyzer technology readiness level[12].

Table 1.2. Total installed electrolysis capacity by technology in the Net Zero Scenario, 2019-2030[12]. Note that capacity in 2022 and 2023 is based on projects under construction or planned, with a disclosed start year of operation. NZE = Net Zero Emissions by 2050 Scenario.

Year	Alkaline MW	PEM MW	Other/unknown MW	Total MW
2019	164	65	13	242
2020	197	93	14	304
2021	354	126	33	513
2022	727	366	306	1 398
2023	1 459	1 125	2 933	5 517
2030 - NZE	-	-	-	720 000

$$2\,OH^-(aq) \rightarrow H_2O(l) + \frac{1}{2}\,O_2(g) + 2\,e^- \quad (1)$$

[anode, $E^\circ = 0.40$ V versus SHE, pH 14]

$$2\,H_2O(l) + 2\,e^- \rightarrow H_2(g) + 2\,OH^-(aq) \quad (2)$$

[cathode, $E^\circ = -0.83$ V versus SHE, pH 14]

$$H_2O(l) \rightarrow \frac{1}{2}\,O_2(g) + 2\,H^+(aq) + 2\,e^- \quad (3)$$

[anode, $E^\circ = 1.23$ V versus SHE]

$$2\,H^+(aq) + 2\,e^- \rightarrow H_2(g) \quad [\text{cathode, } E^\circ = 0.00\text{ V}] \quad (4)$$

Alkaline electrolyzer is a more mature technology with a long history of deployment in the chlor-alkali industry[13]. The anodic and cathodic equations for alkaline electrolysis (pH 14) are shown in Equations (1) and (2), respectively (SHE = standard hydrogen electrode). Figure 1.5a shows the OH^- migrating and gas releasing in alkaline solution.

On the other hand, PEM electrolyzers have been commercialized for around 20 years, which are using a more recent technology that features a gas-tight (≤ 0.2 mm thickness) solid-phase polymer membrane with H^+ as a charge carrier instead of OH^- (Figure 1.5b). This acidic electrolysis reaction equations on anode and cathode are shown as Equations (3) and (4), respectively. In the Table 1.3, the working conditions and efficiencies are compared in detail between alkaline electrolysis and PEM electrolysis.

Higher allowable current densities, conversion and gas purities give more obvious advantages on PEM electrolysis for hydrogen production.

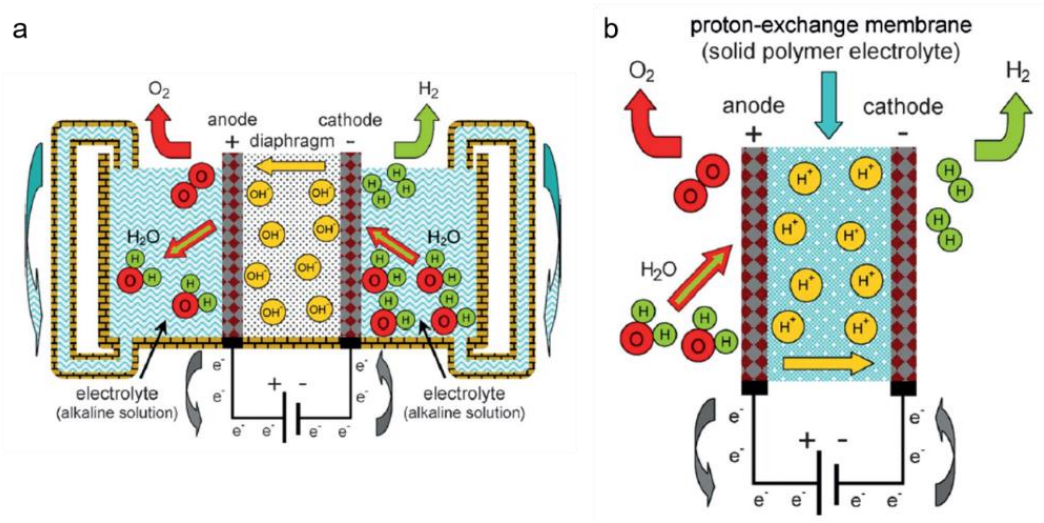

Figure 1.5. (a) Components of an alkaline electrolyzer and the migration of chemical species within; (b) A PEM electrolyzer with migration of chemical species[14].

Table 1.3. State-of-the-art specifications for alkaline and PEM electrolyzers[14].

Specifications	Alkaline electrolysis	PEM electrolysis
cell temperature [°C]	60–80	50–80
cell pressure [bar]	< 30	< 30
current density [mA cm^{-2}]	0.2–0.4	0.6–2.0
cell voltage [V]	1.8–2.4	1.8–2.2
power density [mW cm^{-2}]	< 1	< 4.4
voltage efficiency HHV [%]	62–82	67–82
specif. energy consumption: stack [kW h Nm^{-3}]	4.2–5.9	4.2–5.6
specif. energy consumption: system [kW h Nm^{-3}]	4.5–7.0	4.5–7.5
lower partial load range [%]	20–40	0–10
cell area [m^2]	> 4	< 0.03
H_2 production rate: stack system [Nm^3 h^{-1}]	< 760	< 10
stack lifetime [h]	< 90 000	< 20 000
system lifetime [years]	20–30	10–20
degradation rate [μV h^{-1}]	< 3	< 14

1.4. Oxygen evolution reaction

Water electrolysis is composed of a hydrogen evolution reaction (HER) at the cathode (Equation (2) and (4)) and oxygen evolution reaction (OER) at the anode (Equation (1) and (3)). In the electrochemical water splitting systems, the slow 4 electron transfer process involved in OER is a sluggish but critical step for hydrogen production, affording a significant efficiency loss that hinders the wide commercial applications. The kinetics of the OER in acidic and alkaline media depend on the material by which it is being catalyzed.

In theoretically proposed modes, the OER proceeds in four reaction steps under acidic or basic conditions, in Equation (5)-(8) or (9)-(12), respectively, as one of the most widely accepted mechanisms:

$H_2O \rightarrow OH^* + H^+ + e^-$ (5)

$OH^* \rightarrow O^* + H^+ + e^-$ (6)

$H_2O + O^* \rightarrow OOH^* + H^+ + e^-$ (7)

$OOH^* \rightarrow O_2^* + H^+ + e^-$ (8)

$OH^- \rightarrow OH^* + e^-$ (9)

$OH^- + OH^* \rightarrow H_2O + O^* + H^+ + e^-$ (10)

$OH^- + O^* \rightarrow OOH^* + e^-$ (11)

$OH^- + OOH^* \rightarrow H_2O + O_2 + e^-$ (12)

where * indicates a surface adsorption site, and OH*, O* and OOH* denote adsorbed intermediates. Among the four steps, the elementary reaction step with the highest kinetic barrier is defined as the rate determining step (RDS) and the Gibbs free energies of RDSs can be taken as a guideline to design efficient OER catalysts[7].

1.4.1. Parameters for the evaluation of electrocatalytic performance

a. Overpotential (η)

The thermodynamic equilibrium potential (E^0) of the OER is 1.23 V versus the reversible hydrogen electrode (RHE) under standard conditions. But in a

real system, there is no electrochemical reaction occurring at the potential and much higher potentials need to be applied to overcome the large energy barrier originating from the sluggish reaction kinetics to achieve the appreciable conversion of OH^-/H_2O to O_2. This additional driving force in terms of an extra potential is called the overpotential. There are 3 sources of overpotential: the activation overpotential which is an intrinsic property of the OER catalyst and differs from one material to another, the concentration overpotential which can be minimized by accelerating the mass transfer and resistance overpotential which can be compensated in electrochemical workstations or manually[15]. To match a solar water splitting device efficiency of 12.3% under 1 sun illumination, current density (j) of 10 mA cm^{-2} is usually used as the figure of merit where the overpotential here is defined as η_{10}[16,17].

b. Tafel slope

Tafel equation can be expressed as

$$\eta = a + b * \lg (j) \quad (13)$$

where b denotes the Tafel slope and

$$b = 2.303\ RT/\alpha nF \quad (14)$$

The Tafel slope is proportional to temperature (T) and inversely proportional to the charge transfer coefficient (α) with the ideal gas constant (R), the number of electrons transferred (n) 4 for OER and Faraday constant (F). The Tafel slope can be calculated using Equation (13) and according to Equation (14), it shows that a catalyst with a high charge transfer ability should possess a small Tafel slope so it is often used as a critical parameter in determining the catalytic activity. Steady-state polarization curve, chronoamperometric i−t curves obtained at various overpotentials or the Nyquist plots at various overpotentials in the electrochemical impedance spectroscopy (EIS) are normally analyzed to obtain Tafel slope values.

c. Stability

The stability of an electrocatalyst is usually tested by the cyclic voltammetry (CV) accelerated degradation test, chronoamperometry or

chronopotentiometry. To compare the corresponding overpotential differences at different current densities before and after CV measurement, potential or current response changes through time in chronoamperometric or chronopotentiometric tests, respectively, it is clear to distinguish if a catalyst's stability is good with smaller differences/changes showing higher stabilities.

d. Faraday efficiency (FE)

Faraday efficiency is a quantitative parameter to determine how efficient of a catalyst to transfer electrons from external circuit to generate target product. It can be calculated to compare experimental and theoretic O_2 production value. Technically, there are 2 experimental method to measure Faraday efficiency.

One method is using rotating ring-disk electrode system where OER happens on the glassy carbon disk and oxygen reduction reaction (ORR) on the Pt ring to calculate FE value by Equation (15) below:

$$FE = \frac{I_R n_D}{I_D n_R N_{CL}} \qquad (15)$$

Where I_R, n_R and I_D, n_D are the current and electron transfer numbers at ring and disk, respectively, and N_{CL} is the collection efficiency which can be determined by the Fe (III)/Fe (II) redox system[18].

Another is to quantify the practically generated O_2 gas during chronoamperometric or chronopotentiometric tests by the conventional water-gas displacement setup, gas chromatography or spectroscopic technique.

e. Turnover Frequency (TOF)

TOF is defined as the number of moles of evolved O_2 per unit of time, another quantitative parameter to evaluate a catalyst's activity but under a given overpotential. It is calculated by Equation (16) below:

$$TOF = \frac{IN_A}{AF_n\Gamma} \qquad (16)$$

where I is the current, N_A is the Avogadro constant, A is the geometrical surface area, n=4 is the number of electrons transferred while Γ is the total concentration of catalyst on electrocatalytic surface in terms of number of atoms, hard to be directly measured because the number of active sites is often overestimated by counting the total active species with those of the chemically inert or buried species included. In the CV curve, the redox peak is tried to find surface concentration[18]. Also, the total concentration of atoms could be calculated using the average particle diameter of the catalyst in the Avogadro's number method[19]. Another method is a monolayer assumption that the surface is flat and smooth or the catalyst has a sheet morphology[20].

f. Mass and specific activities

The mass and specific activities are two other quantitative parameters used to define the catalytic activity of an electrocatalyst when obtained current signal normalized by catalyst loading and electrochemical surface area (ECSA), respectively.

Noble metal electrocatalysts, such as Ir, Ru and their oxides as well as composites are the state-of-the-art OER catalysts and catalyze the OER more easily in acidic media than under alkaline conditions. But large-scale commercialization of them is greatly hindered by their low reserve and high cost. Thus, tremendous efforts have been devoted to exploring high-performance noble-metal-free electrocatalysts in both acidic and alkaline media.

1.4.2. Non-noble metal-based OER electrocatalysts in alkaline media.

Recently, a variety of heterogeneous catalysts derived from non-noble metal transition metals, such as Ni and Fe, in the fourth elemental period have been found to catalyze the OER very well with the advantages of low cost, environmental friendliness, high activity and excellent long-term stability comparably to or even better than noble metal-based catalysts in alkaline media[15,21-24].

The spinel oxides are a class of minerals of general formulation AB_2O_4 which crystallize in the cubic (isometric) crystal system, with oxygen arranged in a

cubic close-packed lattice and the cations A and B, which are normally made of group 2, 13 and first-row transition metal elements, occupying some or all of the octahedral and tetrahedral sites in the lattice. The structure of a spinel is illustrated in Figure 1.6a. It is allowed to control their compositions and tune the electronic structures via metal doping. Normally, ferrites are poor conductors of electricity so that a second transition metal dopant is critical to improve their electrochemical performance. A sequence of $CoFe_2O_4$ > $CuFe_2O_4$ > $NiFe_2O_4$ > $MnFe_2O_4$ for doped ferrite with Co, Cu, Ni and Mn in terms of OER electrocatalytic activities was found[25]. Furthermore, Nuria et al. introduced a Zn, Ni-doped ferrite ternary system to prove that cooperative electronic effects at surface- and active-sites are key to designing outstanding OER catalyst[26]. The optimal catalyst with equimolar stoichiometry favored the formation of oxygen vacancies where Zn pushed the electronic density that was pulled by the octahedral Fe and tetrahedral Ni redox pair lowering the overpotential (Figure 1.6b). The catalytic activity of this cubic spinel in the series could directly compete with the best ternary oxides as reported by Stahl et al.[27] (325 mV overpotential for $NiFeGaO_n$ and 331 mV for $NiZnFeO_n$ to reach 10 mA cm^{-2}) or those derived from extensive machine learning with outstanding stability at high currents[28]. In addition, $ZnCo_2O_4$ or $CoAl_2O_4$ were prepared with Zn^{2+} replacing Co^{2+} or Al^{3+} replacing Co^{3+}, respectively and their OER activities were compared with Co_3O_4 to explain the different structural site function[29]. As shown in Figure 1.6c, the activity of $CoAl_2O_4$ was similar to that of Co_3O_4 while $ZnCo_2O_4$ performed much worse, which revealed that Co^{2+} ions and Co^{3+} ions were differently responsible for OER catalysis in the case of Co_3O_4 and the divalent Co^{2+} dominated the OER activity. This interesting finding guided us to obtain better OER performance for spinel oxides using suitable second or third metal dopants to optimize the electronic structures.

Under the strong oxidizing conditions during the OER process, the surface of most OER electrocatalysts undergoes significant physicochemical property changes and the formation of a newly reconstructed surface. During anodic polarization, the metal cations in the catalyst surface typically shift from their more stable lower valence states (0, +2) to their more electrocatalytically active higher valence states (+3, +4) before achieving

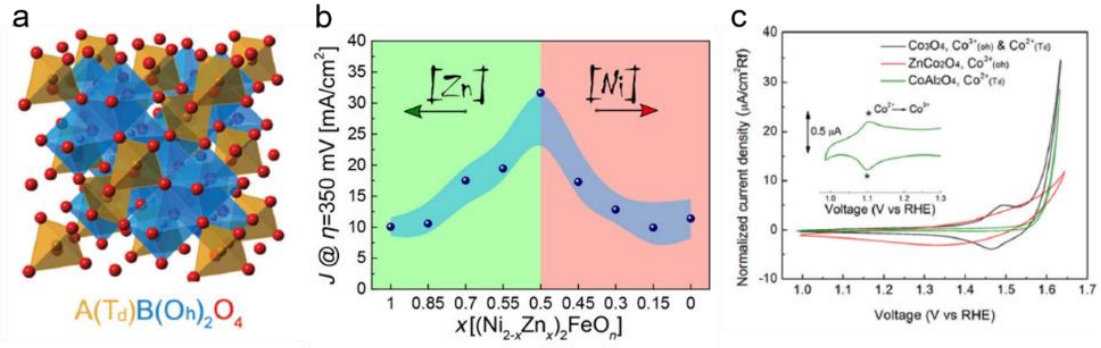

Figure 1.6. (a) Crystal structure of spinel. (b) Current densities at 350 mV overpotential for Ni-Zn-Fe system. (c) Normalized cycling voltammetry curves for Co_3O_4, $ZnCo_2O_4$, and $CoAl_2O_4$.

oxygen evolution (e.g., typically 1.0–1.4 V vs. RHE)[22,23]. In addition, according to enthalpy analyses, the oxides are the thermodynamically stable final product of most electrochemical processes in aqueous solution[30,31]. Accordingly, a high probability of reconstructing into oxides or (oxy)hydroxides more easily occurs on the surface of transition metal-based non-oxide electrocatalysts, like metal sulfides/ selenides/ nitrides/ phosphides/ borides/ fluorides which actually act as "pre-catalysts", forming their corresponding real active species[21-23,32-39]. For example, taking advantage of in situ electrochemical oxidation, Hu et al. first developed and utilized Ni_2P as an OER catalyst in alkaline medium, and observed an electrochemical oxidation process involving its transformation into a core–shell structure, Ni_2P/NiO_x assembly[40]. And Cui et al. further synthesized in situ electrochemically tuned transition metal oxides (ECT-TMO) after CV sweeping of the corresponding transition metal sulfides (TMSs, including CoS_2, $Co_{0.5}Fe_{0.5}S_2$, and $Co_{0.37}Ni_{0.26}Fe_{0.37}S_2$) in alkaline electrolyte[41]. Besides numerous nanopores created on ECT-TMOs, an increased amount of electrocatalytically active sites on ECT-TMOs was obtained, leading to greatly improved OER activity. ECT-$Co_{0.37}Ni_{0.26}Fe_{0.37}O$ showed a much lower overpotential (at current density of 10 mA cm^{-2}) of 232 mV than the directly synthesized $Co_{0.37}Ni_{0.26}Fe_{0.37}O$ (299 mV). Similarly, using NiSe as a representative example of metal selenides, Hu et al. found that metal selenides were converted into metal oxides or hydroxides under OER conditions, which were responsible for the catalytic activity of metal

selenides in OER. Utilizing this in-situ transformation, a nickel iron diselenide ($Ni_xFe_{1-x}Se_2$) was used as a templating precursor to obtain the corresponding oxide, $Ni_xFe_{1-x}Se_2$-DO with high OER catalytic performance, delivering current density of 10 mA cm^{-2} with an overpotential of only 195 mV. Interestingly, unlike the surface reconstruction occurring on metal oxides, the non-oxide elements (S/Se/N/P/B/F) were found to be depleted during anodic polarization, and subsequently replaced by oxygen, which led to the surface reconstruction of metal non-oxides into metal oxides/(oxy)hydroxides[40,42].

As described above, heteroatom doping and surface restructuring are the most common methods for syntheses of efficient OER electrocatalysts with high performance. To observe the changes of structure and physicochemical property, and understand inner mechanisms, post-catalysis analyses (scanning and transmission electron microscopies, X-ray diffraction, X-ray photoelectron spectroscopy, elemental analysis etc.) for electrode materials and electrolytes are necessary[21]. If available, Operando/in-situ technique analyses are also needed for better understanding[43-45].

1.4.3. Non-noble metal-based OER electrocatalysts in acidic media.

As shown in the Table 1.3, the commercially developed PEM technology shows some immediate advantages of higher capacities of hydrogen production, maximum allowable current densities, conversion efficiency and gas purities. But in general, the anode catalysts are based on noble metals, Ir and Ru with high activity and stability, which takes up to ~6% cost of the whole system[14]. To reduce the usage of noble metals and decrease the financial costs are critical for wide application of PEM electrolyser.

In the alkaline solutions, there are a wide range of high-performance non-noble metal-based materials for OER electrocatalysis. But when the working media changed to acidic solutions, they would lose their activities and be dissolved according to the Pourbaix diagrams under high potentials, making it significantly challenging to find a viable and efficient non-noble metal-based OER electrocatalyst which could be compared with Ir, Ru-based compounds.

Table 1.4. Performance parameters for different electrocatalysts for OER in acidic electrolytes.

Catalyst	H_2SO_4 (M)	Scan rate (mV s^{-1})	η (mV)[a]	Tafel slope (mV dec^{-1})	Stability	Loading (mg cm^{-2})	Ref.
[Co-POM]/CP	1	1	361	97	24 h @ η = 250 mV	20	71
ATO/CoHFe	0.1	50	770	~	~	0.61	72
$IrO_2/SrIrO_3$	0.5	10	280	~	30 h[a]	~	73
$CoFePbO_x$	1	~	620	~	12 h @ 2.03 V	~	57
MnO_2	0.1	1	428	80	8000 h[a]	36	53
$Ni_{0.5}Mn_{0.5}Sb_{1.7}O_x$	1	10	672	60	168 h[a]	~0.18	54
$Co_{0.05}Fe_{0.95}O_y$	0.5	10	650	110	50 h[a]	1	60
$Mn_xSb_{1-x}O_z$	1	20	508	75	2 h[a]	~	50
Co_3O_4/FTO	0.5	2	490	80	12 h[a]	~	55
Co_3O_4/CeO_2/FTO	0.5	5	423	88	50 h[a]		56
Ti-MnO_2	0.05	5	~540[b]	170	2 h @ 1.9 V	~	47
$Ni_{40}Fe_{40}P_{20}$	0.05	5	540	-	30 h[a]	~	66
c-Fe_2O_3	0.5	10	650	56	24 h[a]	1	74
P-NSC/ $Ni_4Fe_5S_8$-1000	0.5	2	~560	72	10000 cycles[c]	0.4	65
1T-MoS_2	0.5	5	420	322	2 h[a]	1	69

[a] @ 10 mA cm^{-2}. [b] @ 2 mA cm^{-2}. [c] @ 1 mA cm^{-2}

Even it cannot achieve noble metal-free target on the anode in the commercial PEM electrolyser nowadays, many researchers have tried to investigate the dissolution mechanism and further improve the acidic OER catalytic performance using several strategies, as shown in Table 1.4. In 2014, Nocera et al. reported a comprehensive electrochemical characterization of manganese oxide (MnO_x) in acid, and revealed MnO_x as a functionally stable OER catalyst owing to self-healing which was that MnO_x redeposition offseted catalyst dissolution during turnover[46]. Since that, numerous Mn-based oxides have been synthesized and optimized, such as TiO_2-incorporated MnO_2[47], hausmannite derived MnO_2[48], metastable Mn^{3+} activated MnO_2[49], Mn-Sb-O system[50], F doped $Cu_{1.5}Mn_{1.5}O_4$[51], $(Mn_{0.9}Nb_{0.1})O_2$:10F[52] etc. Among these Mn-based oxides, impressively, a γ-MnO_2 on FTO was fabricated and could catalyze the OER at 10 mA cm^{-2} for over 8000 hours in a pH 2 electrolyte with no noticeable decrease in activity[53]. And a nickel-manganese antimonate electrocatalyst with a rutile-type crystal structure could catalyze OER in contact with 1.0 M sulfuric acid. Under galvanostatic

control, the overpotential initially rose from 670 mV and then stable at 735mV for 168 h of continuous operation at 10 mA cm^{-2} [54].

On the other hand, Co-based oxides are the other most widely researched electrocatalysts for acidic OER[55-62]. Schaak et al. firstly developed nanostructured films of cobalt oxide (Co_3O_4) on the fluorine-doped tin oxide (FTO) substrate with a robustly electrical and mechanical Co_3O_4/FTO interface as an active OER catalyst in 0.5 M H_2SO_4[55]. Then, Jin et al. introduced nanocrystalline CeO_2 to form a heterogeneous Co_3O_4/CeO_2 nanocomposite on FTO and carbon paper to achieve a geometric catalytic current density of 10 mA cm^{-2} with ~423 and 347 mV overpotentials, respectively, making it an efficient earth-abundant electrocatalysts for acidic OER[56]. In-situ Raman and ex-situ X-ray absorption spectroscopy (XAS) structural characterization results revealed that the introduction of nanocrystalline CeO_2 could modify the electronic structures and create a more favorable local bonding environment in Co_3O_4. The Co^{3+} surface species could be easily oxidized into OER-active Co^{4+} species and suppress the charge accumulation of Co_3O_4 under these conditions, which was helpful to bypass the potential-determining redox step in Co_3O_4 and thus enhance the acidic OER activity. In addition, based on the similar self-healing mechanism described above, a highly disordered mixed metal oxide $CoFePbO_x$ was generated from dissolved Co, Pb and Fe precursors on FTO, allowing for a continuous oxygen evolution at temperatures up to 80 °C and rates up to 500 mA cm^{-2} at overpotentials below 0.7 V[57]. Furthermore, to incorporate the critical Mn element into the spinel lattice of Co_3O_4, Co_2MnO_4 was prepared in which Co occupied both octahedral sites and tetrahedral sites, and Mn preferentially occupied the octahedral sites [63]. This compound could reach a current density of 1 A cm^{-2} at 1.95 V and when supported on Pt/Ti mesh, it was stable for > 1500 h in pH 1 at 200 mA cm^{-2}, exhibiting excellent electrocatalytic performance. Density functional theory (DFT) calculations supported that the good stability was due to the ideal binding energies for the OER intermediates and unfavourable thermodynamics for the elementary steps of dissolution.

Moreover, using computational Pourbaix diagrams, Nørskov and co-workers made a systematic exploration on the aqueous stability of 47814 oxides and

identified 68 acid-stable candidates under acidic oxygen evolution reaction condition[64]. Accordingly, an acid-stable periodic table was constructed (Figure 1.7) and some of Sb/Ti/Sn/Ge/Mo/W-based oxides with better corrosion resistance were predicted as potential candidates for OER in acid.

Apart from oxides, some researches about transition metal chalcogenides, pnictides and borides, have also been reported but these compounds are unstable under OER cycling condition and some of them can even decompose/dissolve immediately if contact with acid electrolytes[65-70].

Developing robust catalysts for OER in acid with both good activity and stability is a big challenge. To discover active and stable electrode materials, most effort was put on the catalysts themselves, while neglecting the solid–liquid interfaces since electrocatalytic reactions occur at the catalyst-electrolyte interface. Such an interface may be more complicated in acidic electrolyte[71]. Thus, there needs more understanding of how the surface of catalysts and interfacial water structure interacts with each other.

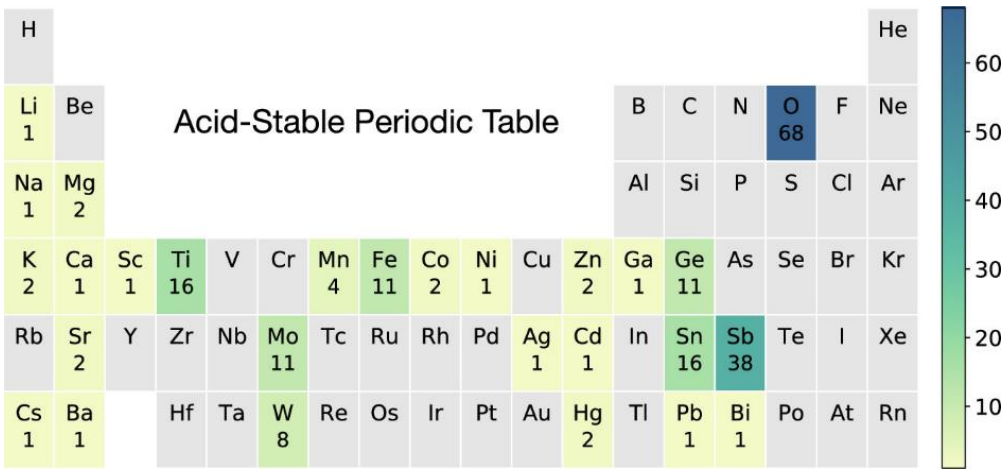

Figure 1.7. Frequency at which each element appears in acid-stable oxides. Elements with zero frequency are shaded in gray. Lanthanoids and actinoids are omitted for clarity because no oxide containing these elements was predicted to be stable[64].

1.5. Hydrogen evolution reaction

In the water splitting, hydrogen evolution reaction happens on the cathode. In acidic media, the cathodic reaction of the water electrolysis is the

reduction of proton ions H_3O^+ to gaseous H_2. Thermodynamically, this 2-electron electrode reaction should occur at 0 V vs the reference hydrogen electrode (RHE). The first step of this reaction is called as Volmer Step (Equation 17): the reduction of a proton and adsorption of hydrogen on the catalyst surface, followed by the evolution of molecular dihydrogen, either through Heyrovsky step: a second proton/electron transfer (Equation 18) or Tafel step: the recombination of two adsorbed hydrogen (Equation 19):

$$H_3O^+ + e^- + * \rightarrow H^* + H_2O \quad (17)$$

$$H^* + H_3O^+ + e^- \rightarrow H_2 + H_2O \quad (18)$$

$$2H^* \rightarrow H_2 \quad (19)$$

where * denotes an active site on the catalyst surface, and H* an adsorbed hydrogen atom on the active site. In general, one step kinetically limits the electrochemical reaction is called the rate-determining step (RDS). The HER kinetics is strongly dependent on the electrode electrocatalysts. HER happens very fast on platinum while on a mercury electrode it exhibits slow kinetics. The electrode kinds, crystalline nature and orientation of the electrode (single-crystal, polycrystalline, amorphous, etc.) are also the keys to affecting HER. In the **section 1.4.1**, the parameters for the evaluation of electrocatalytic performance of an electrocatalyst are also applicable on HER.

By the Tafel slope analyses, the Tafel slope for Pt (110) and polycrystalline Pt was ~30 mV dec^{-1}, which meant the Tafel step was determined as the RDS for them while the Heyrovsky step was the RDS for Pt (100) with the Tafel slope of 40 mV dec^{-1}. But for Pt (111), the Tafel slope was 74 mV dec^{-1} which did not match the expected values from kinetics analysis[75]. The HER kinetics strongly hinges on the interaction between the catalyst and H*. Nørskov et al. collected experimental data of exchange current densities for HER on various metals and calculated the corresponding adsorption energies using the density functional theory (DFT), as shown in Figure 1.8[76]. The first modern volcano plots were presented and it elucidated the origin of the superior HER activity of Pt. Also, it introduced an intuitive descriptor of hydrogen binding energy for the dependence of HER activity.

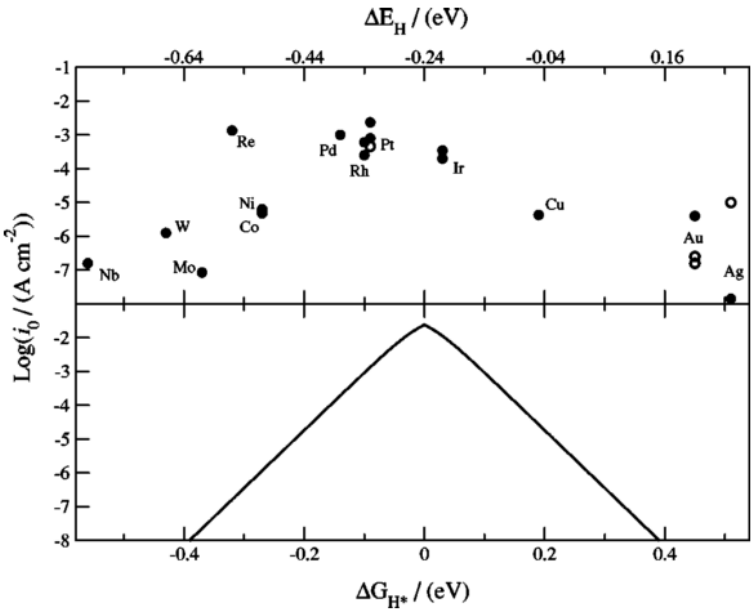

Figure 1.8. (top) Experimentally measured exchange current, log(j_0), for hydrogen evolution over different metal surfaces plotted as a function of the calculated hydrogen chemisorption energy per atom, ΔE_H. (bottom) The result of the simple kinetic model now plotted as a function of the free energy for hydrogen adsorption[76].

Table 1.5 Heterostructures for HER in acidic solutions.

Catalyst	Overpotential (mV) @ 10 mA cm^{-2}	Tafel slope (mV dec^{-1})	Mass loading (mg cm^{-2})	Electrolyte	Ref.
$Pt/MoS_2/NiS_2$	34	40	0.57	0.5 M H_2SO_4	77
$Pt/Mo_2TiC_2T_x$	30	30	1	0.5 M H_2SO_4	78
$Co\text{-}FeS_2/CNT$	160	46	0.4	0.5 M H_2SO_4	79
CoNi@NC	142	105	1.6	0.1 M H_2SO_4	80
$CoS_2/CoSe_2$	80	34	0.28	0.5 M H_2SO_4	81
FeP/C	71	52	~	0.5 M H_2SO_4	82
$Mo_2C\text{-}Mo_2N/CNT$	96	37	0.4	1 M H_2SO_4	83
$MoS_2/CoS_2/CC$	87	73	~	0.5 M H_2SO_4	84
MoS_2/MGF	100	42	0.21	0.5 M H_2SO_4	85
$Ni_2P/CoP/CC$	55	48	~	0.5 M H_2SO_4	86
$Ni_2P/Mo_2C/MWCNT$	154	83	0.2	0.5 M H_2SO_4	87
PANI/CoP HNWs-CFs	57	35	0.8	0.5 M H_2SO_4	88
P-WN/RGO	85	54	0.34	0.5 M H_2SO_4	89
$W_2C/MWCNT$	123	45	0.56	0.5 M H_2SO_4	90
$W_xC@WS_2$	146	61	0.3	0.5 M H_2SO_4	91
$ZnSe/MoSe_2$	200	73	~	0.5 M H_2SO_4	92

MoS_2/C	122	39	0.28	0.5 M H_2SO_4	93
MoS_2/NCNT	110	40	0.1	0.5 M H_2SO_4	94
MoO_x/MoS_2	259	63	~	0.5 M H_2SO_4	95

It is well known that Pt has been considered as the most efficient electrocatalyst for HER in acidic media with near zero overpotential and low Tafel slope. But due to its scarcity and high market price, the use of Pt is limited industrially. To deal with this situation, it necessitates efficient electrocatalytic materials based on inexpensive elements for HER. In the search for alternate and economically viable catalysts, non-noble transition metal-based electrocatalysts have been widely researched and reported in the last decades using a variety of techniques to adjust electrocatalytic property parameters. Material heterostructuring is considered as the most effective approach and Table 1.5 showed several efficient HER electrocatalysts with high activities.

Graphene, reduced graphene oxide (RGO) and other carbon-based compounds are normally used as ideal support for active materials (Transition metal-based phosphides/sulfides etc.) owing to high specific area and excellent conductivity, such as $MoSe_2$, WS_2, P-WN nanosheets on RGO sheets[89,96,97], FeP/$W_xMo_{1-x}S_2$ nanoparticles grown on graphene sheets[98,99], N, S co-doped GO sheets decorated with CoP[100]. In these carbonaceous material-supported heterostructures, the substrates confined the formation of well-dispersed nanostructures and avoided the clustering for the exposure of sufficient active sites. In addition, these highly conductive carbonaceous substrates also favored fast electron transport in the heterostructures and the presence of heteroatom dopants might adjust the electronic structure and further improve the charge transfer for better electrocatalytic HER performance.

Like Graphene and RGO, MXenes are also 2D materials containing a large family of transition metal carbides, nitrides. Since the discovery of $Ti_3C_2T_x$ in 2011, MXenes have found enormous potential in energy storage and conversion applications because of their superb physicochemical, electrical and mechanical properties[101]. The general formula is $M_{n+1}X_nT_x$ (n = 1-3), where M = transition metal atoms, X is carbon or nitrogen and T_x = -OH, -O, or -F. MXenes are produced as a result of etching of A (IIIA or IVA group

elements in the periodic table) group element of metal ceramic phase MAX with etchants, such as the HF solution[102]. The etching process results in generation of various surface functional groups (-OH, -F, -O) on the MXene surfaces. The MXene models are shown in Figure 1.9.

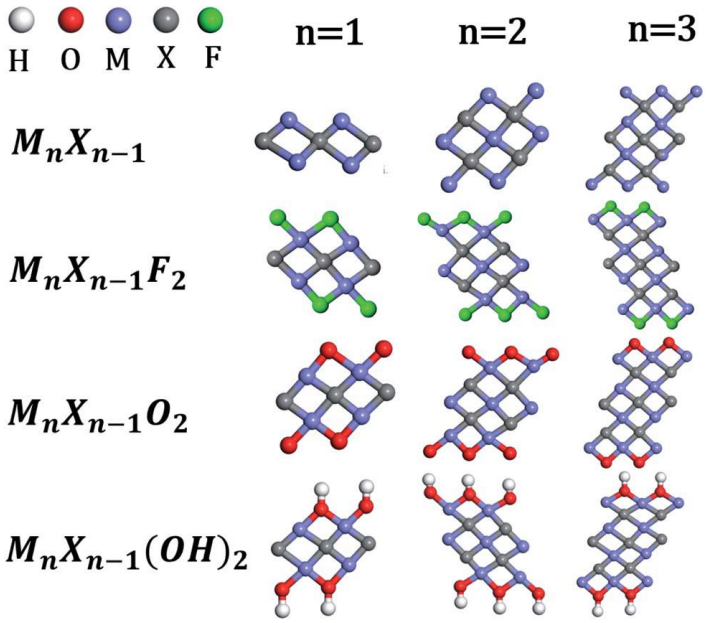

Figure 1.9. Models of bare MXenes (M_nX_{n-1}), fluorine terminated MXenes ($M_nX_{n-1}F_2$), oxygen-terminated MXenes ($M_nX_{n-1}O_2$) and hydroxyl-terminated MXenes [$M_nX_{n-1}(OH)_2$]. n varies from 2 to 4. Color code: blue = metal; deep gray = X; red = oxygen; gray = hydrogen and green = fluorine.

Since the 2D layered structure of MXenes gives high surface area, the containing transition metal provides metallic character and transient electronic states, the presence of surface termination groups introduces hydrophilic character, and adjustable metal center and surface modification brings chances of diverse compositions, it has endowed MXenes with great promise directly as efficient alternative HER electrocatalysts. For instance, Mo_2CT_x and Ti_2CT_x were prepared by Zi et al.[103] and then their HER electrocatalytic activities were measured. The Mo_2CT_x showed a much lower overpotential of 305 mV than 609 mV for Ti_2CT_x at the current density of 10 mA cm^{-2} in 0.5 M H_2SO_4, which could be attributed to the smaller free energy for hydrogen adsorption on Mo_2CT_x. In addition, a novel synthesis introduced Co single atom into the host Mo_2CT_x lattice to favor binding of

hydrogen on the O-terminated surface by a freezing-dry and annealing treatment[104]. The resultant Mo_2CT_x: Co solid solution exhibited excellent activity with a reduced overpotential of 180 mV to deliver 10 mA cm^{-2}. Besides these, the HER performances of some other MXenes were also summarized in Table 1.6.

Table 1.6 HER performance of MXene-based electrocatalysts in acid. Reported overpotentials are at 10 mA cm^{-2}.

Catalyst	Electrolyte	Overpotential (mV)	Tafel slope (mV dec^{-1})	Ref.
Mo_2CT_x	0.5 M H_2SO_4	305	82	103
Mo_2CT_x: Co	1 M H_2SO_4	180	59	104
Ti_2CT_x nanofibers	0.5 M H_2SO_4	169	97	105
P-Mo_2CT_x	0.5 M H_2SO_4	186	~	106
Ultrathin $Ti_3C_2(OH)_x$	0.5 M H_2SO_4	217	89	107
Ultrathin $Ti_3C_2O_x$	0.5 M H_2SO_4	190	61	107
Ultrathin F-Ti_2CT_x	0.5 M H_2SO_4	170	100	108
P_3-V_2CT_x	0.5 M H_2SO_4	163	74	109
MoS_2-Ti_3C_2	0.5 M H_2SO_4	98	45	110
Mo_2CT_x/2H-MoS_2	0.5 M H_2SO_4	119	60	111
P-Mo_2C/Ti_3C_2@NC	0.5 M H_2SO_4	177	57	112
CoP/Ti_3C_2	0.5 M H_2SO_4	71	57	113
MoS_2@Nb_2CT_x	0.5 M H_2SO_4	180	91	114
$MoSe_2$@Ti-MXene	0.5 M H_2SO_4	127	56	115
$V_4C_3T_x$	0.5 M H_2SO_4	200	168	116

Considering that MXenes possess the features of 2D morphology with high specific area, good conductivity and structural flexibility, it could also be liable to combine with other functional materials into composites to reach better electrocatalytic performance. Normally, oxophilic transition metal basal plane of MXenes tends to form their corresponding oxides, which does not facilitate the HER electrocatalytic process so Rui et al. converted Mo_2CT_x into Mo_2CT_x/2H-MoS_2 by two-step sulfidation, reducing the contributions of MoO_{3-x} species and -O terminations. This nanohybrid structure provided a strong interfacial relationship and reached an ultrahigh HER catalytic activity[111]. Similarly, the CoP/Ti_3C_2 heterostructure was obtained by the phosphorization of Co-LDH nanosheet arrays vertically grown on Ti_3C_2 nanoflakes[113]. The resultant irregular morphology gave more accessibility to H_2SO_4 solution and fast H_2 spreading, which was favorable to HER eletrocatalysis. It exhibited an extraordinary performance with a very low overpotential of 71 mV at 10 mA cm^{-2} and Tafel slope of 57 mV dec^{-1}.

Owing to unique host-support interaction effect, heterostructuring is an efficient methodology to obtain high-performance HER electrocatalytic materials. How to design the suitable electrocatalyst structures has become the key to optimal hydrogen absorption free energy and achieving Pt-like performance using earth-abundant elements.

1.6. Thesis goals and outlines

Since long time ago, the great dependence of humanity on fossil fuels for energy production has been continuously increasing. The non-renewable and unevenly distributed features have deeply aggravated global instabilities including economy market shaking and lifestyle changes. Especially in 2022, it has witnessed how energy crisis makes human society suffer indeed. Besides, direct or indirect CO_2 emissions coming from carbon-rich technologies lead to serious climate changes and appearances of extreme weather owing to the greenhouse effect. Although this matter has been under animated discussion on the table, there is no any of fast and effective solutions, putting the whole humanity society in the dilemma of making big changes or going on the way we live.

To develop “Hydrogen economy” is an option and how to take advantage of renewable energy sources including wind, solar etc., to generate electricity for the production of important chemicals and materials is critical. Water electrolyzers are the most promising and sustainable technologies, in which PEM electrolyzer has obvious advantages of high allowable current densities, conversion and gas purities for hydrogen production. But the commercial usage of noble metals has hindered the application in wide range.

Therefore, the objectives of the thesis will be the investigations of different viable approaches to develop the efficient electrocatalytic materials based on non-noble metals for anode and cathode in PEM electrolyzer, respectively.

Proton-rich working condition is favorable for hydrogen evolution reaction on the cathode, which could be electrocatalyzed by a variety of earth-abundant transition element-based materials with Pt-like high performance, as described in the **section 1.5**. In the **Chapter 2**, we have developed a new technique for creating a novel hybrid nanocomposite, Co-containing POM

nanoparticles on 2D MXene nanosheets. The as-prepared Co_9-POM/Ti_3C_2 exhibited excellent Pt-like HER electrocatalytic performance in 0.5 M H_2SO_4 solution. It provides a desirable platform for the design of efficient non-precious-metal HER electrocatalysts in acidic medium with unique heterostructures.

On the other hand, oxygen evolution on the anode is an oxidation reaction and working under high potential for the OER catalysts to reach a desirable current density is necessary. In the **section 1.4**, many efficient OER electrocatalysts based on low-cost materials, such as transition metal-based oxides and phosphide, have been reported and proved to work well in alkaline media. Nevertheless, these materials would lose their high activities and be instable when acid used as electrolytes under high potentials according to Pourbaix diagrams, making noble metal (Ru, Ir)-based catalysts the only choices for acidic OER commercially and further increasing the cost of PEM electrolyzer.

To provide an efficient solution for the problem, in the **Chapter 3**, we present a promising processing protocol, which combines in one single anode two powerful strategies: (i) the incorporation of a nanostructured MOF-derived OER catalyst from earth-abundant metals to maximize active surface area, (ii) supported by a conducting, partially hydrophobic binder made from paraffin oil and graphite powder. This protocol delivers robust and scalable anodes that exhibit excellent acidic OER performances and opens an alternative venue towards fast, energy efficient acid-media water oxidation electrodes.

Since the strategy in the **Chapter 3** for acidic OER has been proved viable and efficient, following this strategy, in the **Chapter 4**, we have been able to conduct an extensive survey of the activity and stability of monometallic, bimetallic and trimetallic earth-abundant transition metal oxides during electrocatalytic OER in strongly acidic conditions. Our results confirm the general validity of the strategy in using a partially hydrophobic electrode to confer high stability to common metal oxides under these harsh conditions. These comprehensive and interesting findings would be helpful in the exploitation of earth-abundant electrocatalysts for acidic OER.

1.7. References

1. United Nations Department of Economic and Social Affairs.
2. International Energy Agency. Energy Statistics Data Browser.
3. Montenegro, A., Brovkin, V., Eby, M., Archer, D. & Weaver, A. J. Long term fate of anthropogenic carbon. *Geophys. Res. Lett.* **34,** 1–5 (2007).
4. Archer, D. & Brovkin, V. The millennial atmospheric lifetime of anthropogenic CO2. *Clim. Change* **90,** 283–297 (2008).
5. Solomon, S., Plattner, G. K., Knutti, R. & Friedlingstein, P. Irreversible climate change due to carbon dioxide emissions. *Proc. Natl. Acad. Sci. U. S. A.* **106,** 1704–1709 (2009).
6. Meehl GA, et al. *Climate Change 2007: The Physical Science Basis* (Cambridge Univ. Press, Cambridge, 2007).
7. Seh, Z. W. *et al.* Combining theory and experiment in electrocatalysis: Insights into materials design. *Science* **80**, 355 (2017).
8. Hanley, E. S., Deane, J. P. & Gallachóir, B. P. Ó. The role of hydrogen in low carbon energy futures–A review of existing perspectives. *Renew. Sustain. Energy Rev.* **82,** 3027–3045 (2018).
9. Oliveira, A. M., Beswick, R. R. & Yan, Y. A green hydrogen economy for a renewable energy society. *Curr. Opin. Chem. Eng.* **33,** 100701 (2021).
10. International Energy Agency. The Future of Hydrogen 2019.
11. Kayfeci, M., Keçebaş, A. & Bayat, M. *Hydrogen production*. *Solar Hydrogen Production: Processes, Systems and Technologies* (2019). doi:10.1016/B978-0-12-814853-2.00003-5.
12. International Energy Agency. Hydrogen Projects Database.
13. Buttler, A. & Spliethoff, H. Current status of water electrolysis for energy storage, grid balancing and sector coupling via power-to-gas and power-to-liquids: A review. *Renew. Sustain. Energy Rev.* **82,** 2440–2454 (2018).
14. Spöri, C., Kwan, J. T. H., Bonakdarpour, A., Wilkinson, D. P. & Strasser, P. The Stability Challenges of Oxygen Evolving Catalysts: Towards a

Common Fundamental Understanding and Mitigation of Catalyst Degradation. *Angew. Chemie - Int. Ed.* **56,** 5994–6021 (2017).

15. Anantharaj, S. et al. Recent trends and perspectives in electrochemical water splitting with an emphasis on sulfide, selenide, and phosphide catalysts of Fe, Co, and Ni: a review. *ACS Catal.* **6**, 8069–8097 (2016)

16. McCrory, C. C. L. et al. Benchmarking hydrogen evolving reaction and oxygen evolving reaction electrocatalysts for solar water splitting devices. *J. Am. Chem. Soc.* **137**, 4347–4357 (2015).

17. McCrory, C. C. L., Jung, S., Peters, J. C. & Jaramillo, T. F. Benchmarking heterogeneous electrocatalysts for the oxygen evolution reaction. *J. Am. Chem. Soc.* **135**, 16977–16987 (2013).

18. Guo, S. X. *et al.* Facile electrochemical co-deposition of a graphene-cobalt nanocomposite for highly efficient water oxidation in alkaline media: Direct detection of underlying electron transfer reactions under catalytic turnover conditions. *Phys. Chem. Chem. Phys.* **16,** 19035–19045 (2014).

19. Anantharaj, S., Karthik, P. E., Subramanian, B. & Kundu, S. Pt Nanoparticle Anchored Molecular Self-Assemblies of DNA: An Extremely Stable and Efficient HER Electrocatalyst with Ultralow Pt Content. *ACS Catal.* **6,** 4660–4672 (2016).

20. Anantharaj, S., Jayachandran, M. & Kundu, S. Unprotected and interconnected Ru0 nano-chain networks: Advantages of unprotected surfaces in catalysis and electrocatalysis. *Chem. Sci.* **7,** 3188–3205 (2016).

21. Gao, L., Cui, X., Sewell, C. D., Li, J. & Lin, Z. Recent advances in activating surface reconstruction for the high-efficiency oxygen evolution reaction. *Chem. Soc. Rev.* **50,** 8428–8469 (2021).

22. Gong, M. & Dai, H. A mini review of NiFe-based materials as highly active oxygen evolution reaction electrocatalysts. *Nano Res.* **8,** 23–39 (2015).

23. Du, J., Li, F. & Sun, L. Metal-organic frameworks and their derivatives as electrocatalysts for the oxygen evolution reaction. *Chem. Soc. Rev.* **50,** 2663–2695 (2021).

24. Chen, F. Y., Wu, Z. Y., Adler, Z. & Wang, H. Stability challenges of electrocatalytic oxygen evolution reaction: From mechanistic understanding to reactor design. *Joule* **5,** 1704–1731 (2021).

25. Li, M. *et al.* Facile synthesis of electrospun MFe_2O_4 (M = Co, Ni, Cu, Mn) spinel nanofibers with excellent electrocatalytic properties for oxygen evolution and hydrogen peroxide reduction. *Nanoscale* **7,** 8920–8930 (2015).

26. Garcés-Pineda, F. A. *et al.* Push-Pull Electronic Effects in Surface-Active Sites Enhance Electrocatalytic Oxygen Evolution on Transition Metal Oxides. *ChemSusChem* **14,** 1595–1601 (2021).

27. Gerken, J. B., Chen, J. Y. C., Massé, R. C., Powell, A. B. & Stahl, S. S. Development of an O 2 -Sensitive Fluorescence-Quenching Assay for the Combinatorial Discovery of Electrocatalysts for Water Oxidation. *Angew. Chemie* **124,** 6780–6784 (2012).

28. Sun, Y., Liao, H., Wang, J. *et al.* Covalency competition dominates the water oxidation structure–activity relationship on spinel oxides. *Nat Catal* **3**, 554–563 (2020)

29. Wang, H. Y. *et al.* In Operando Identification of Geometrical-Site-Dependent Water Oxidation Activity of Spinel Co_3O_4. *J. Am. Chem. Soc.* **138,** 36–39 (2016).

30. Stevanović, V., Lany, S., Zhang, X. & Zunger, A. Correcting density functional theory for accurate predictions of compound enthalpies of formation: Fitted elemental-phase reference energies. *Phys. Rev. B - Condens. Matter Mater. Phys.* **85,** 1–12 (2012).

31. Rasmussen, F. A. & Thygesen, K. S. Computational 2D Materials Database: Electronic Structure of Transition-Metal Dichalcogenides and Oxides. *J. Phys. Chem. C* **119,** 13169–13183 (2015).

32. Wang, Q. *et al.* An overview of heteroatom doped cobalt phosphide for efficient electrochemical water splitting. *Chem. Eng. J.* **456,** 141056 (2023).

33. Huang, C. J. *et al.* A review of modulation strategies for improving catalytic performance of transition metal phosphides for oxygen evolution reaction. *Appl. Catal. B Environ.* **325,** 122313 (2023).

34. Bi, J., Ying, H., Hao, J. & Li, Z. Application of metal chalcogenide-based anodic electrocatalyst toward substituting oxygen evolution reaction in water splitting. *Curr. Opin. Electrochem.* **33,** 100963 (2022).

35. Sun, J., Zhao, Z., Li, J., Li, Z. & Meng, X. Recent advances in transition metal selenides-based electrocatalysts: Rational design and applications in water splitting. *J. Alloys Compd.* **918,** 165719 (2022).

36. Yao, Y., Zhang, Z. & Jiao, L. Development Strategies in Transition Metal Borides for Electrochemical Water Splitting. *Energy Environ. Mater.* **5,** 470–485 (2022).

37. Li, M., Liu, H. & Feng, L. Fluoridation-induced high-performance catalysts for the oxygen evolution reaction: A mini review. *Electrochem. commun.* **122,** 106901 (2021).

38. Tareen, A. K. *et al.* Nickel-Based Transition Metal Nitride Electrocatalysts for the Oxygen Evolution Reaction. *ChemSusChem* **12,** 3941–3954 (2019).

39. Wang, H. *et al.* Transition metal carbides in electrocatalytic oxygen evolution reaction. *Chinese Chem. Lett.* **32,** 291–298 (2021).

40. Stern, L. A., Feng, L., Song, F. & Hu, X. Ni2P as a Janus catalyst for water splitting: The oxygen evolution activity of Ni2P nanoparticles. *Energy Environ. Sci.* **8,** 2347–2351 (2015).

41. Chen, W. *et al.* In situ electrochemical oxidation tuning of transition metal disulfides to oxides for enhanced water oxidation. *ACS Cent. Sci.* **1,** 244–251 (2015).

42. Mabayoje, O., Shoola, A., Wygant, B. R. & Mullins, C. B. The Role of Anions in Metal Chalcogenide Oxygen Evolution Catalysis:

Electrodeposited Thin Films of Nickel Sulfide as 'pre-catalysts'. *ACS Energy Lett.* **1,** 195–201 (2016).

43. Mefford, J., Rong, X., Abakumov, A. *et al.* Water electrolysis on $La_{1-x}Sr_xCoO_{3-\delta}$ perovskite electrocatalysts. *Nat Commun* **7**, 11053 (2016)

44. Bai, L., Lee, S. & Hu, X. Spectroscopic and Electrokinetic Evidence for a Bifunctional Mechanism of the Oxygen Evolution Reaction. *Angew. Chemie* **133,** 3132–3140 (2021).

45. Liu, X. *et al.* Reconstruction-Determined Alkaline Water Electrolysis at Industrial Temperatures. *Adv. Mater.* **32,** 1–10 (2020).

46. Huynh, M., Bediako, D. K. & Nocera, D. G. A functionally stable manganese oxide oxygen evolution catalyst in acid. *J. Am. Chem. Soc.* **136,** 6002–6010 (2014).

47. Frydendal, R., Paoli, E. A., Chorkendorff, I., Rossmeisl, J. & Stephens, I. E. L. Toward an Active and Stable Catalyst for Oxygen Evolution in Acidic Media: Ti-Stabilized MnO2. *Adv. Energy Mater.* **5,** (2015).

48. Luo, Y., Tan, W., Suib, S. L., Qiu, G. & Liu, F. Dissolution and phase transformation processes of hausmannite in acidic aqueous systems under anoxic conditions. *Chem. Geol.* **487,** 54–62 (2018).

49. Chan, Z. M. *et al.* Electrochemical trapping of metastable Mn^{3+} ions for activation of MnO_2 oxygen evolution catalysts. *Proc. Natl. Acad. Sci. U. S. A.* **115,** E5261–E5268 (2018).

50. Zhou, L. *et al.* Rutile Alloys in the Mn-Sb-O System Stabilize Mn^{3+} to Enable Oxygen Evolution in Strong Acid. *ACS Catal.* **8,** 10938–10948 (2018).

51. Patel, P. P. *et al.* Noble metal-free bifunctional oxygen evolution and oxygen reduction acidic media electro-catalysts. *Sci. Rep.* **6,** 1–14 (2016).

52. Ghadge, S. D. *et al.* Computational and Experimental Study of Fluorine Doped $(Mn_{1-x}Nb_x)O_2$ Nanorod Electrocatalysts for Acid-Mediated Oxygen Evolution Reaction. *ACS Appl. Energy Mater.* **3,** 541–557 (2020).

53. Li, A. *et al.* Stable Potential Windows for Long-Term Electrocatalysis by Manganese Oxides Under Acidic Conditions. *Angew. Chemie - Int. Ed.* **58,** 5054–5058 (2019).

54. Moreno-Hernandez, I. A. *et al.* Crystalline nickel manganese antimonate as a stable water-oxidation catalyst in aqueous 1.0 M H_2SO_4. *Energy Environ. Sci.* **10,** 2103–2108 (2017).

55. Mondschein, J. S. *et al.* Crystalline Cobalt Oxide Films for Sustained Electrocatalytic Oxygen Evolution under Strongly Acidic Conditions. *Chem. Mater.* **29,** 950–957 (2017).

56. Huang, J., Sheng, H., Ross, R.D. *et al.* Modifying redox properties and local bonding of Co_3O_4 by CeO_2 enhances oxygen evolution catalysis in acid. *Nat Commun* **12**, 3036 (2021).

57. Chatti, M. *et al.* Intrinsically stable in situ generated electrocatalyst for long-term oxidation of acidic water at up to 80 °C. *Nat. Catal.* **2,** 457–465 (2019).

58. Qin, C., Ye, Z., Ma, G. & Li, D. Study on the Stability of Co x M 3-x O 4 (M = Ni, Mn and Ce) Nanowire Array Electrodes for Electrochemical Oxygen Evolution at Large Current Densities. *J. Electrochem. Soc.* **165,** A3496–A3503 (2018).

59. Yang, X. *et al.* Highly acid-durable carbon coated Co_3O_4 nanoarrays as efficient oxygen evolution electrocatalysts. *Nano Energy* **25,** 42–50 (2016).

60. Kwong, W. L., Lee, C. C., Shchukarev, A. & Messinger, J. Cobalt-doped hematite thin films for electrocatalytic water oxidation in highly acidic media. *Chem. Commun.* **55,** 5017–5020 (2019).

61. Huang, H. *et al.* Activation of transition metal oxides by in-situ electro-regulated structure-reconstruction for ultra-efficient oxygen evolution. *Nano Energy* **58,** 778–785 (2019).

62. Han, L. *et al.* Enhanced Activity and Acid pH Stability of Prussian Blue-type Oxygen Evolution Electrocatalysts Processed by Chemical Etching. *J. Am. Chem. Soc.* **138,** 16037–16045 (2016).

63. Li, A. *et al.* Enhancing the stability of cobalt spinel oxide towards sustainable oxygen evolution in acid. *Nat. Catal.* **5,** 109–118 (2022).

64. Wang, Z., Zheng, Y. R., Chorkendorff, I. & Nørskov, J. K. Acid-Stable Oxides for Oxygen Electrocatalysis. *ACS Energy Lett.* **5,** 2905–2908 (2020).

65. Hu, Q. *et al.* Coupling pentlandite nanoparticles and dual-doped carbon networks to yield efficient and stable electrocatalysts for acid water oxidation. *J. Mater. Chem. A* **7,** 461–468 (2019).

66. Hu, F. *et al.* Amorphous Metallic NiFeP: A Conductive Bulk Material Achieving High Activity for Oxygen Evolution Reaction in Both Alkaline and Acidic Media. *Adv. Mater.* **29,** 1–9 (2017).

67. Cheng, W. *et al.* A metal-vacancy-solid-solution NiAlP nanowall array bifunctional electrocatalyst for exceptional all-pH overall water splitting. *J. Mater. Chem. A* **6,** 9420–9427 (2018).

68. Kirshenbaum, M. J., Richter, M. H. & Dasog, M. Electrochemical Water Oxidation in Acidic Solution Using Titanium Diboride (TiB2) Catalyst. *ChemCatChem* **11,** 3877–3881 (2019).

69. Wu, J. *et al.* Exfoliated 2D Transition Metal Disulfides for Enhanced Electrocatalysis of Oxygen Evolution Reaction in Acidic Medium. *Adv. Mater. Interfaces* **3,** 1–6 (2016).

70. Najafi, L. *et al.* Carbon Nanotube-Supported MoSe 2 Holey Flake:Mo 2 C Ball Hybrids for Bifunctional pH-Universal Water Splitting. *ACS Nano* **13,** 3162–3176 (2019).

71. Blasco-Ahicart, M., Soriano-Lopez, J., Carbo, J. J., Poblet, J. M. & Galan-Mascaros, J. R. Polyoxometalate electrocatalysts based on earthabundant metals for efficient water oxidation in acidic media. *Nat. Chem.* **10,** 24–30 (2018).

72. Rodríguez-García, B. *et al.* Cobalt hexacyanoferrate supported on Sb-doped SnO_2 as a non-noble catalyst for oxygen evolution in acidic medium. *Sustain. Energy Fuels* **2,** 589–597 (2018).

73. Seitz, L. C. *et al.* A highly active and stable IrO_x /$SrIrO_3$ catalyst for the oxygen evolution reaction. *Science* **353,** 1011–1014 (2016).

74. Kwong, W. L., Lee, C. C., Shchukarev, A., Björn, E. & Messinger, J. High-performance iron (III) oxide electrocatalyst for water oxidation in strongly acidic media. *J. Catal.* **365,** 29–35 (2018).

75. Shinagawa, T., Garcia-Esparza, A. T. & Takanabe, K. Insight on Tafel slopes from a microkinetic analysis of aqueous electrocatalysis for energy conversion. *Sci. Rep.* **5,** 1–21 (2015).

76. Nørskov, J. K. *et al.* Trends in the Exchange Current for Hydrogen Evolution. *J. Electrochem. Soc.* **152,** J23 (2005).

77. Guan, Y. *et al.* Ganoderma-Like MoS_2/NiS_2 with Single Platinum Atoms Doping as an Efficient and Stable Hydrogen Evolution Reaction Catalyst. *Small* **14,** 1–6 (2018).

78. Zhang, J., Zhao, Y., Guo, X. *et al.* Single platinum atoms immobilized on an MXene as an efficient catalyst for the hydrogen evolution reaction. *Nat Catal* **1**, 985–992 (2018).

79. Wang, D. Y. *et al.* Highly active and stable hybrid catalyst of cobalt-doped FeS2 nanosheets-carbon nanotubes for hydrogen evolution reaction. *J. Am. Chem. Soc.* **137,** 1587–1592 (2015).

80. Deng, J., Ren, P., Deng, D. & Bao, X. Enhanced electron penetration through an ultrathin graphene layer for highly efficient catalysis of the hydrogen evolution reaction. *Angew. Chemie - Int. Ed.* **54,** 2100–2104 (2015).

81. Guo, Y., Shang, C. & Wang, E. An efficient CoS_2/$CoSe_2$ hybrid catalyst for electrocatalytic hydrogen evolution. *J. Mater. Chem. A* **5,** 2504–2507 (2017).

82. Chung, D. Y. *et al.* Large-Scale Synthesis of Carbon-Shell-Coated FeP Nanoparticles for Robust Hydrogen Evolution Reaction Electrocatalyst. *J. Am. Chem. Soc.* **139,** 6669–6674 (2017).

83. Zhou, W. *et al.* MoO_2 nanobelts@nitrogen self-doped MoS_2 nanosheets as effective electrocatalysts for hydrogen evolution reaction. *J. Mater. Chem. A* **2,** 11358–11364 (2014).

84. Huang, J. *et al.* MoS_2 nanosheet-coated CoS_2 nanowire arrays on carbon cloth as three-dimensional electrodes for efficient electrocatalytic hydrogen evolution. *J. Mater. Chem. A* **3,** 22886–22891 (2015).

85. Liao, L. *et al.* MoS_2 formed on mesoporous graphene as a highly active catalyst for hydrogen evolution. *Adv. Funct. Mater.* **23,** 5326–5333 (2013).

86. Tang, W. *et al.* Heterostructured Arrays of Ni_xP/S/Se Nanosheets on Co_xP/S/Se Nanowires for Efficient Hydrogen Evolution. *ACS Appl. Mater. Interfaces* **9,** 41347–41353 (2017).

87. Regmi, Y. N. *et al.* Lattice Matched Carbide-Phosphide Composites with Superior Electrocatalytic Activity and Stability. *Chem. Mater.* **29,** 9369–9377 (2017).

88. Feng, J. X., Tong, S. Y., Tong, Y. X. & Li, G. R. Pt-like hydrogen evolution electrocatalysis on PANI/CoP hybrid nanowires by weakening the shackles of hydrogen ions on the surfaces of catalysts. *J. Am. Chem. Soc.* **140,** 5118–5126 (2018).

89. Yan, H. *et al.* Phosphorus-Modified Tungsten Nitride/Reduced Graphene Oxide as a High-Performance, Non-Noble-Metal Electrocatalyst for the Hydrogen Evolution Reaction. *Angew. Chemie - Int. Ed.* **54,** 6325–6329 (2015).

90. Gong, Q., Wang, Y., Hu, Q. *et al.* Ultrasmall and phase-pure W_2C nanoparticles for efficient electrocatalytic and photoelectrochemical hydrogen evolution. *Nat Commun* **7**, 13216 (2016).

91. Wang, F. *et al.* Interface Engineered $W_xC@WS_2$ Nanostructure for Enhanced Hydrogen Evolution Catalysis. *Adv. Funct. Mater.* **27,** 1–7 (2017).

92. Wu, M. *et al.* Arrays of ZnSe/$MoSe_2$ Nanotubes with Electronic Modulation as Efficient Electrocatalysts for Hydrogen Evolution Reaction. *Adv. Mater. Interfaces* **4,** 2–9 (2017).

93. Cao, P., Peng, J., Li, J. & Zhai, M. Highly conductive carbon black supported amorphous molybdenum disulfide for efficient hydrogen evolution reaction. *J. Power Sources* **347,** 210–219 (2017).

94. Li, D. J. *et al.* Molybdenum sulfide/N-doped CNT forest hybrid catalysts for high-performance hydrogen evolution reaction. *Nano Lett.* **14,** 1228–1233 (2014).

95. Jin, B. *et al.* Aligned MoO_x/MoS_2 Core-Shell Nanotubular Structures with a High Density of Reactive Sites Based on Self-Ordered Anodic Molybdenum Oxide Nanotubes. *Angew. Chemie* **128,** 12440–12444 (2016).

96. Tang, H., Dou, K., Kaun, C. C., Kuang, Q. & Yang, S. $MoSe_2$ nanosheets and their graphene hybrids: Synthesis, characterization and hydrogen evolution reaction studies. *J. Mater. Chem. A* **2,** 360–364 (2014).

97. Yang, J. *et al.* Two-dimensional hybrid nanosheets of tungsten disulfide and reduced graphene oxide as catalysts for enhanced hydrogen evolution. *Angew. Chemie - Int. Ed.* **52,** 13751–13754 (2013).

98. Zhang, Z., Lu, B., Hao, J., Yang, W. & Tang, J. FeP nanoparticles grown on graphene sheets as highly active non-precious-metal electrocatalysts for hydrogen evolution reaction. *Chem. Commun.* **50,** 11554–11557 (2014).

99. Lei, Y. *et al.* Low-temperature Synthesis of Heterostructures of Transition Metal Dichalcogenide Alloys (WxMo1-xS2) and Graphene with Superior Catalytic Performance for Hydrogen Evolution. *ACS Nano* **11,** 5103–5112 (2017).

100. Lin, Y. *et al.* Graphene oxide co-doped with nitrogen and sulfur and decorated with cobalt phosphide nanorods: An efficient hybrid catalyst for electrochemical hydrogen evolution. *Electrochim. Acta* **222,** 246–256 (2016).

101. Naguib, M. *et al.* Two-dimensional nanocrystals produced by exfoliation of Ti_3AlC_2. *Adv. Mater.* **23,** 4248–4253 (2011).

102. Naguib, M., Mochalin, V. N., Barsoum, M. W. & Gogotsi, Y. 25th anniversary article: MXenes: A new family of two-dimensional materials. *Adv. Mater.* **26,** 992–1005 (2014).

103. Seh, Z. W. *et al.* Two-Dimensional Molybdenum Carbide (MXene) as an Efficient Electrocatalyst for Hydrogen Evolution. *ACS Energy Lett.* **1,** 589–594 (2016).

104. Kuznetsov, D. A. *et al.* Single Site Cobalt Substitution in 2D Molybdenum Carbide (MXene) Enhances Catalytic Activity in the Hydrogen Evolution Reaction. *J. Am. Chem. Soc.* **141,** 17809–17816 (2019).

105. Yuan, W. *et al.* MXene Nanofibers as Highly Active Catalysts for Hydrogen Evolution Reaction. *ACS Sustain. Chem. Eng.* **6,** 8976–8982 (2018).

106. Qu, G. *et al.* Phosphorized MXene-Phase Molybdenum Carbide as an Earth-Abundant Hydrogen Evolution Electrocatalyst. *ACS Appl. Energy Mater.* **1,** 7206–7212 (2018).

107. Jiang, Y. *et al.* Oxygen-Functionalized Ultrathin $Ti_3C_2T_x$ MXene for Enhanced Electrocatalytic Hydrogen Evolution. *ChemSusChem* **12,** 1368–1373 (2019).

108. Li, S. *et al.* Ultrathin MXene nanosheets with rich fluorine termination groups realizing efficient electrocatalytic hydrogen evolution. *Nano Energy* **47,** 512–518 (2018).

109. Yoon, Y. *et al.* Precious-Metal-Free Electrocatalysts for Activation of Hydrogen Evolution with Nonmetallic Electron Donor: Chemical Composition Controllable Phosphorous Doped Vanadium Carbide MXene. *Adv. Funct. Mater.* **29,** 1–12 (2019).

110. Li, X. *et al.* Edge-oriented, high-percentage 1T'-phase MoS_2 nanosheets stabilize Ti_3C_2 MXene for efficient electrocatalytic hydrogen evolution. *Appl. Catal. B Environ.* **284,** 119708 (2021).

111. Lim, K. R. G. *et al.* 2H-MoS_2 on Mo_2CT_x MXene nanohybrid for efficient and durable electrocatalytic hydrogen evolution. *ACS Nano* **14,** 16140–16155 (2020).

112. Tang, Y., Yang, C., Sheng, M., Yin, X. & Que, W. Synergistically Coupling Phosphorus-Doped Molybdenum Carbide with MXene as a Highly Efficient and Stable Electrocatalyst for Hydrogen Evolution Reaction. *ACS Sustain. Chem. Eng.* **8,** 12990–12998 (2020).

113. Yan, L., Zhang, B., Wu, S. & Yu, J. A general approach to the synthesis of transition metal phosphide nanoarrays on MXene nanosheets for pH-universal hydrogen evolution and alkaline overall water splitting. *J. Mater. Chem. A* **8,** 14234–14242 (2020).

114. Hu, L. *et al.* Experimental and theoretical investigation on MoS_2/MXene heterostructure as an efficient electrocatalyst for hydrogen evolution in both acidic and alkaline media. *New J. Chem.* **44,** 7902–7911 (2020).

115. Huang, J. J. *et al.* A facile method to produce $MoSe_2$/MXene hybrid nanoflowers with enhanced electrocatalytic activity for hydrogen evolution. *J. Electroanal. Chem.* **856,** 113727 (2020).

116. Tran, M. H. *et al.* Adding a New Member to the MXene Family: Synthesis, Structure, and Electrocatalytic Activity for the Hydrogen Evolution Reaction of $V_4C_3T_x$. *ACS Appl. Energy Mater.* **1,** 3908–3914 (2018)

Chapter 2. Polyoxymetalate-assisted MXenes: hybrid electrocatalysts for high-performance hydrogen evolution

2.1. Introduction

The water-splitting electrochemical system has two main reactions: the hydrogen evolution reaction (HER) and the oxygen evolution reaction (OER). HER is the reaction that takes place at the cathode in the water electrolyzer, and happens faster in acid with proton-rich environments[1,2]. The rate of H_2 production is determined by the activity of the HER electrocatalyst, and a high current density at the lowest possible potential is desirable. The benchmark HER electrocatalysts are made from noble metals or platinum-group metals (PGMs), typically Pt/C, because of their very low overpotentials required[3,4]. To lower the cost of electrode and electrolyzer fabrications, PGM-based catalyst usage must be minimized without losing the optimum HER activity.

Ni, Mo, and Co-based materials have been identified as potential catalysts to replace Pt/C for HER, including alloys such as NiMo, transition-metal chalcogenides, and phosphides[5,6]. And two-dimensional (2D) nanomaterials such as graphene and MXene have been well used as desirable supports to stabilize these catalysts to avoid aggregation and active area decrease, leading to better performances in their HER electrocatalytic processes[7-9]. MXenes, as a family of 2D transition metal carbides/nitrides, contain an abundance of termination groups on their basal planes that enable them to anchor molecular catalysts or nanoparticles, and facilitate their distribution[10,11]. Besides, their high conductivity helps to lower the electron transfer resistance, thereby enhancing the intrinsic HER activity.

Polyoxometalates (POMs) are a type of anionic transition metal-oxide clusters, with a wide range of shapes, sizes, and compositions[12]. The oxidation/reduction states of POMs are highly stable and can take part in fast reversible electron transfer reactions, leading to favorable characteristics for various electrochemical processes including hydrogen evolution[13]. Most POMs are good candidates as HER electrocatalysts in the homogeneous liquid phase because of their high solubility, electron and proton reservoir behaviors, but could only afford very low current densities,

far from large-scale hydrogen production[14-16]. In order to take advantage of POMs for HER heterogeneous electrocatalysis, anchoring and immobilizing them on a proper substrate would be an effective strategy.

However, limited efforts have been made to solve this problem[17-19]. For example, Kortz et al. used reduced oxided-graphene flasks to immobilize 3 kinds of POMs and built novel nanocomposite structures via a one-step electroreduction synthesis[18]. It was also reported that a robust supramolecular assembly of POMs on carbon nanotubes was prepared and then the POM/CNT hybrid materials were proved to work well as HER electrocatalysts[19]. Herein, a new strategy for creating nanocomposites that include POMs on 2D highly conductive material for hydrogen evolution reaction (HER) has been developed. For the first time, a novel hybrid nanostructure, Co containing POMs supported on a 2D MXene, has been introduced and found with high electrocatalytic performance for acidic HER. Representatively, as-prepared Co_9-POM/Ti_3C_2 exhibited excellent activity with ultralow overpotential of 56 mV at 10 mA cm^{-2} current density and long-term stability for HER electrocatalysis in 0.5 M H_2SO_4 solution.

2.2. Experimental sections

2.2.1. Synthesis.

A few-layered Ti_3C_2 MXene was created using a method outlined in previous research[20]. The process involved immersing 10 grams of Ti_3AlC_2 MAX phase material (Jinzhou Haixin Metal Materials, China) in a hydrofluoric acid solution (40% HF, Sigma-Aldrich) for 7 days with continually stirring under ambient conditions, then centrifugation and washing for a few times until the water reached a neutral pH. The sediment was collected and dried at 50°C in a vacuum oven. After that, 5 grams of $Ti_3C_2T_x$ MXene were mixed with tetrabutylammonium hydroxide (40% TBAOH, Sigma-Aldrich) using ultrasonication for 30 minutes (400 W), followed by repeated filtering and washing with distilled water. Finally, the resulting MXene was dried overnight in a vacuum oven at 50°C.

Co_4- and Co_9- POMs were prepared according to the methods reported[21,22]. Their molecular formulas are $Na_8K_8[Co_9(H_2O)_6(OH)_3(HPO_4)_2(PW_9O_{34})_3]\cdot 43H_2O$ (NaK[Co_9-POM]) and

$Na_5K_5[Co_4(H_2O)_2(PW_9O_{34})_2]\cdot 31H_2O$ (NaK[Co_4-POM]) respectively, and the molecular structure of the polyanions were shown in Figure 2.1. To obtain Co_x-POM (x=4, 9)/ Ti_3C_2, above-prepared Ti_3C_2 MXene was dispersed in ethanol (20 mg ml^{-1}), followed by adding 5 mg of each POM. After continuously stirring for 24 h at room temperature, the composite solid was obtained by centrifugation, washing with deionized water for several times, and subsequently dried for 5 h in the oven at 80 °C.

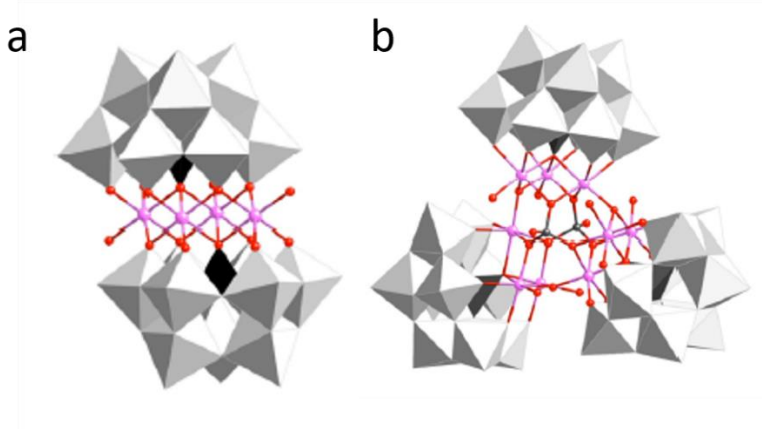

Figure 2.1. Representation of the molecular structure of the polyanions of (a) Co_4-POM and (b) Co_9-POM[22].

2.2.2. Electrochemistry.

All electrochemical experiments were performed under ambient conditions (~293 K) with a Bio-Logic VMP3 multichannel potentiostat and implemented with a three-electrode configuration using 0.5 M H_2SO_4 (pH 0.52) as filling solution, graphite rod as counter electrode, Ag/AgCl (3 M KCl) as reference electrode and carbon fiber paper (CFP, Sigracet 22 BB in FUELCELL Store) spray-coated with electrocatalyst as working electrodes (1 cm^2 surface area). The inks were prepared by sonicating 10 mg of catalyst, 5 µL Nafion 117 containing solution and 995 µL ethanol aqueous solution (3:1 in volume) for 30 mins. The actual mass amounts of the catalysts on CFP were measured with a weight balance. Before the test, the actual value of the potential vs. the reversible hydrogen electrode (RHE) of the reference electrode was calibrated by using a hydrogen electrode reaction with 40 wt% Pt/C on glassy carbon as the working electrode, a Ag/AgCl (3 M KCl) electrode as the

reference electrode, and platinum foil as the counter electrode in a hydrogen saturated electrolyte, as shown in Figure 2.2. It was calculated that the actual value of the potential of the Ag/AgCl (3 M KCl) was 0.24 V vs. the reversible hydrogen electrode (RHE) and the reported potential $E_{RHE} = E_{Ag/AgCl} + 0.24$ V. The overpotentials $\eta = - E_{RHE}$ V. All current densities were calculated based on the geometrical surface area of the electrodes. Ohmic drop (R) was determined by current interrupt (CI) method. iR-compensations were done all electrochemical data. Cyclic voltammetry (CV) experiments were carried out with 50 mV s^{-1} scan rate. Single linear sweep voltammetry (LSV) curve was recorded with a 1 mV s^{-1} scan rate for activity comparison after 20-cycle CV activation. Chronoamperometry tests were carried out at fixed potential of 0.6 V vs Ag/AgCl (3 M KCl). For the electrochemical double-layer capacitance (EDLC) measurements, the 100 mV potential windows were centered at open circuit potentials (OCPs) and cyclic voltammetries were then carried out under scanning rates of 10 to 300 mV s^{-1}. The current density differences between the minimum and maximum values at OCPs and the corresponding scanning rates were plotted to calculate the EDLC value (1/2 of the slope of current density-scan rate plots).

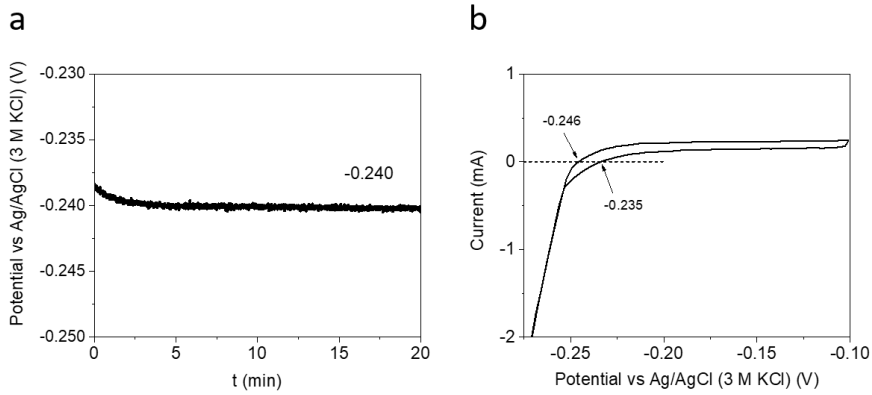

Figure 2.2. (a) Open circuit potential (OCP) value recording. (b) Calibration with cyclic voltammetry of the actual value of the potential of the Ag/AgCl (3 M KCl) vs. the reversible hydrogen electrode (RHE) by using a hydrogen electrode reaction with Pt/C (40 wt%)/GC, the Ag/AgCl electrode as the reference electrode, and carbon rod as the counter electrode in a hydrogen-saturated 0.5 M H_2SO_4 electrolyte.

2.2.3. Physical characterization.

Powder X-ray diffraction (PXRD) data were recorded with a Bruker D8 Advance Series equipped with a VANTEC-1 PSD3 detector. Energy-dispersive X-ray spectroscopy (EDX) was collected with a JEOL- JMS6400 environmental scanning electron microscope (SEM) equipped with an Oxford Instruments X-ray elemental analyzer.

2.3. Results and discussions.

2.3.1. Preparation of Co_9-POM/Ti_3C_2.

Firstly, Co_9-POM and Ti_3C_2 were separately synthesized according to the previous reports[20,21]. Scanning electron microscopy (SEM) image showed the layered nanosheet structure of Ti_3C_2 MXene and energy dispersive X-ray (EDX) elemental mapping images confirmed the uniform distribution of C, O, F and Ti within the whole 2D sheets (Figure 2.3a and Figure 2.4). In addition, Co_9-POM salt nanoparticles were exhibited in Figure 2.3b and the uniform distribution of O, Na, P, K, Co, W elements was also proven in Figure 2.5.

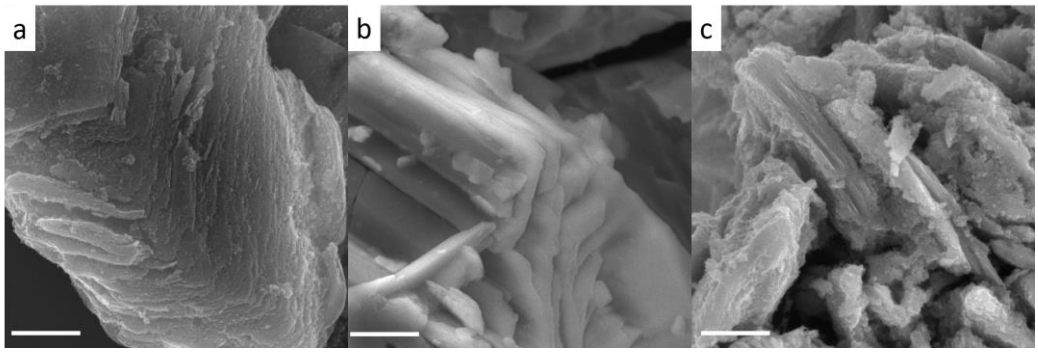

Figure 2.3. SEM images of (a) Ti_3C_2 MXene, (b) NaK[Co_9-POM] and (c) Co_9-POM/Ti_3C_2. Scale bar: 1 µm.

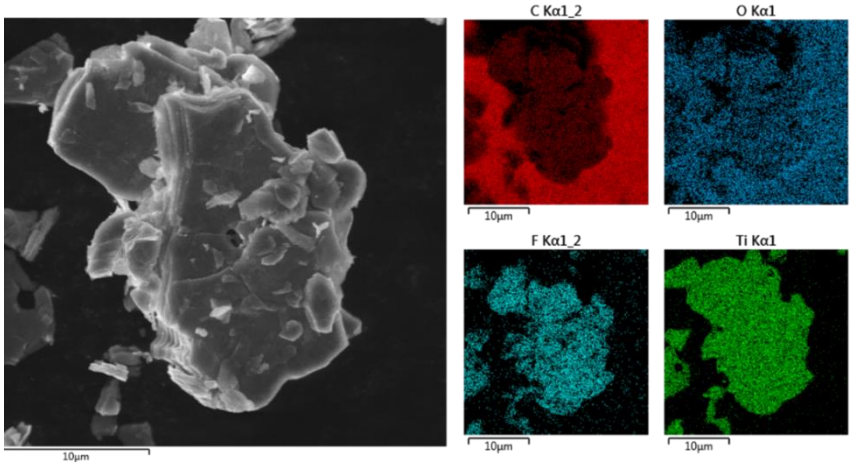

Figure 2.4. SEM image and energy dispersive X-ray (EDX) elemental mapping images of C, O, F, Ti within Ti_3C_2 MXene. Scale bar: 10 μm.

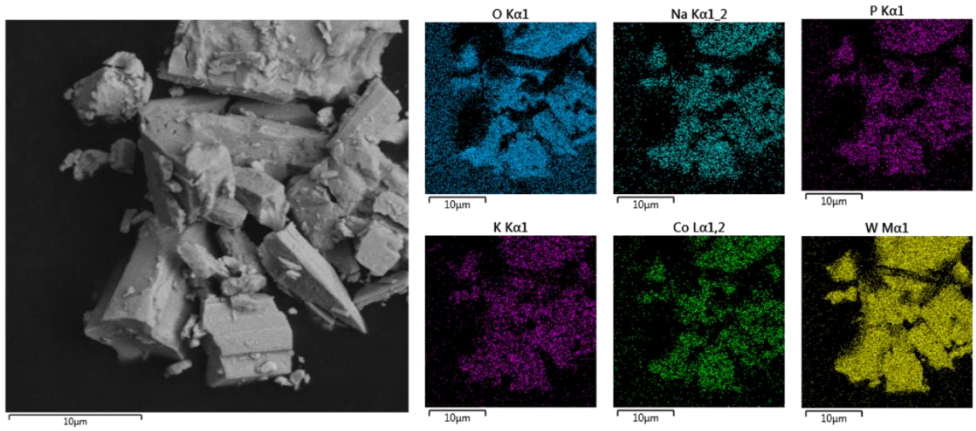

Figure 2.5. SEM image and EDX elemental mapping images of O, Na, P, K, Co, W within NaK[Co_9-POM]. Scale bar: 10 μm.

Then, a convenient one-step synthesis method was applied for the preparation of the Co_9-POM supported Ti_3C_2 MXene, Co_9-POM/Ti_3C_2 hybrid, as described in the **Experimental section**. After mixing NaK[Co_9-POM] salt and Ti_3C_2 MXene, Co_9-POM would be immobilized on the surface of Ti_3C_2 nanosheets by electrostatic attraction to replace other function groups, such as F^- or OH^-, which was illustrated in Figure 2.6. Compared with Ti_3C_2 MXene nanosheets, it showed the rougher surface with nanoparticles on the nanosheets for Co_9-POM/Ti_3C_2 (Figure 2.3c and 2.7). It was observed that the elements C, O, F, P, Ti, Co, W were dispersed uniformly in the EDX elemental mapping images (Figure 2.7). Besides, powder X-ray diffraction

(PXRD) pattern of Co_9-POM/Ti_3C_2 showed the characteristic peaks from Co_9-POM salt and Ti_3C_2 MXene, which further confirmed the obtained Co_9-POM/Ti_3C_2 hybrid. Similarly, Co_4-POM/Ti_3C_2 was also synthesized using this method.

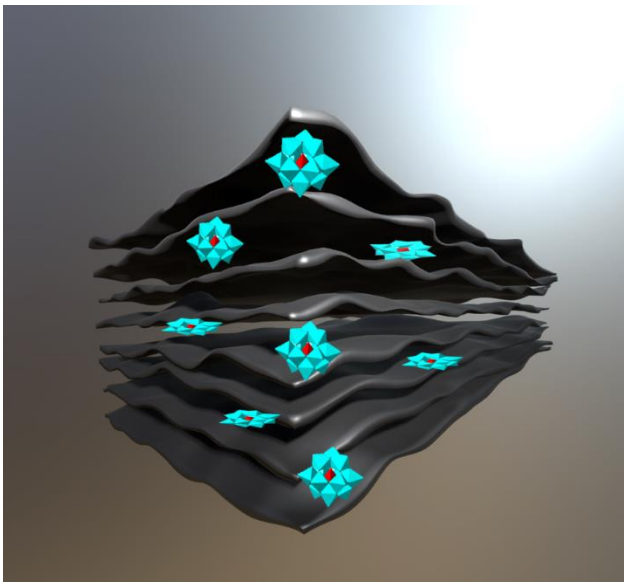

Figure 2.6. Schematic illustration of Co_9-POM/Ti_3C_2 hybrid.

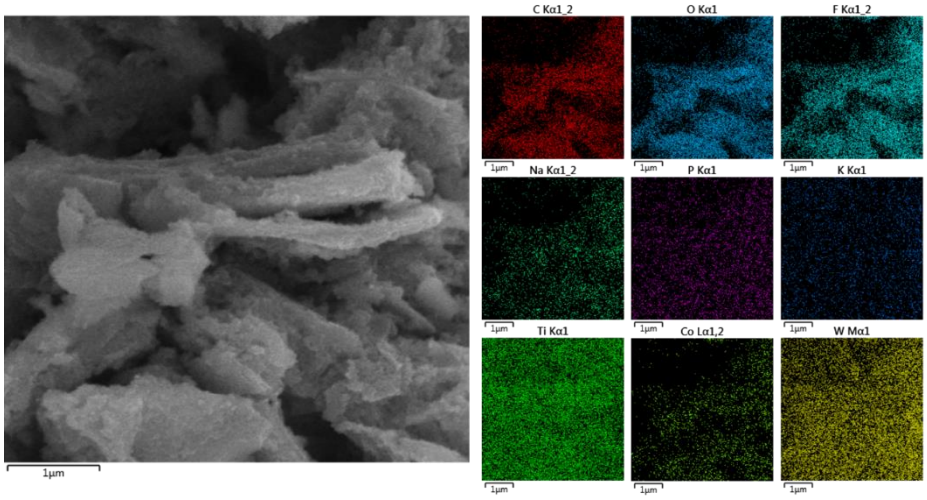

Figure 2.7. SEM image and EDX elemental mapping images of C, O, F, Na, P, K, Ti, Co, W within Co_9-POM/Ti_3C_2. Scale bar: 1 µm.

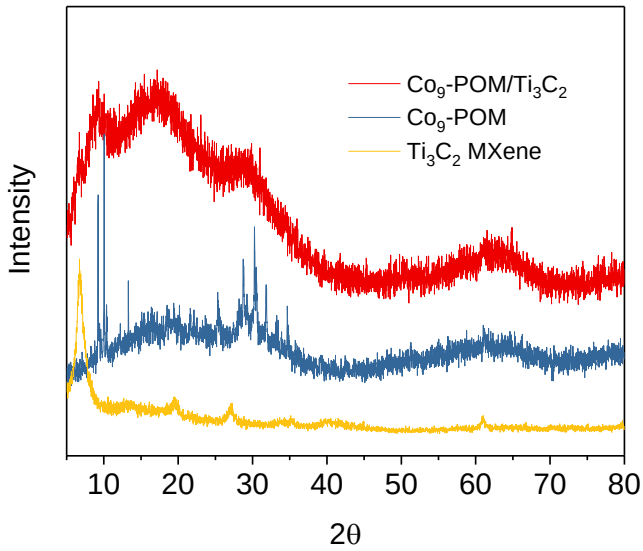

Figure 2.8. PXRD patterns of Co_9-POM/Ti_3C_2 (red), NaK[Co_9-POM] (blue) and Ti_3C_2 MXene (yellow).

2.3.2. Electrochemical HER evaluation of POMs/MXenes in acid.

Firstly, the electrocatalytic activities of Ti_3C_2 supporting Co-based POMs with different structure and nuclearity, Co_4-POM/Ti_3C_2 and Co_9-POM/Ti_3C_2 respectively, were evaluated and compared by applying representative iR-corrected polarization curves with a sweeping rate of 1 mV s^{-1}. It was shown in Figure 2.9 that the activity was much improved with lower potentials and higher currents when POMs supported on Ti_3C_2, compared to the blank Ti_3C_2 substrate. At most, Co_9-POM/Ti_3C_2 showed ~10-time improvement of current density at -0.4 V potential, which implied a positive assisting effect of Co containing POMs on the Ti_3C_2 MXene itself. Interestingly, Co_9-POM/Ti_3C_2 with higher nuclearity exhibited even better electrochemical activity than Co_4-POM/Ti_3C_2 with the lower nuclearity, which might come from more POM moles possessed within Co_9-POM/Ti_3C_2 per charge where POM anion bound with positively charged MXene substrate[17,22]. In addition, in the electrochemical double-layer capacitance (EDLC, C_{dl}) measurements (Figure 2.10), it was found that the C_{dl} value of Co_9-POM/Ti_3C_2 (154 mF cm^{-2}) was nearly double of 76 mF cm^{-2} of Co_9-POM/Ti_3C_2 and 5 times of 31 mF

cm^{-2} of Ti_3C_2 MXene, showing a much greater electrochemical active area within Co_9-POM/Ti_3C_2 and higher active site density.

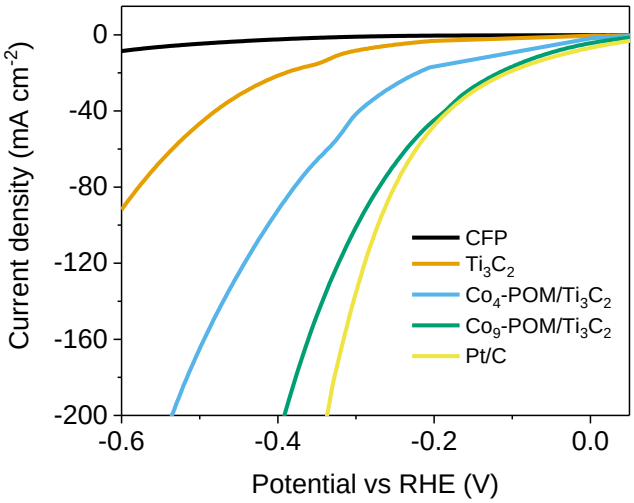

Figure 2.9. Electrocatalytic activities of Co_4-POM/Ti_3C_2, Co_9-POM/Ti_3C_2, Ti_3C_2, CFP and Pt/C electrodes in 0.5 M H_2SO_4 electrolyte.

For HER, the current density of interest corresponds to 10 mA cm^{-2} since this is the current density expected for a 12.3 % efficient solar to hydrogen device for photoelectrochemical water splitting in the solar water splitting process. So, generally, a relevant metric to compare the electrocatalysts is the overpotential required to reach an operating current density (j) of 10 mA cm^{-2}. To deliver 10 mA cm^{-2}, Co_9-POM/Ti_3C_2 showed an ultralow overpotential of 56 mV, much lower than 153 mV for Co_4-POM/Ti_3C_2, 316 mV for Ti_3C_2 MXene, respectively, and also outperformed other excellent MXene-based electrocatalysts in acid (Table 1.6). Besides, this overpotential was quite close to 33 mV required for Pt/C, showing a comparable activity of Co_9-POM/Ti_3C_2 to Pt/C. Moreover, a very low overpotential of only 393 mV was needed to reach a high current density of 200 mV cm^{-2}, indicating the high promise of Co_9-POM/Ti_3C_2 to be applied in the industrial scale.

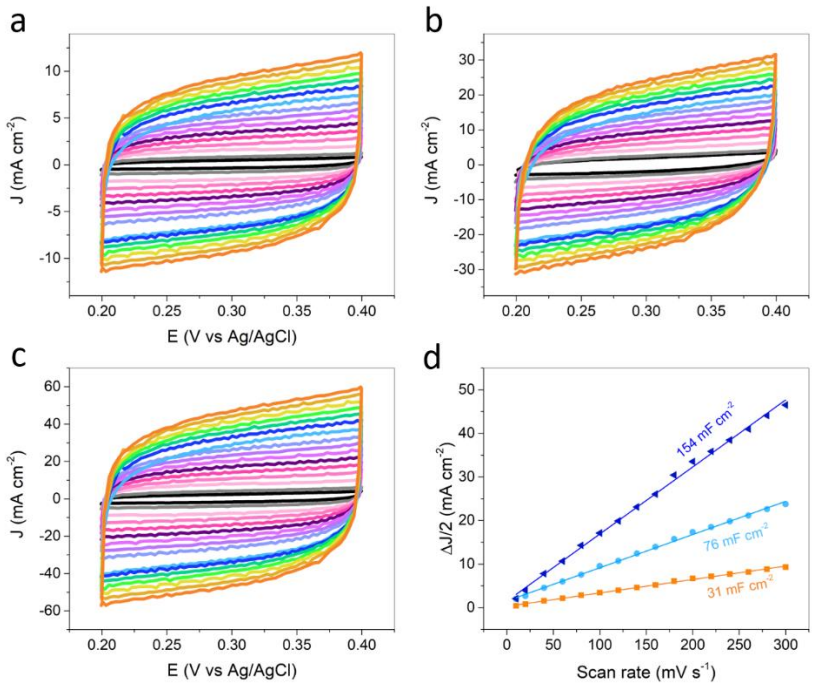

Figure 2.10. Electrochemical double-layer capacitance (EDLC) measurements: CV curves under different scan rates from 10 to 300 mV s^{-1} of (a) Ti_3C_2 MXene, (b) Co_4-POM/Ti_3C_2 and (c) Co_9-POM/Ti_3C_2; (d) The scan rate dependences of the current density differences Δ of Ti_3C_2 (orange), Co_4-POM/Ti_3C_2 (sky blue), Co_9-POM/Ti_3C_2 (navy blue).

Stability is another critical criterion for evaluating the efficient HER electrocatalysts. The chronoamperometry curve in Figure 2.11 showed that the current density of the HER process remained nearly constant without any obvious decrease even after 48 h. In addition, after long-term Chronoamperometry (CA) stability test, Co_9-POM/Ti_3C_2 exhibited a similar polarization curve (red curve) as before (blue curve) with negligible decay of the current density and increase of the overpotential (inset of Figure 2.11). These results implied the superior operational stability of Co_9-POM/Ti_3C_2 toward acidic HER in a long-term electrochemical process.

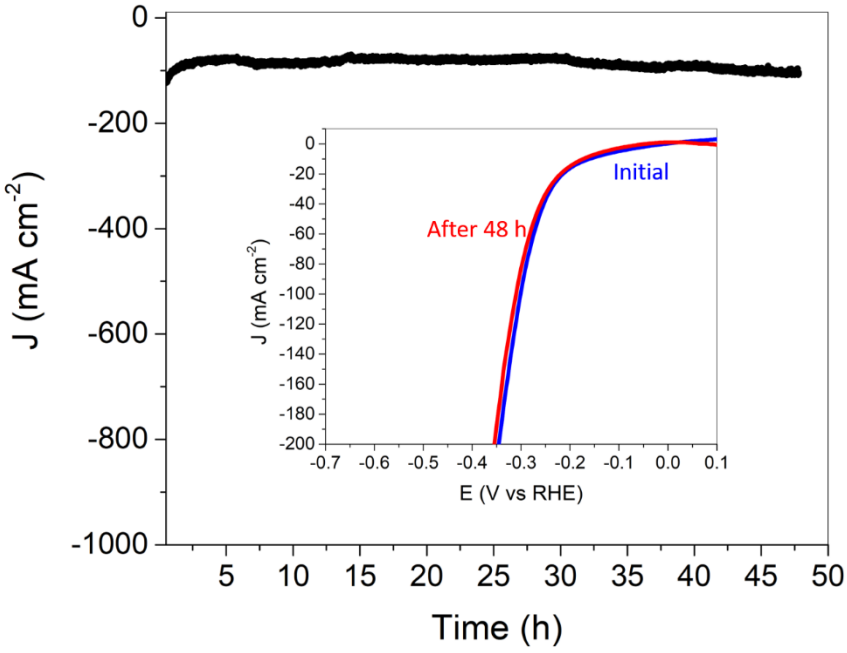

Figure 2.11. Chronoamperometry (CA) test for 48 h under the potential of -0.65 V vs Ag/AgCl (3 M KCl) and LSVs before and after CA measurement (Inset) for Co_9-POM/Ti_3C_2.

2.3.3. Conclusion.

In summary, we have developed a new technique for creating a novel hybrid nanocomposite that include POM nanoparticles on 2D MXene nanosheets. Representatively, as-prepared Co_9-POM/Ti_3C_2 exhibited excellent HER electrocatalytic performance in 0.5 M H_2SO_4 solution with much higher activity compared with Ti_3C_2 MXene and good stability for a long time. It opens an avenue for designing a highly efficient and durable non-precious-metal HER electrocatalysts in acidic medium with unique heterostructures.

2.4. References.

1. El-Refaei, S. M., Russo, P. A. & Pinna, N. Recent Advances in Multimetal and Doped Transition-Metal Phosphides for the Hydrogen Evolution Reaction at Different pH values. *ACS Appl. Mater. Interfaces* **13,** 22077–22097 (2021).

2. Zheng, Y., Jiao, Y., Vasileff, A. & Qiao, S. Z. The Hydrogen Evolution Reaction in Alkaline Solution: From Theory, Single Crystal Models, to

Practical Electrocatalysts. *Angew. Chemie - Int. Ed.* **57,** 7568–7579 (2018).

3. Shinagawa, T., Garcia-Esparza, A. T. & Takanabe, K. Insight on Tafel slopes from a microkinetic analysis of aqueous electrocatalysis for energy conversion. *Sci. Rep.* **5,** 1–21 (2015).

4. Nørskov, J. K. *et al.* Trends in the Exchange Current for Hydrogen Evolution. *J. Electrochem. Soc.* **152,** J23 (2005).

5. Anantharaj, S. et al. Recent trends and perspectives in electrochemical water splitting with an emphasis on sulfide, selenide, and phosphide catalysts of Fe, Co, and Ni: a review. *ACS Catal.* **6**, 8069–8097 (2016).

6. Ito, Y. *et al.* Cooperation between holey graphene and NiMo alloy for hydrogen evolution in an acidic electrolyte. *ACS Catal.* **8,** 3579–3586 (2018).

7. Tang, H., Dou, K., Kaun, C. C., Kuang, Q. & Yang, S. $MoSe_2$ nanosheets and their graphene hybrids: Synthesis, characterization and hydrogen evolution reaction studies. *J. Mater. Chem. A* **2,** 360–364 (2014).

8. Yang, J. *et al.* Two-dimensional hybrid nanosheets of tungsten disulfide and reduced graphene oxide as catalysts for enhanced hydrogen evolution. *Angew. Chemie - Int. Ed.* **52,** 13751–13754 (2013).

9. Seh, Z. W. *et al.* Two-Dimensional Molybdenum Carbide (MXene) as an Efficient Electrocatalyst for Hydrogen Evolution. *ACS Energy Lett.* **1,** 589–594 (2016).

10. Naguib, M. *et al.* Two-dimensional nanocrystals produced by exfoliation of Ti_3AlC_2. *Adv. Mater.* **23,** 4248–4253 (2011).

11. Naguib, M., Mochalin, V. N., Barsoum, M. W. & Gogotsi, Y. 25th anniversary article: MXenes: A new family of two-dimensional materials. *Adv. Mater.* **26,** 992–1005 (2014).

12. Wang, S. S. & Yang, G. Y. Recent Advances in Polyoxometalate-Catalyzed Reactions. *Chem. Rev.* **115,** 4893–4962 (2015).

13. Freire, C., Fernandes, D. M., Nunes, M. & Abdelkader, V. K. POM & MOF-

based Electrocatalysts for Energy-related Reactions. *ChemCatChem* **10,** 1703–1730 (2018).

14. Li, S. *et al.* First examples of hybrids based on graphene and a ring-shaped macrocyclic polyoxometalate: Synthesis, characterization, and properties. *Eur. J. Inorg. Chem.* 1882–1889 (2013).

15. Li, S. *et al.* Polyoxometalate-encapsulated twenty-nuclear silver-tetrazole nanocage frameworks as highly active electrocatalysts for the hydrogen evolution reaction. *Chem. Commun.* **54,** 1964–1967 (2018).

16. Lv, H. *et al.* Cu-based Polyoxometalate Catalyst for Efficient Catalytic Hydrogen Evolution. *Inorg. Chem.* **55,** 6750–6758 (2016).

17. Liu, R. *et al.* Enhanced proton and electron reservoir abilities of polyoxometalate grafted on graphene for high-performance hydrogen evolution. *Energy Environ. Sci.* **9,** 1012–1023 (2016).

18. Fernandes, D. M. *et al.* Polyoxometalate-graphene Electrocatalysts for the Hydrogen Evolution Reaction. *ChemElectroChem* **5,** 273–283 (2018).

19. Jawale, D. V. *et al.* Carbon nanotube-polyoxometalate nanohybrids as efficient electro-catalysts for the hydrogen evolution reaction. *Carbon* **188,** 523–532 (2022).

20. Alhabeb, M. *et al.* Guidelines for Synthesis and Processing of Two-Dimensional Titanium Carbide (Ti3C2Tx MXene). *Chem. Mater.* **29,** 7633–7644 (2017).

21. Weakley, T. J. R., Evans, H. T., Showell, J. S., Tourné, G. F. & Tourné, C. M. 18-Tungstotetracobalto (II)diphosphate and related anions: A novel structural class of heteropolyanions. *J. Chem. Soc. Chem. Commun.* 139–140 (1973).

22. Goberna-Ferrón, S., Vigara, L., Soriano-López, J. & Galán-Mascarós, J. R. Identification of a Nonanuclear $\{Co^{II}_9\}$ Polyoxometalate Cluster as a Homogeneous Catalyst for Water Oxidation. *Inorg. Chem.* **51,** 11707–11715 (2012).

Chapter 3. Sustainable oxygen evolution electrocatalysis in aqueous 1 M H_2SO_4 with earth abundant nanostructured Co_3O_4

3.1. Introduction

Hydrogen is considered the most environmentally friendly alternative fuel to replace traditional fossil energy[1,2]. However, hydrogen production is still dominated worldwide by natural gas steam reforming, a mature technology fixing a very low competitive price in the market. Electrochemical water splitting powered by renewable sources is regarded as the ideal future technology to produce hydrogen, but costs must be lowered to improve its market penetration[3,4]. The catalysts responsible to improve the efficiency of the process, mainly relying on noble metals, are part of the high cost of the technology, and because of this, many laboratories in the world are working to find viable solutions to develop effective, earth-abundant, robust and scalable catalyst[5-8].

Acidic electrolytes offer many advantages for hydrogen production, given that high H^+ concentration improves the hydrogen evolution reaction (HER), and also facilitates fast/low resistance ionic transport[9,10]. Several electrocatalysts based on low-cost raw materials have shown great promise to substitute the state-of-the-art platinum electrodes responsible for HER[6,7,11-14]. On the contrary, no viable candidates are known to substitute noble-metal oxides such as IrO_2 at the anode where the oxygen evolution reaction (OER) takes place[1,6,9,15-21]. So far, no stable and inexpensive OER catalysts can work under high potential and/or current densities in acidic media, where even the highly active RuO_2 presents serious deactivation problems[22,23].

Several strategies have been proposed to promote OER at high proton concentration[24-28]. One strategy deals with the investigation of ternary/complex oxide structures such as nickel-manganese antimonate. This rutile-type oxide was stable for 168 h at 10 mA cm^{-2} operating in 1 M sulfuric acid, although with the penalty of requiring a large overpotential ($\eta \geq 700$ mV)[26]. Cobalt-doped hematite thin-film electrocatalysts were also

able to sustain a geometric current density of 10 mA cm^{-2} for up to 50 h at pH 0.1, but again at large overpotentials ($\eta \geq 650$ mV)[27]. Indeed, cobalt oxides have shown promising OER electrocatalysis in acidic media, although highly limited by its redox potential-dependent instability, since CoO_x may rapidly dissolve either at open circuit conditions or under high applied potentials[29-32]. Some interesting advances in long-term stability were achieved by doping or processing techniques[33-35].

In our previous work with polyoxometalate (POM)-supported catalysts, we disclosed how these molecular catalysts showed promising OER catalytic performance in acidic conditions when incorporating active Co centers[36]. The high activity of these catalysts, even in heterogeneous conditions, was achieved thanks to the synergic stability offered by a partially hydrophobic carbon-based support. However, this strategy was not successful to achieve long-term stability, since these POM-based electrodes could only survive at low current densities and for a very limited time, given their intrinsic instability to the mechanical stress provoked by gas bubbling.

In this work, we present a promising processing protocol, which combines in one single anode two powerful strategies: (i) the incorporation of a nanostructured OER catalyst from earth-abundant metals to maximize active surface area, (ii) supported by a conducting, partially hydrophobic binder made from paraffin oil and graphite powder. Our processing protocol with nitrogen-doped carbon-coated Co_3O_4 nanoparticles (Co_3O_4@C) delivers robust and scalable anodes that exhibit excellent acidic OER performances, needing a minimum overpotential ($\eta \leq 398$ mV) to maintain a 10 mA cm^{-2} current density for >40 h when working in 1 M sulfuric acid solution, without any sign of fatigue or deactivation. The high activity and also great stability demonstrate a performance superior to any other non-noble catalysts reported. Oxygen evolution quantification confirms the Faradaic efficiency (>96%) of these electrodes towards OER, with negligible participation of other oxidation processes. These results open alternative opportunities for stable OER electrocatalysis with earth-abundant raw materials.

3.2. Experimental section

3.2.1. Synthesis.

All the chemical reagents and solvents were of commercial grade and used directly without any further purification Experimental Details.

ZIF-9 was prepared via a solvothermal method according to the previous literature with some modifications[37,38]. $Co(NO_3)_2 \cdot 6H_2O$ (0.175 g) and benzimidazole (0.142 g) were dissolved into 15 mL DMF and then the homogeneous solution was transferred into a Teflon-lined stainless autoclave. The sealed autoclave was put into an oven and kept at 140 °C for 24 h. When it was cooled down to room temperature, the purple product was filtered out and washed with acetone, and then dried at 60 °C.

To obtain the target material, Co@C was firstly synthesized using ZIF-9 as precursor by heating at 500 and then 750 °C for 2 h, respectively, under Ar flow while Co_3O_4 was obtained under air. Afterwards, the pyrolysis product was oxidized in air at 230 °C for 48 h to generate Co_3O_4@C.

The composite electrodes were prepared by 2-hour ball-milling at 20 s^{-1} of a mixture of paraffin oil (20 mg), graphite powder (80 mg) and the desired weight of metal oxide (5, 10, 20, 30 or 40 mg), namely, x-Co_3O_4@C/GPO. x-IrO_2/GPO (commercial IrO_2 from AlfaAesar), x-Co_3O_4/GPO and other oxide electrodes were also prepared using the same process for comparison purposes.

3.2.2. Electrochemistry.

Table 3.1. Ohmic drop values determined by the automatic current interrupt (CI) software and actual mass of catalysts in working electrodes.

	40-Co_3O_4@C/GPO	30-Co_3O_4@C/GPO	20-Co_3O_4@C/GPO	40-IrO_2/GPO	30-IrO_2/GPO	20-IrO_2/GPO
Ohmic drop (Ω)	19	37	27	25	28	25
Total electrode mass (mg)*	39.9	39.1	40.7	47.7	45.2	43.8
Total mass of Co_3O_4@C in the electrode (mg)*	11	9	7	14	10	7

*total mass of the composite: Co_3O_4@C + graphite + paraffin oil.

Table 3.2. Mass loading of catalysts in working electrodes.

Catalysts	Co_3O_4@C	IrO_2	Co_3O_4	NiO_x	FeO_x	$NiFeO_x$	$CoFeO_x$	$NiCoO_x$
Mass loading (mg cm^{-2})	20	25	19	24	20	22	23	22

All electrochemical experiments were performed under ambient conditions (~293 K) with a Bio-Logic VMP3 multichannel potentiostat and implemented with a three-electrode configuration using 1 M H_2SO_4 (pH 0.1) as filling solution, Pt mesh as counter electrode, Ag/AgCl (3 M KCl) as reference electrode and a pocket working electrode (0.07 cm^2 surface area and 4 mm depth) filled with the GPO composites. The actual mass amounts of the x-Co_3O_4@C/GPO composites in the electrode pocket were measured with a weight balance and are indicated in Table 3.1. Although it is difficult to estimate the actual active layer, an estimation is suggested that 1/8 of the total electrode pocket volume is used as the maximum limit in contact with the solution in order to determine the mass loading for comparison[36] (Table 3.2). All potentials were measured versus Ag/AgCl electrode and converted to the RHE reference scale using $E_{RHE} = E_{Ag/AgCl} + 0.21 + 0.059$ pH (V) while overpotentials $\eta = E_{RHE} - 1.23$ V. All current densities were calculated based on the geometrical surface area of the electrodes. Ohmic drop (R) was determined by using the automatic current interrupt (CI) software and the corresponding ohmic drops were included in Table 3.1. iR-compensations were done all electrochemical data. CV experiments were carried out with 10 or 100 mV s^{-1} scan rates. Single LSV curve was recorded with a 1 mV s^{-1} scan rate for activity comparison after 10-CV cycle activation. Tafel slopes were estimated from the LSV curves by plotting overpotential η vs log *j* (*j* = current density). The potential vs RHE to drive 1 mA cm^{-2} was used to define onset potential and corresponding η_{onset}. Chronopotentiometry tests were carried out at fixed current densities of 10 or 100 mA cm^{-2}. Accelerated degradation testing (ADT) was measured between 0-1.4 V vs Ag/AgCl using 100 mV s^{-1} scan rate[39]. For the electrochemical double-layer capacitance (EDLC) measurements, open circuit potentials (OCPs) vs. the Ag/AgCl were firstly recorded for 30 mins to reach rather stable values. Combined with above CV measurements, the 100 mV potential windows centered at OCPs could be determined and cyclic voltammetries were then carried out under scanning rates of 20, 40, 60, 80 and 100 mV s^{-1}. The current density

differences between the minimum and maximum values at OCPs vs. the Ag/AgCl and the corresponding scanning rates were plotted to calculate the EDLC value (1/2 of the slope of current density-scan rate plots)[40]. Co_3O_4@C and commercial Pt/C from AlfaAesar were also deposited on the glassy carbon (GC, 0.07 cm^{-2}) disk electrodes. The inks were prepared by sonicating 10 mg of catalyst, 25 µL Nafion 117 containing solution and 975 µL ethanol aqueous solution (3:1 in volume) for 30 mins.

High Electrochemical impedance spectroscopy (EIS) was performed by means of a typical three-electrode cell in the frequency range from 100 kHz to 0.1 Hz with 8 points per decade. The AC perturbation was 5 mV. Experimental data were fitted to the selected equivalent circuit model using Zview software (Scriber Associates) for extracting both capacitances and resistances.

3.2.3. Faradaic efficiency.

The experiment was performed under continuous flow conditions by bubbling Ar as carrier gas in both anodic and cathodic compartments. For this purpose, an H-type cell was used containing a frit glass separating both compartments, a connection for the sensor to be inserted in the anodic gas headspace, and connections for the inlet and outlet Ar streams in both compartments (Figure 3.1). The oxygen microsensor was in situ two-point calibrated by feeding to the H-cell with certified standard of Ar (≥ 99.999%) and compressed air, being the gas flow rate controlled by a set of mass flowmeters (Bronkhorst EL-FLOW).

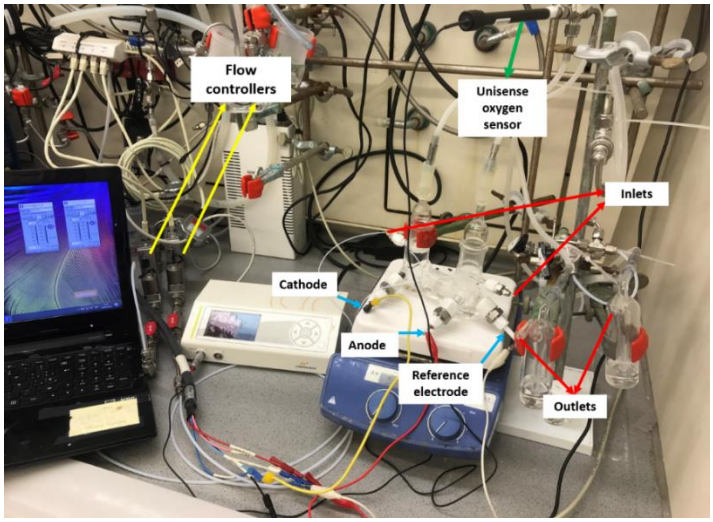

Figure 3.1. Setup for oxygen evolution measurement. It includes an H-type cell containing the Co_3O_4@C/GPO anode, carbon cathode and Ag/AgCl (3 M KCl) reference electrode connected to the potentiostat, the Unisense oxygen sensor connected to the anodic side headspace and the gas flow controlling system employed to feed Ar carrier gas to the cell.

After purging the cell headspace with argon, the chronopotentiometry test was started and the oxygen concentration was monitored until reaching stabilization while oxygen concentration in the headspace was in-situ measured by using an Unisense sensing system equipped with an oxygen microsensor based on voltage polarization (Figure 3.2). The expected faradaic oxygen production rate is calculated with the following equation:

$$F_{O_2,far} = I\, n_e^{-1} F^{-1}$$

Where *I* is the applied current (in A), n_e is the number of mols of electrons involved in the water oxidation reaction to generate one mol of oxygen (4) and *F* is the Faraday constant (96485 C mol^{-1}).

The experimental O_2 flow rate was calculated considering ideal gas behavior with the following equation:

$$F_{O_2,exp} = P\, C_{O_2}\, F_{Ar}\, (100 - C_{O_2})^{-1}\, R^{-1}\, T^{-1}$$

Where *P* is the total gas pressure (1 atm), *C* (O_2) is the steady-state oxygen concentration provided by the sensor (in %), F_{Ar} is the Ar carrier flow, *R* is

the ideal gas constant (0.082 atm L K^{-1} mol^{-1}) and *T* is the cell temperature (293 K).

Then Faradaic efficiency (in %), *FE*, is calculated as follows:

$$FE = \frac{100 \times F_{O_2,exp}}{F_{O_2,far}}$$

3.2.4. Physical characterization.

Powder X-ray diffraction (PXRD) data were recorded with a Bruker D8 Advance Series equipped with a VANTEC-1 PSD3 detector. Elemental analyses were carried out with an Agilent 725-ES inductively coupled plasma optical emission spectrometer (ICP-OES) at University of Valladolid (Co) and LECO CHNS-932 elementary microanalyzers (C, H, N) at Complutense University of Madrid. Thermogravimetric analysis was conducted with a thermogravimetric balance of Mettler Toledo. Nitrogen adsorption-desorption isotherms at 77 K were measured on a Quantachrome Autosorb iQ gas adsorption analyzer. Prior to analysis, the sample was degassed in vacuum. The BET method was applied to calculate the total surface area.

X-Ray photoemission (XPS) experiments were performed inside an ultra-high vacuum chamber (base pressure of 10^{-10} mbar) using a Phoibos 100 photoelectron spectrometer equipped with an Al Kα X-ray source (16 mA, 1486.6 V) as the incident photon radiation. XPS spectra of Co 2p, O 1s, N 1s, and C 1s core levels were measured for as received samples deposited on top of indium tape. The spectra are well described by the superposition of several Doniach-Sunjic curve-components. The intensities of the XPS core levels were evaluated by the peak areas, after a standard background subtraction according to Shirley procedure[41]. The spin-orbit splitting for every component into the Co-2p core level has been set to *D* = 15.2 eV with a branching ratio of 0.5. The metallic cobalt peak, Co $2p_{3/2}$=779.7 eV, was used for a final calibration of the spectra[42]. Co_3O_4@C/GPO after OER chronopotentiometry at 10 mA cm^{-2} for 2h at was washed with acetone in order to remove the paraffin oil prior to XPS measurements. As expected, the treatment do not affect the oxidation state of the composite, as evidenced by the measured spectra.

High resolution transmission electron microscopy (HRTEM) and scanning transmission electron microscopy (STEM) investigations were performed on a field emission gun FEI Tecnai F20 microscope. High angle annular dark-field (HAADF) STEM was combined with electron energy loss spectroscopy (EELS) in the Tecnai microscopy by using a GATAN QUANTUM energy filter in order to obtain compositional maps. STEM-EELS maps were performed using the O K-edge at 532 eV (green), the Co L-eadge at 779 eV (red) and C K-edge at 284 eV (blue).

3.3. Results and discussions

3.3.1. Catalyst and electrode preparation

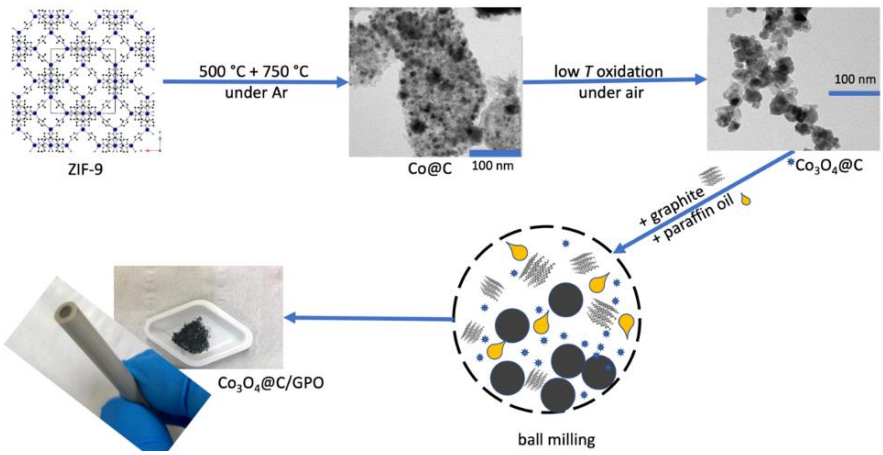

Figure 3.2. Electrode preparation. Scheme of the synthesis and processing protocol to obtain a Co_3O_4@C/GPO electrode.

The overall synthetic and processing protocol is summarized in Figure 3.2. We synthesized carbon-coated Co (Co@C) nanoparticles, starting from the thermal treatment of $Co(bIm)_2$ (bIm = 2-benzimidazolate), a metal-organic framework (MOF) precursor (ZIF-9)[43]. Then Co@C was oxidized at low-temperature to achieve its full transformation into cobalt oxide nanoparticles, covered by an amorphous, nitrogen-doped-carbon coating derived from the organic skeleton (Co_3O_4@C, Figure 3.2). Powder X-ray diffraction (PXRD) patterns and Raman spectra confirmed the presence of a

Co_3O_4 phase and the carbon support (Figure 3.3). High-resolution transmission electron microscopy showed the presence of graphitic-like nanostructures all around the sample, embedding the Co_3O_4 nanoparticles (Figure 3.4). Electron energy loss spectroscopy in scanning TEM mode (EELS-STEM) confirmed the chemical composition of the nanoparticles and surrounding nanostructures (Figure 3.5). The Co_3O_4@C composition was determined as $(Co_3O_4)(H_2O)_{0.30}(OH)_{0.85}C_{2.00}N_{0.05}$ by thermogravimetry elemental analysis (Figure 3.6 and Table 3.3).

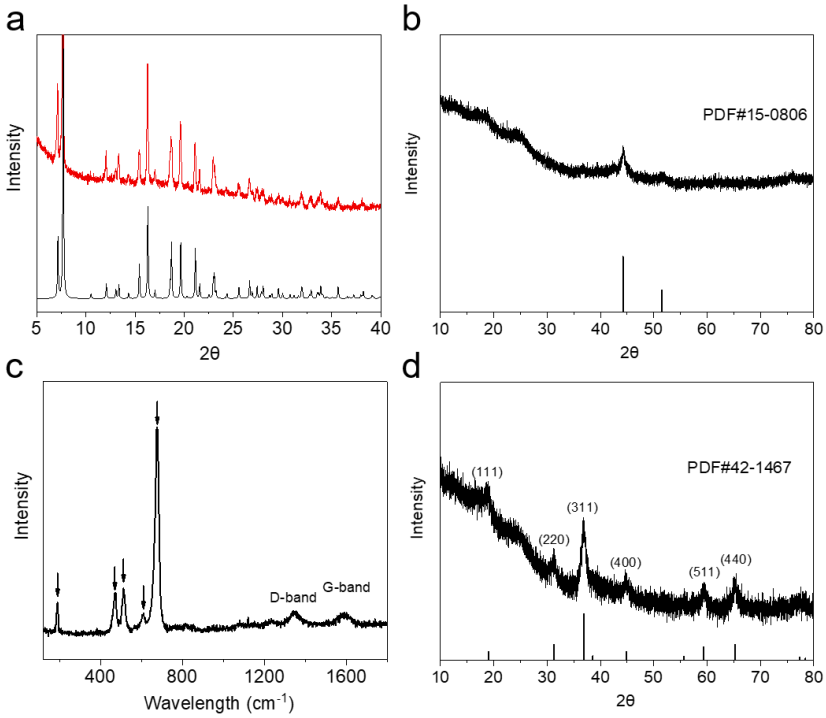

Figure 3.3. PXRD patterns of (a) as-synthesized ZIF-9 (red) and the one by Yaghi's group[44] (black), (b) Co@C. (c) Raman spectrum and (d) PXRD pattern for Co_3O_4@C.

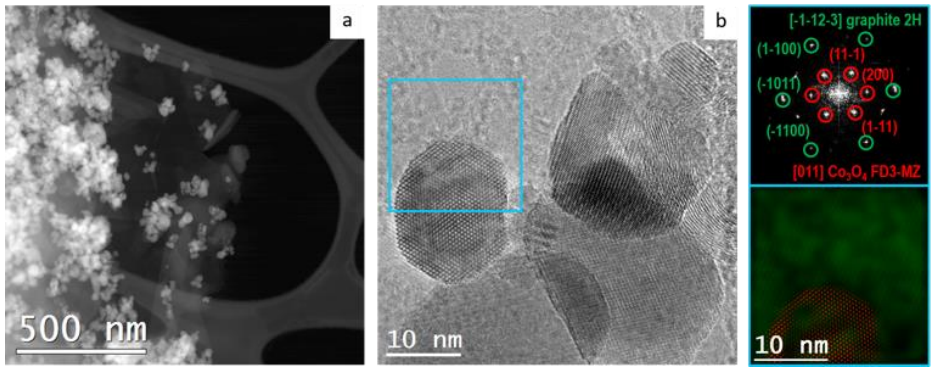

Figure 3.4. Structural and morphological characterization of Co_3O_4@C/GPO composites. HAADF STEM (a) and HRTEM (b) micrographs from a fresh Co_3O_4@C/GPO composite. The power spectrum analysis confirms the presence of Co_3O_4 nanoparticles with a cubic FD3-MZ (s.g. 227) spinel structure, oriented along its [011] axis (red circles) superimposed to the reflections corresponding to graphite layers with a ≈0.34 nm spacing and here oriented along the [–1–12–3] (green circles). To highlight the different systems, we show a frequency filtered map (on the bottom right) where the Co_3O_4 corresponding lattice fringes are in red and the graphite layer ones in green.

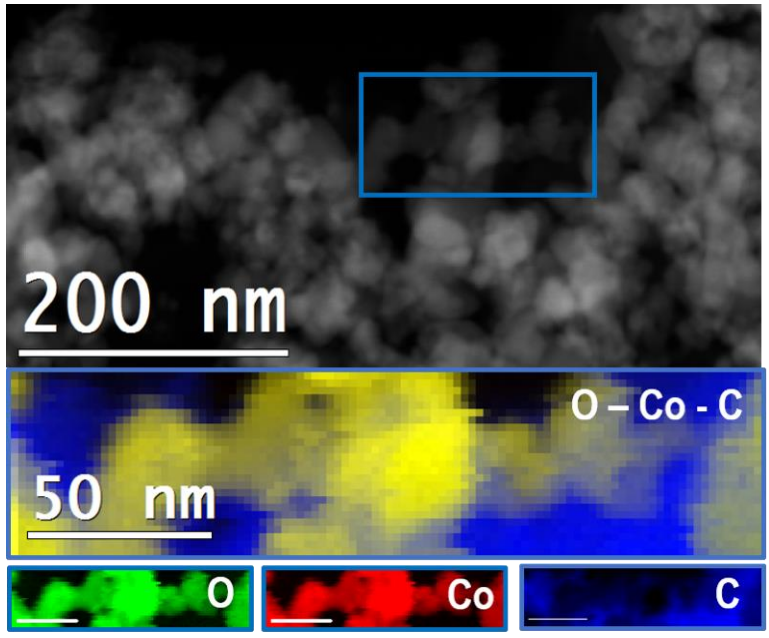

Figure 3.5. STEM-EELS elemental mapping for the as-prepared Co_3O_4@C.

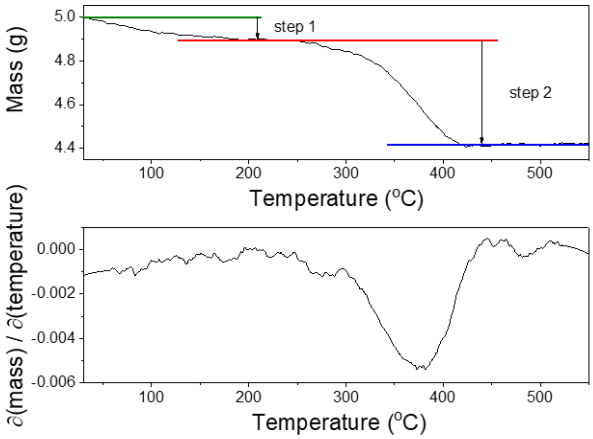

Figure 3.6. TGA curves of Co_3O_4@C with the heating rate of 10 °C min^{-1} in air. The step 1 shows the loss of water whose amount is 1.9 wt% while step 2 indicates the loss of carbon, nitrogen or other unstable species and further oxidation of Co_3O_4 to Co_2O_3 at the same time.

Table 3.3. The actual ratios of carbon, nitrogen, hydrogen and cobalt determined by elemental analysis.

	Carbon (wt%)	Nitrogen (wt%)	Hydrogen (wt%)	Cobalt (wt%)
Co_3O_4@C	8.28	0.26	0.47	62

For the preparation of the electrode composites, Co_3O_4@C was mixed with graphite (G) and paraffin oil (PO) in the desired ratio (see **Experimental section**) to prepare a homogeneous composite (Co_3O_4@C/GPO) with the desired Co_3O_4@C content up to 40% (40-Co_3O_4@C). HRTEM images and EELS-STEM maps showed similar nanostructures within Co_3O_4@C/GPO and close contact between Co_3O_4@C and GPO (Figure 3.4 and Figure 3.7). X-ray photoemission spectroscopy (XPS) analysis was employed to further identify the surface chemical composition and the mixed oxidation state $Co^{2+/3+}$ (Figure 3.8) consistent with the presence of the Co_3O_4, as confirmed by PXRD and HR-TEM data[42]. XPS spectra from the Co_3O_4@C/GPO composite show no differences respect to the Co_3O_4@C precursor, demonstrating the absence of chemical modification during composite preparation.

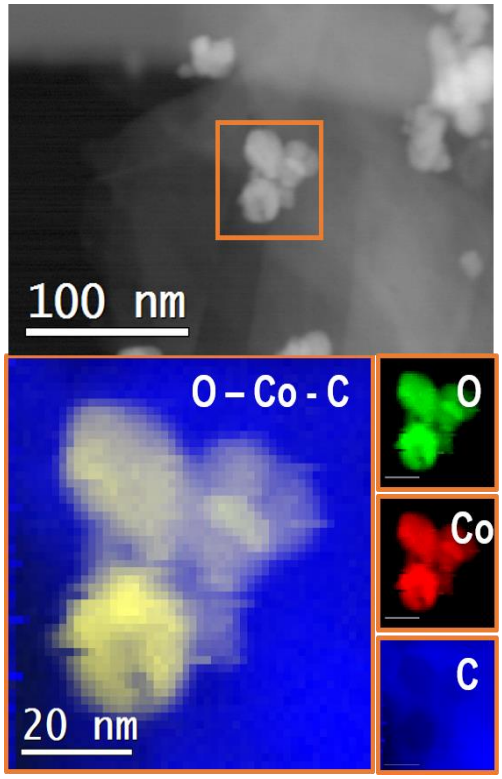

Figure S3.8. STEM-EELS elemental mapping for Co_3O_4@C/GPO.

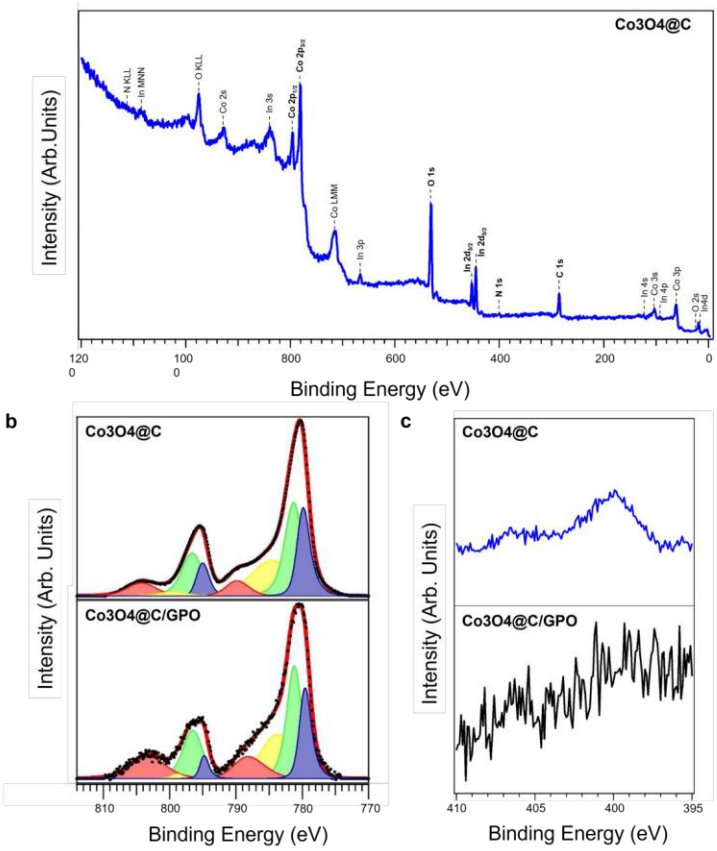

Figure 3.8. Chemical XPS characterization. (a) Overview spectrum of Co_3O_4@C catalyst with all the relevant core-levels attributed to the electrode composition (Co, O, N and C). No additional elements are identified, supporting the absence of cross-contamination of the catalyst. Indium (In) presence is justified since the samples were deposited onto and in tape for XPS measurement. (b) Co 2p XPS peak of the Co_3O_4@C (upper) and Co_3O_4@C/GPO (bottom) samples. No compositional changes are observed due to composite preparation. (c) N 1s XPS spectra of Co_3O_4@C (upper) and Co_3O_4@C/GPO (bottom) samples. Nitrogen detection in the system is below our resolution limit when the electrode composite is prepared.

3.3.2. OER electrocatalytic activity in 1 M H_2SO_4

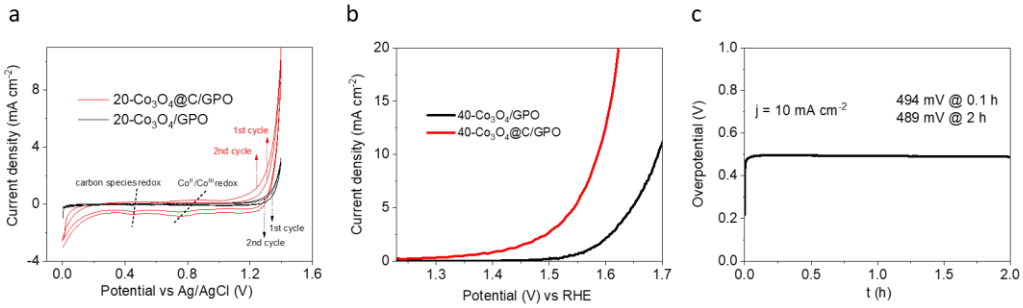

Figure 3.9. (a) CV curves of 20-Co_3O_4@C/GPO and 20-Co_3O_4/GPO, respectively. (b) LSV curves of 40-Co_3O_4@C/GPO and 40-Co_3O_4/GPO in 1 M H_2SO_4 electrolyte and (c) stability in chronopotentiometry measurements at 10 mA cm^{-2} of 40-Co_3O_4/GPO.

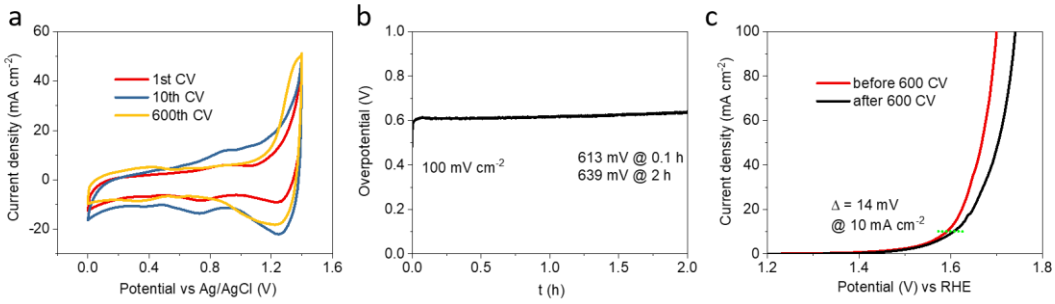

Figure 3.10. (a) CV curves of different cycles at 100 mV s^{-1}, (b) stability in chronopotentiometry measurements at 100 mA cm^{-2} and (c) LSV curves before and after 600 CV cycles of 40-Co_3O_4/GPO in 1 M H_2SO_4 electrolyte.

The *x*-Co_3O_4@C/GPO composites (*x* corresponds to the % in weight for the metal oxide) were inserted into the pocket of a working electrode and used as anode during electrochemical water oxidation in 1 M H_2SO_4 (pH ≈ 0.1). The cyclic voltammetry (CV) showed the appearance of a catalytic current density on the Co_3O_4@C/GPO electrode at relatively low overpotentials, which was sustained after successive cycling curves (Supplementary Figure 3.9 and 3.10). Comparative linear sweep voltammetry (LSV) showed an enhanced electrochemical activity upon increasing Co_3O_4@C content, reaching a very low onset overpotential (η_{onset} = 194 ± 4 mV) for the 40-Co_3O_4@C/GPO electrode (Figure 3.11a and Figure 3.12). These electrodes reach 10 mA cm^{-2} currents at just 360 ± 4 mV overpotential. Interestingly, no sign of a transport-limited regime appeared in the studied potential

range, reaching over 20 mA cm^{-2} at η = 397 ± 4 mV. A current density limit of 100 mA cm^{-2} was found in these *x*-Co_3O_4@C/GPO electrodes.

We prepared analogous IrO_2/GPO working electrodes to benchmark our results in the same conditions with the state-of-the-art IrO_2. The IrO_2/GPO anodes delivered higher overpotentials, $\eta_{j=10\ mA\ cm^{-2}}$ = 368 mV at 10 mA cm^{-2} and $\eta_{j=20\ mA\ cm^{-2}}$ = 396 mV at 20 mA cm^{-2}, slightly above those obtained for the Co_3O_4@C-based electrode (Figure 3.11b and Table 3.4).

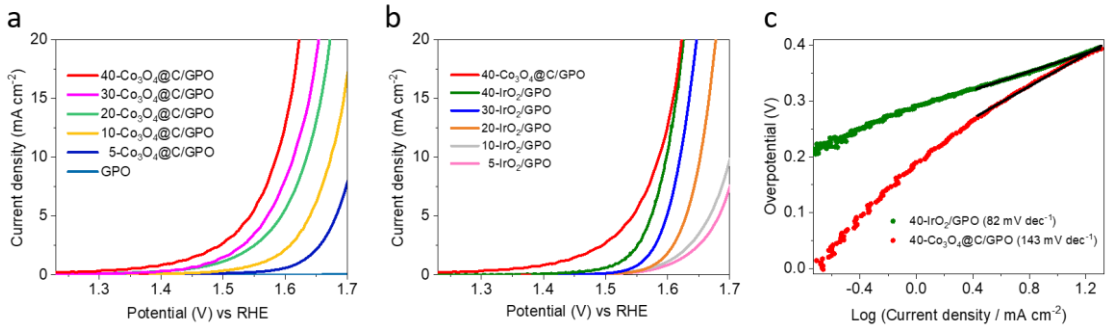

Figure 3.11. Electrocatalytic activity of Co_3O_4@C/GPO electrodes in 1 M H_2SO_4 electrolyte. (a) LSV curves for x-Co_3O_4@C/GPO electrodes in 1 M H_2SO_4 (pH 0.1), at *x* = 0 (GPO blank, light blue), 5 (blue), 10 (yellow), 20 (green), 30 (pink), 40 (red) and with 1 mV s^{-1} scan rate; (b) LSV curves of x-IrO_2/GPO electrodes in 1 M H_2SO_4 (pH 0.1), at *x* =5 (pink), 10 (grey), 20 (orange), 30 (blue), 40 (green) compared to 40-Co_3O_4@C/GPO (red); (c) Tafel plots of IrO_2/GPO (green) and Co_3O_4@C/GPO (red) extracted from LSV data.

Table 3.4. OER activity for working electrodes from LSV curves in 1 M H_2SO_4 (pH 0.3).

	η (mV) @ 1 mA cm^{-2}	η (mV) @ 5 mA cm^{-2}	η (mV) @ 10 mA cm^{-2}	η (mV) @ 20 mA cm^{-2}
40-Co_3O_4@C/GPO	190	313	356	393
40-IrO_2/GPO	291	344	368	396

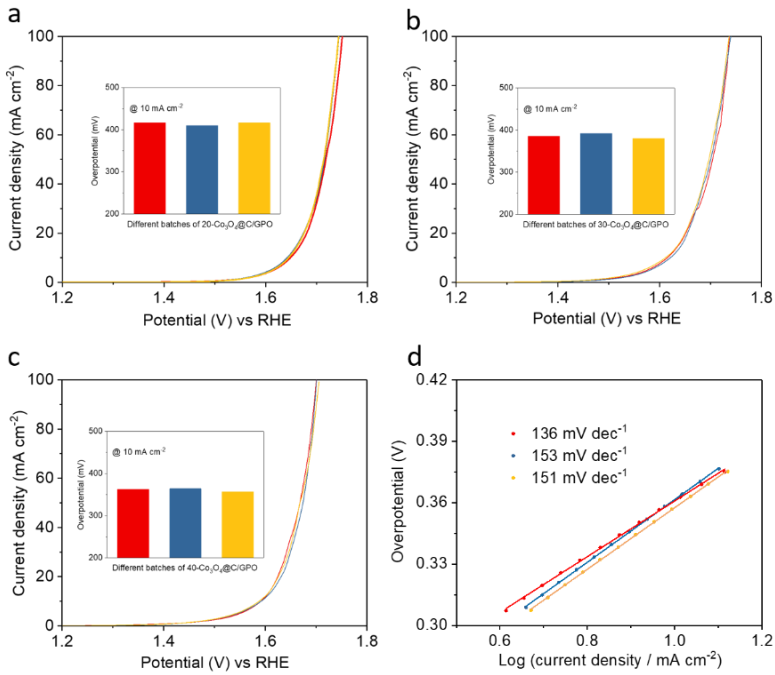

Figure 3.12. LSV curves of 3 different batches of (a) 20-Co_3O_4/GPO, (b) 30-Co_3O_4/GPO, (c) 40-Co_3O_4/GPO with corresponding overpotentials for 10 mA cm^{-2} in 1 M H_2SO_4 electrolyte inserted, respectively. (d) The Tafel plots of 40-Co_3O_4@C/GPO extracted from LSV data in (c).

Tafel analyses of the LSV data yielded slopes of 139 mV dec^{-1} for Co_3O_4@C and 83 mV dec^{-1} for IrO_2 (Figure 3.11c), suggesting a different reaction mechanism (rate-limiting step) for these two catalysts, and indicating a faster increment of current density with the applied potential for IrO_2[44,45]. Interestingly, this is compensated by the lower onset potential of Co_3O_4@C/GPO. The electrochemical double-layer capacitance (EDLC) of Co_3O_4@C/GPO and IrO_2/GPO were calculated as 25 and 2 mF cm^{-2}, respectively, with 0.03 mF cm^{-2} for the blank GPO (Figure 3.13). This indicates a greater electrochemical active surface area for Co_3O_4@C/GPO, due to its higher density of active sites in Co_3O_4@C/GPO, thanks to its nano-structuration, favouring the higher current densities observed in the potential range studied[46,47]. It is important to point out that nanostructured IrO_2 can perform significantly better than our IrO_2/GPO electrodes[20,48,49].

This must be related to the relatively low electrochemical surface area (ECSA) of our IrO_2/GPO composite. When we normalize current densities vs ECSA (Figure 3.14a), IrO_2/GPO electrodes reach higher values at lower potentials. Still, the Co_3O_4@C catalyst remains competitive as a non-noble metal catalysts, and especially when current density is normalized per gram (Figure 3.14b), as a more practical parameter for applications.

Finally, we measured anodic oxygen evolution during chronopotentiometry experiments with Co_3O_4@C/GPO electrodes (Figure 3.15). We found over >96% Faradaic efficiency, confirming that OER is the dominant process at these electrodes' surface, and confirming no significant oxidation of the carbon-based matrix is taking place in these conditions.

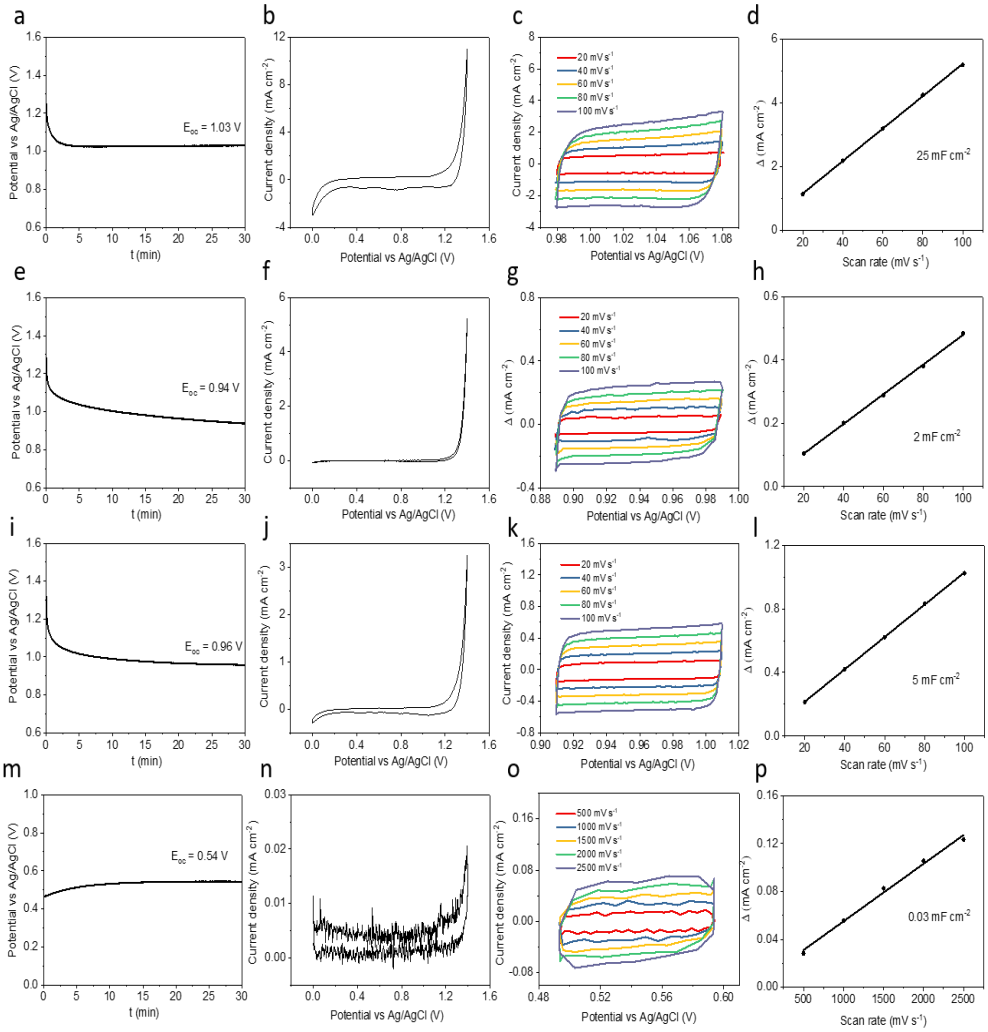

Figure 3.13. Electrochemical double-layer capacitance (EDLC) measurements: OCP (vs Ag/AgCl) values recording within 30 mins of (a) 20-Co_3O_4@C/GPO, (e) 20-IrO_2/GPO, (i) 20-Co_3O_4/GPO and (m) GPO; CV curves under 10 mV s^{-1} scan rate of (b) 20-Co_3O_4@C/GPO, (f) 20-IrO_2/GPO, (j) 20-Co_3O_4/GPO and (n) GPO; CV curves under different scan rates of (c) 20-Co_3O_4@C/GPO, (g) 20-IrO_2/GPO, (k) 20-Co_3O_4/GPO and (o) GPO; The scan rate dependences of the current density differences Δ of (d) 20-Co_3O_4@C/GPO, (h) 20-IrO_2/GPO, (l) 20-Co_3O_4/GPO and (p) GPO. Note: the current density for GPO electrode under 100 mV s^{-1} was very low and hardly detected so higher scan rates (from 500 to 2500 mV mV s^{-1}) were used to obtain clear value for EDLC determination.

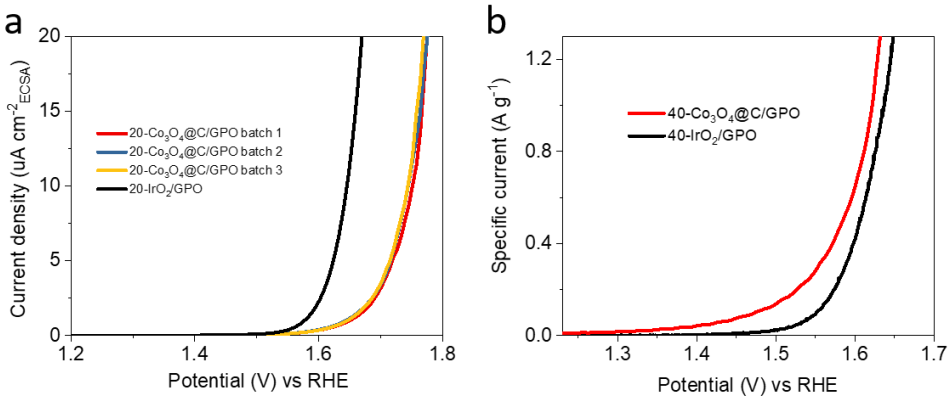

Figure 3.14. Comparative potential dependence of the ECSA (a) and mass specific current for IrO_2/GPO and Co_3O_4@C/GPO (b). The electrochemically active surface area (ECSA) was calculated by dividing the electrochemical double-layer capacitance C_{dl} by the specific capacitance C_s of the sample: ECSA = C_{dl} / C_s while a value of 0.035 mF cm^{-2} was suggested for C_s in the reference[6].

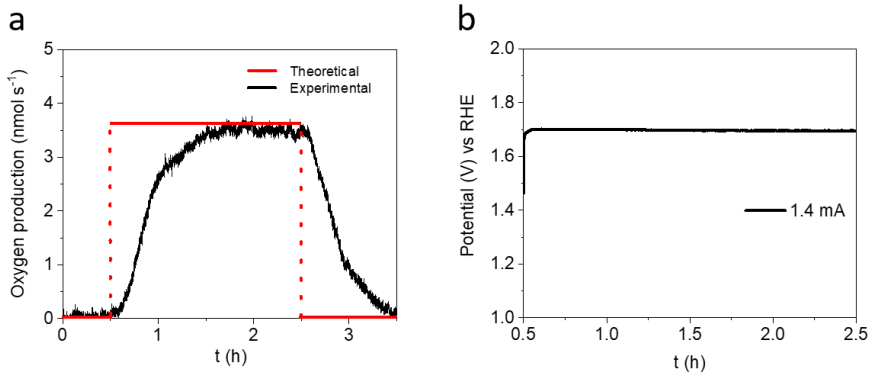

Figure 3.15. Time evolution of oxygen production rate in the cell headspace during a chronopotentiometry at 1.4 mA for 2 hours, using 3.3 mL min^{-1} of Ar stream as sweep gas at 20 ºC and 1 atm. Once the chronopotentiometry starts, the O2 signal rapidly increases, reaching a 3.6 nmol s^{-1} production of O_2 in steady state conditions (reached after 1 hour of operation). This corresponds to a 99% Faradaic efficiency. After the chronopotentiometry, the oxygen signal rapidly decreases, as the chamber is purged with Ar. Integration of all the O_2 detected over time, yields a total of 24.9 µmol of O_2 that corresponds to ≥ 96% of Faradaic efficiency. (b) Chronopotentiometry test for 2 h.

3.3.3. OER electrocatalytic stability in 1 M H_2SO_4.

As mentioned before, stability is a critical issue for earth abundant OER catalysts in acidic media[50-54]. To determine the stability of our Co_3O_4@C/GPO electrodes, we take advantage of the benchmarking protocol designed by Jaramillo's group that uses as figure of merit the overpotential required to achieve and maintain a 10 mA cm^{-2} current density, as this is approximately the current density expected at the anode in a 12.3% efficient solar water-splitting device under 1 sun illumination.[6,55] The corresponding chronopotentiometry data (Figure 3.16a-c) show very good stability for all electrodes, independently of their Co_3O_4@C content. In all cases, $\eta_{j=10\ mA\ cm^{-2}}$ after 2 hours shows just a small increment. In the case of our best electrodes, the 40-Co_3O_4@C/GPO, this increment is of just 3 mV, and the stability is maintained for long times. After 43 h of continuous electrolysis, the overpotential is essentially identical to the starting value (Figure 3.16a). Meanwhile, even to keep 100 mA cm^{-2} current density, only 27 mV increment was needed after 2 h catalysis (Figure 3.10b). We also applied more aggressive stability tests under cycling applied potentials. In this accelerated degradation testing (ADT), complete CV cycles were collected, thus exposing the electrodes sequentially to catalytic and non-catalytic potentials. These conditions simulate better the different degradation mechanisms during electrode and electrolyzer operation. The 40-Co_3O_4@C/GPO electrodes showed also good stability after ~600 CV cycles with only a 14 mV increment in the overpotential to reach a 10 mA cm^{-2} current density (Figure 3.11c).

The benchmarking of these electrodes with previous literature is highlighted in the $\eta_{j=10\ mA\ cm^{-2},t=2\ h}$ vs $\eta_{j=10\ mA\ cm^{-2},t=0\ h}$ plot (Figure 3.16d). This comparative plot illustrates the high activity and stability of our electrodes. The three of them appear at the diagonal of the graph, as expected for sustainable performance, and very close and competitive to the results obtained with noble metal counterparts. For the first time, earth abundant anodes successfully pass this benchmarking protocol for OER performance in acidic media.

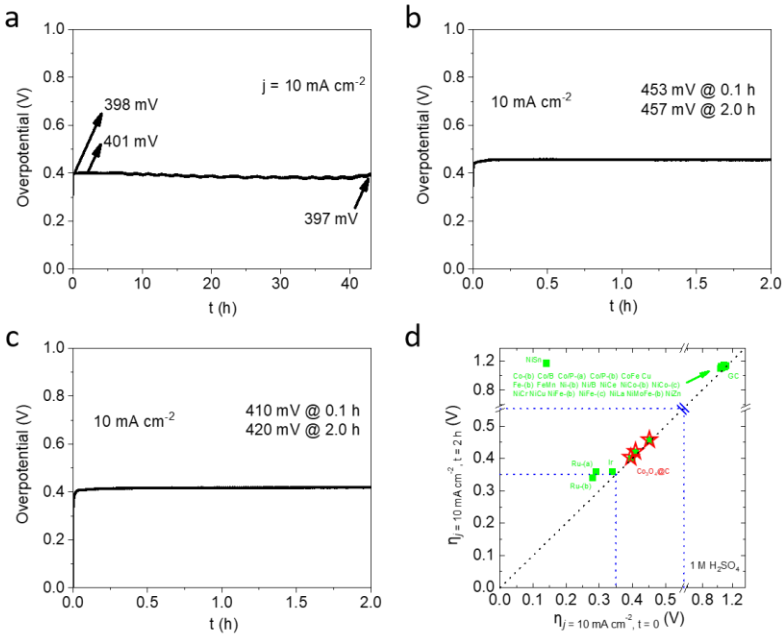

Figure 3.16. Electrochemical stability of Co_3O_4@C/GPO electrodes. Chronopotentiometry measurements at j = 10 mA cm^{-2} in 1 M H_2SO_4 electrolyte. (a) 40-Co_3O_4@C/GPO (> 40 hours). (b) 20-Co_3O_4@C/GPO (2 hours). (c) 30-Co_3O_4@C/GPO (2 hours). (d) Benchmarking of their activity/stability features (red stars) in comparison with other OER electrocatalysts (green squares) in the same electrolysis conditions according to the data from a previous benchmarking study[6].

Stability number (S-number) and Activity-Stability Factor (ASF) were also proposed as key metrics for estimating lifetime and long-term stability for electrocatalysts[56-58]. Thus, we analyzed the electrolyte after stability tests to check for Co leaching (Table 3.5). We found the presence of Co but at the ppb level, corresponding to just ≈ 0.4 % of the total. Based on this number, we can estimate a 25 S-number, an ASF of 101 and a lifetime of 462 h. These estimations are comparable even to Ir-based catalysts such as $SrIrO_3$ in analogous conditions, and confirm the promising performance/stability of these electrodes. It is worthy to mention that this small Co loss does not significantly affect performance. This may be due to Co leaching only from non-catalytically areas, or to the 3D nature of our electrodes. Thus, after leaching, the new surface exposed brings additional active sites,

keeping the performance. Both may explain why activity is so stable, but a relatively modest S-number is obtained.

Table 3.5. Elemental analysis (ICP-MS) of cobalt before and after 2 h electrocatalytic water oxidation at a constant current density of 10 mA cm^{-2} in 1 M H_2SO_4 of 40 mL.

	Cobalt amount (µg/L)
1 M H_2SO_4 before	–
1 M H_2SO_4 after	756

3.3.4. Post-electrolysis Co_3O_4@C/GPO characterization.

To further confirm the stability of Co_3O_4@C as a genuine OER catalyst, we characterized the structural and chemical evolution of the electrodes after these 2 h electrolysis at 10 mA cm^{-2} in 1 M H_2SO_4. The powder XRD patterns did not show any significant change nor shift in the observed peaks, still typical of Co_3O_4@C and graphite (Figure 3.17). This suggests no major structural changes are occurring to the bulk of the material Co_3O_4@C.

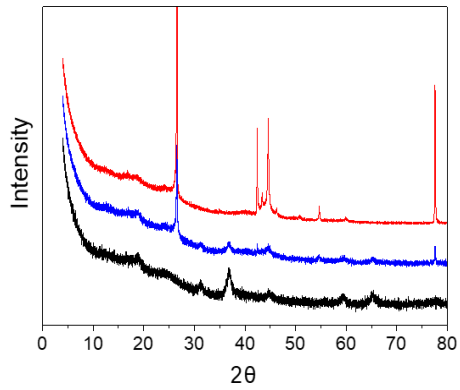

Figure 3.17. PXRD patterns of Co_3O_4@C (black), Co_3O_4@C after 2h catalysis, washed with acetone to remove paraffin oil (blue) and commercial graphite (red).

We explored potential changes on the chemical composition of the catalyst due to OER process by XPS characterization of the fresh electrode and after water electrolysis under different conditions. The Co 2p XPS spectrum of the fresh Co_3O_4@C/GPO electrode (Figure 18a) shows two peaks located at 794.9 eV (Co $2p_{1/2}$) and 779.7 eV (Co $2p_{3/2}$), corresponding to the spin-orbit

splitting of the 2p orbital. Both components contain equivalent chemical information.

The deconvoluted analysis of the peaks reveals the presence of two different chemical components, which we attribute to the Co^{3+} (blue) and Co^{2+} (green) states, in agreement with the presence of Co_3O_4[38]. In addition, we observe two doubled satellite peaks arising from charge transfer and final states effects from Co^{2+} (satellite A, yellow) and Co^{3+} (satellite B, red),[59] again characteristic of Co_3O_4. We also analyzed the O 1s peak (Figure 3.18a). In addition to the Co-O component (brown) related to the Co_3O_4, we observe a higher binding energy component attributed to residual OH/H_2O (pink). Quantitative analysis of the Co 2p and O 1s core levels of Co_3O_4@C/GPO after chronopotentiometry at 10 mA cm^{-2} for 2 h (Figure 3.18b) and 5 mA cm^{-2} for 24 h (Figure 3.18c) revealed no shifts in the binding energies of the components respect to the fresh sample. Crucially, the main spectral features attributed to a Co_3O_4@C catalyst remain unaltered after water electrolysis, which demonstrates the preservation of the oxidation state of the catalyst. Changes in the intensity of the OH/H_2O component on the O 1s can be fairly attributed to the different environmental conditions of the emersed electrode (see **Experimental section**). XPS analysis of the C component does not evidence significant changes in the oxidation state of the C 1s peak, supporting the preservation of the carbon-based matrix (Figure 3.19) in agreement to the obtained Faradaic efficiencies. Nitrogen detection in the system is below our resolution limit; therefore, no discussion is referred to this element. Based on the current analysis, the most important finding is that the oxide film is stable and no cobalt oxide is lost nor further oxidized during the electrolysis process. In summary, XRD and XPS strongly support the bulk and surface stability of Co_3O_4@C before and after acidic OER electro catalysis, and its genuine catalytic activity.

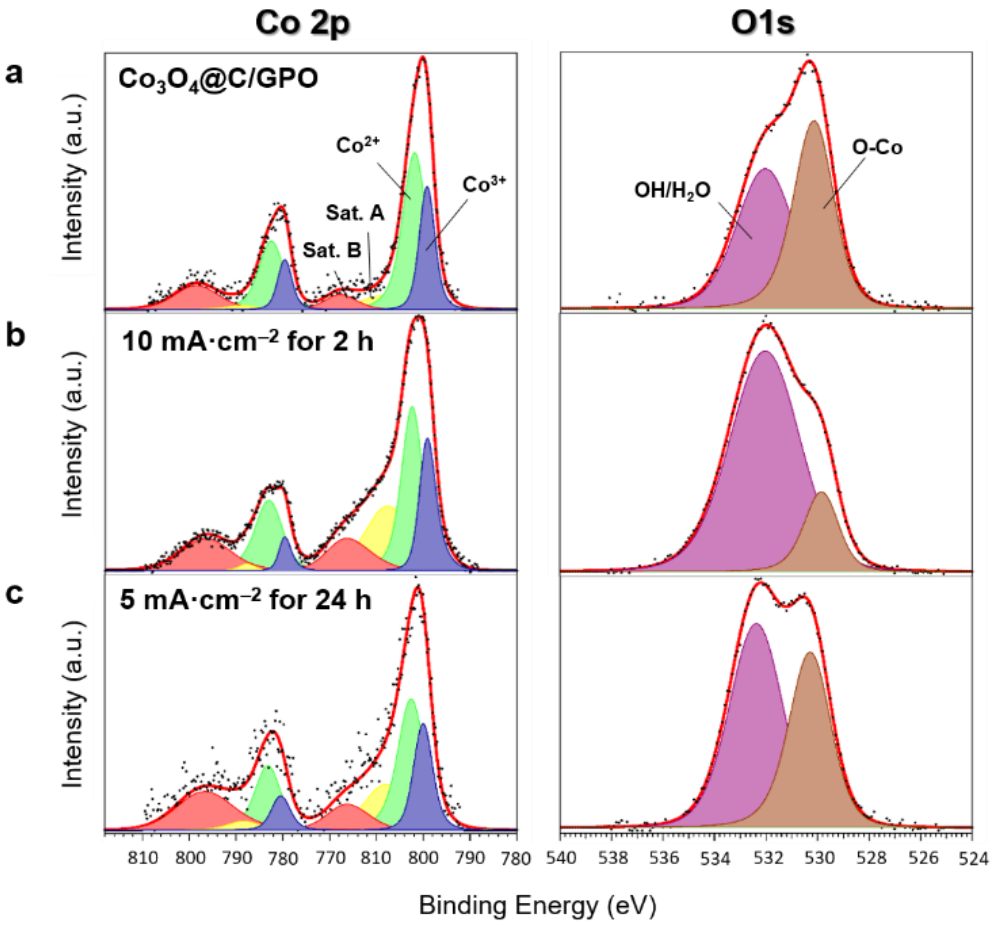

Figure 3.18. Chemical analysis of the Co_3O_4@C/GPO catalyst after water electrolysis. (a) X-ray photoelectron spectra of the Co 2p (left) and O 1s (right) core levels for a 20-Co_3O_4@C/GPO electrode. (b) Same spectra for a 20-Co_3O_4@C/GPO electrode after OER chronopotentiometry at 10 mA cm^{-2} for 2 h. (c) Same spectra for a 20-Co_3O_4@C/GPO electrode after OER chronopotentiometry at 5 mA cm^{-2} for 24 h. Colour assignment for the different areas: Co^{3+} (violet); Co^{2+} (green), OH/H_2O (purple), O–Co (brown).

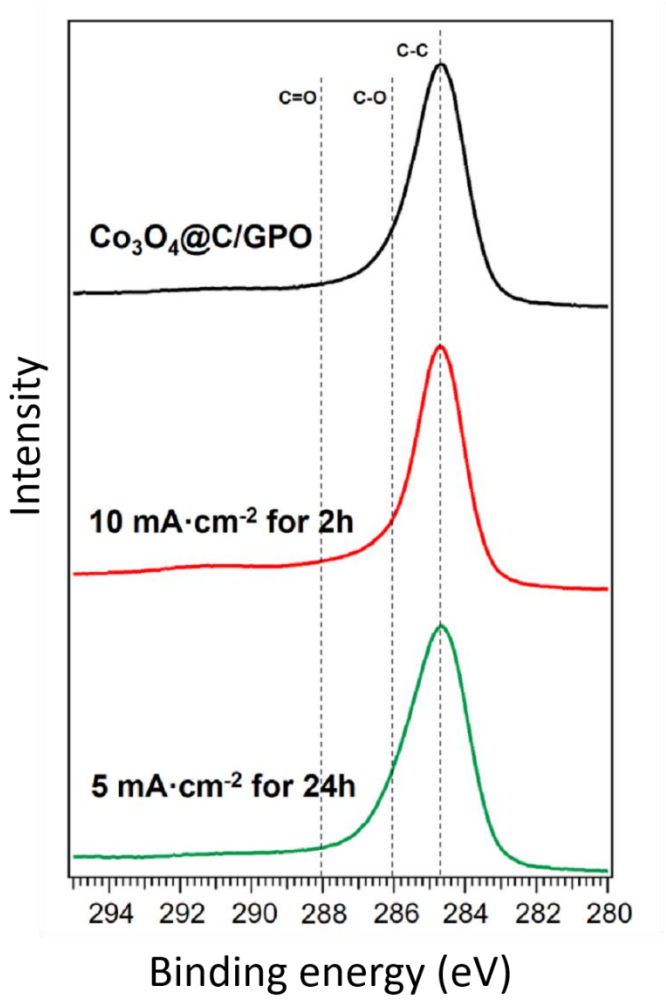

Figure 3.19. C1s XPS spectrum of Co_3O_4@C/GPO (black), Co_3O_4@C/GPO after 2h of electrolysis at 10 mA·cm^{-2} (red) and Co_3O_4@C/GPO after 24h of electrolysis at 5mA·cm^{-2} (green).

We also investigated the Co_3O_4@C/GPO composite after 2 h electrolysis at 10 mA cm^{-2} by means of HR-TEM (Figure 3.20). The images and power spectra (FFT) analyses also confirm a high structural and chemical stability. Neither crystallinity nor particle size are affected by the electrochemical process.

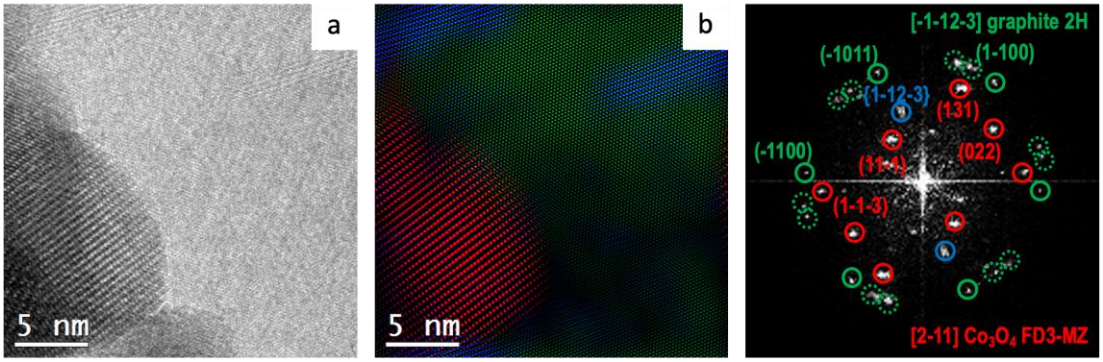

Figure 3.20. Structural and morphological characterization of Co_3O_4@C/GPO electrodes after water electrolysis in 1 M H_2SO_4 electrolyte. HRTEM micrograph (a) from a Co_3O_4@C/GPO composite, recovered after 2 h water electrolysis at 10 mA cm^{-2}. To highlight the different systems, we show a frequency filtered map (b) where the Co_3O_4 nanoparticle lattice fringes are in red and the ones corresponding to the surrounding graphitic layers in green and blue. The power spectra (FFT) confirm the high stability of these electrodes, showing again Co_3O_4 nanoparticles with a cubic FD3-MZ (s.g. 227) spinel structure (red cirlces) here oriented along the [2–11] zone axis. No changes in crystallinity or particle size are observed for the Co_3O_4@C composite when compared to the fresh samples (Figure 3.4). Notice that the graphitic layers may show multiple rotated domains as shown by the highlighted dotted green circles in the power spectrum, but this effect also happened in the as-prepared sample.

3.3.5. Critical role of GPO.

To investigate the actual role of the carbon paste in the stability of the electrodes, we carried out additional alternative experiments. First, we directly deposited Co_3O_4@C on a glassy carbon (GC) electrode as a Nafion-based ink. This electrode showed a significantly lower electrocatalytic activity when compared with the Co_3O_4@C/GPO (Figure 3.11, 3.16 vs Figure 3.21). More importantly, after 30-min of the benchmarking test in 1 M H_2SO_4, the Co_3O_4@C/GC electrode is apparently deactivated. This suggests that the GPO binder is fundamental to confer the acidic stability and activity of the Co_3O_4@C component.

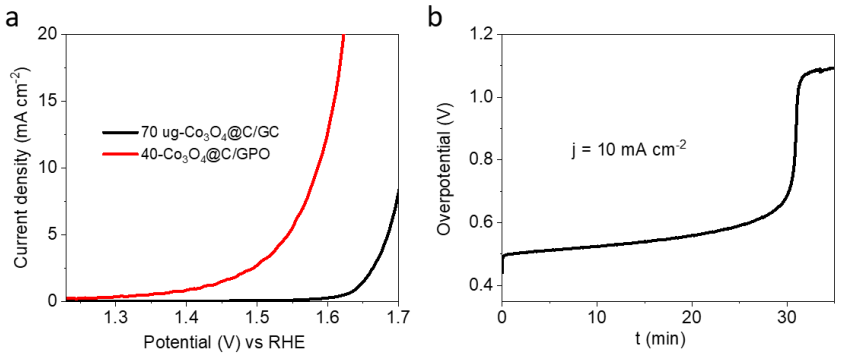

Figure 3.21. (a) LSV curves of 40-Co_3O_4@C/GPO and 70 ug-Co_3O_4@C/GC in 1 M H_2SO_4 electrolyte. (b) Chronopotentiometry measurement of 70 ug-Co_3O_4@C/GC at 10 mA cm^{-2}.

This effect of the GPO binder could be due to a modified local pH at the electrode/electrolyte interface[60-62]. To check this hypothesis, we decided to investigate the effect of the GPO binder on the local pH through the reversible H^+/H_2 pair as catalyzed with commercial Pt/C[63]. The reversible potential for this model reaction differs when the Pt/C is directly deposited on a graphite electrode, or when incorporated into a GPO electrode as observed in their CV plots in a hydrogen saturated 1 M H_2SO_4 electrolyte (Figure 3.22). An average value of –0.002 V vs E_{RHE} was estimated for the Pt/C catalyst, in good agreement with the theoretical +0.0 V value. A +0.031 V vs E_{RHE} was found for the (Pt/C)/GPO electrode. If we associate this potential difference only to a theoretical local pH difference, $\Delta E = 0.059\ \Delta pH$, we can estimate a pH difference of just 0.52 unit between both electrodes. Of course, this number cannot be assigned to the actual pH at the surface, since this difference may be caused by pH and other parameters, including Pt surface states. But such small difference indicates that the higher stability and activity found in GPO electrodes cannot arise exclusively from the modification of the local pH. Therefore, we associate the protective function to the hydrophobic environment, which avoids proper solvation of the oxides, precluding its dissolution. The high hydrophobicity of GPO is corroborated by contact angle tests (Figure 3.23). A contact angle of 125° was found for a 1 M H_2SO_4 solution on GPO, significantly higher than on GC (86°).

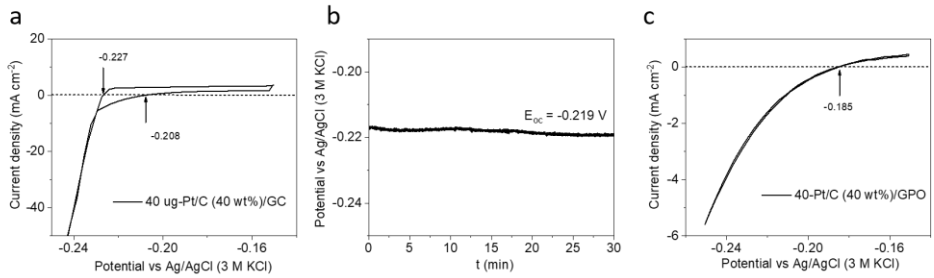

Figure 3.22. (a) Calibration of the actual value of the potential of the Ag/AgCl (3 M KCl) vs. the reversible hydrogen electrode (RHE) by using a hydrogen electrode reaction with 40 ug-Pt/C (40 wt%)/GC, the Ag/AgCl electrode as the reference electrode, and carbon rod as the counter electrode in a hydrogen-saturated 1 M H_2SO_4 electrolyte. (b) OCP value recording. (c) CV curve of 40-Pt/C (40 wt%)/GPO with 10 mV s^{-1} scan rate.

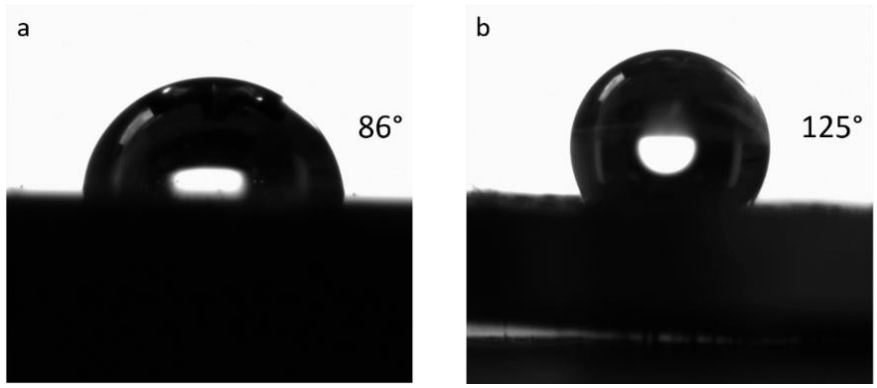

Figure 3.23. Contact angle tests of (a) glassy carbon and (b) GPO.

We also compared the activity/stability of Co_3O_4@C vs Co_3O_4 (Figure 3.9). The corresponding x-Co_3O_4/GPO electrodes showed good stability during preliminary CV cycles and chronopotentiometry measurement, but at higher overpotentials. A 5 mF cm^{-2} EDLC was determined, just 1/5 that of Co_3O_4@C/GPO (Figure 3.13). Specific surface area from N_2 sorption isotherm curves for Co_3O_4@C was also about 5 times greater than that of Co_3O_4 (Figure 3.24). These results suggest that the role of the carbon coating is to improve the nanostructuration of the active Co_3O_4 material.

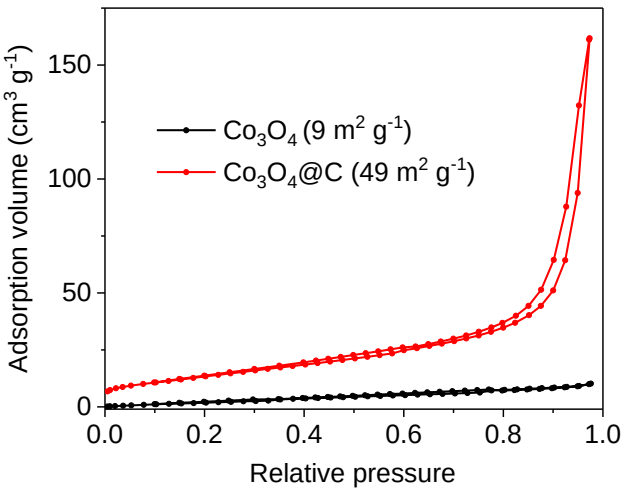

Figure 3.24. Adsorption and desorption isotherms of Co_3O_4@C and Co_3O_4.

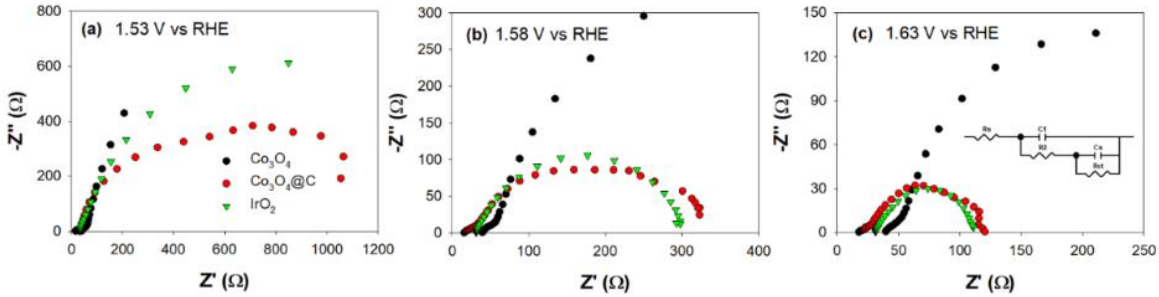

Figure 3.25. Nyquist plots from EIS data for Co_3O_4@C/GPO, Co_3O_4/GPO and IrO_2/GPO electrodes at different applied potentials (a) 1.53 V vs RHE, (b) 1.58 V vs RHE and (c) 1.63 V vs RHE. The equivalent circuit model employed to fit the data is also showed as an inset in the right panel (c).

In addition, the Co_3O_4@C/GPO, Co_3O_4/GPO and IrO_2/GPO electrodes were studied by Electrochemical Impedance Spectroscopy (EIS) at different applied potentials. Figure 3.25 shows the obtained Nyquist plots, which systematically feature two arcs (or distorted arc for IrO_2), consistent with two simultaneous/consecutive charge-transfer channels[64]. Fitting the experimental data to a suitable equivalent circuit model (Figure 3.26) revealed that the best ohmic contact (reflected by the series resistance, R_S) is obtained for the Co_3O_4@C/GPO (Figure 3.26a). On the other hand, the charge transfer resistance (R_{ct}), scales inversely with the electrocatalytic activity of the different electrodes, being the lowest one for the

Co_3O_4@C/GPO electrode (Figure 3.26b). This is consistent with the estimated surface capacitance, which scales with electrode performance, as a result of higher surface area and hence, higher density of catalytic sites (Figure 3.26c).

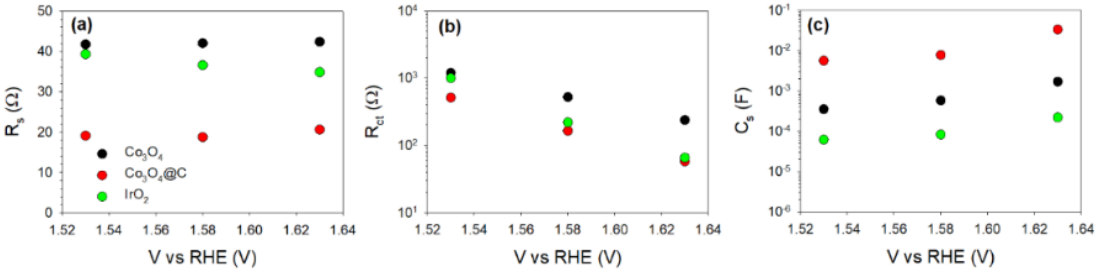

Figure 3.26. Fitted parameters from the EIS analysis: (a) Series resistance, R_s, (b) Charge transfer resistance, R_{ct} and (c) Surface capacitance, C_S.

3.3.6. Conclusions

In summary, we are reporting the activity and promising stability of carbon-decorated Co_3O_4@C nanoparticles (Co_3O_4@C) for electrocatalytic OER under acidic conditions when protected by a hydrophobic binder support. Electrodes built from Co_3O_4@C, graphite and paraffin oil are able to evolve oxygen from water during the electrolysis of a concentrated (1 M) sulfuric acid solution (pH < 0.1).

Table 3.6. Performance parameters for different electrocatalysts for OER in strong acidic electrolytes.

Catalyst	H_2SO_4 (M)	Scan rate (mV s^{-1})	η (mV)[a]	Tafel slope (mV dec^{-1})	Stability	Loading (mg cm^{-2})	*S*	Ref.
Co_3O_4@C/GPO	1	1	356	139	43 h[a]	20	25	this work
[Co-POM]/CP	1	1	361	97	24 h @ η = 250 mV	20	~	65
IrO_2	1	1	458	66	24 h @ η = 250 mV	26	~	65
ATO/CoHFe	0.1	50	770	~	~	0.61	~	24
IrO_2/$SrIrO_3$	0.5	10	280	~	30 h[a]	~	~	20
$CoFePbO_x$	1	~	620	~	12 h @ 2.03 V	~	~	29

MnO_2	0.1	1	428	80	8000 h[a]	36	~855	25
$Ni_{0.5}Mn_{0.5}Sb_{1.7}O_x$	1	10	672	60	168 h[a]	~0.18	~6194	26
$Co_{0.05}Fe_{0.95}O_y$	0.5	10	650	110	50 h[a]	1	~	27
$Mn_xSb_{1-x}O_z$	1	20	508	75	2 h[a]	~	71	28
Co_3O_4/FTO	0.5	2	490	80	12 h[a]	~	~847	31
$W_{0.57}Ir_{0.43}O_{3-\delta}$	1	20	370	125	2000 s[a]	~	~	66
Ti-MnO_2	0.05	5	~540[b]	170	2 h @ 1.9 V	~	~16230	67
$Ni_{40}Fe_{40}P_{20}$	0.05	5	540	-	30 h[a]	~	~	68
c-Fe_2O_3	0.5	10	650	56	24 h[a]	1	~174	69
P-NSC/ $Ni_4Fe_5S_8$-1000	0.5	2	~560	72	10000 cycles[c]	0.4	~	52
$Y_{1.85}Zn_{0.15}Ru_2O_{7-\delta}$	0.5	10	291	37	2000 cycles @ 1.55 V	3	~	70
1T-MoS_2	0.5	5	420	322	2 h[a]	1	~	71
Ir-ND/ATO	0.05	5	~400	56	15 h[a]	0.01	~	48
Ir/TiO_x	0.5	6	~320	53	~	~	~	72
IrO_x/ATO	0.05	5	~420	60	15 h[c]	0.01	12307	49

[a] @10 mA cm^{-2}. [b] @2 mA cm^{-2}. [c] @ 1 mA cm^{-2}

Although previous reports on acidic water splitting with earth-abundant raw materials had achieved either high activity or high stability, this is the first consistent report of a working anode fulfilling both requirements (Table 3.6). These electrodes operate during more than 40 h, at a relatively high current density (10 mA cm^{-2}) and at a low overpotential of $\eta < 398$ mV, very close to the benchmarking performance of state-of-the-art IrO_2.

The synergy between active catalytic phase, Co_3O_4 nanoparticles, and the carbon support (doped-carbon cover, graphite and paraffin oil) is crucial to reach this robust performance. We assign this protective effect to the hydrophobicity of the electrode surface, which could avoid proper solvation of the metal oxides precluding their dissolutions.

Despite the promising performance of our electrodes, a few challenges will need to be addressed before their implementation into commercial electrolyzers. To start with, the carbon content may become an issue at high current densities, as those expected from commercial devices (> 500 mA cm^{-2}). But our successful corrosion-protection opens an interesting strategy that can be translated into full cell devices, looking for alternative approaches to incorporate hydrophobic species at the electrode surfaces.

3.4. References

1. Wei, C. *et al.* Recommended Practices and Benchmark Activity for Hydrogen and Oxygen Electrocatalysis in Water Splitting and Fuel Cells. *Adv. Mater.* **31,** 1–24 (2019).
2. Staffell, I. *et al.* The role of hydrogen and fuel cells in the global energy system. *Energy Environ. Sci.* **12,** 463–491 (2019).
3. Singh, S. *et al.* Hydrogen: A sustainable fuel for future of the transport sector. *Renew. Sustain. Energy Rev.* **51,** 623–633 (2015).
4. Sharma, S. & Ghoshal, S. K. Hydrogen the future transportation fuel: From production to applications. *Renew. Sustain. Energy Rev.* **43,** 1151–1158 (2015).
5. Seh, Z. W. *et al.* Combining theory and experiment in electrocatalysis: Insights into materials design. *Science* **355,** 1–12 (2017).
6. McCrory, C. C. L. *et al.* Benchmarking Hydrogen Evolving Reaction and Oxygen Evolving Reaction Electrocatalysts for Solar Water Splitting Devices. *J. Am. Chem. Soc.* **137,** 4347–4357 (2015).
7. Zhu, J., Hu, L., Zhao, P., Lee, L. Y. S. & Wong, K. Y. Recent Advances in Electrocatalytic Hydrogen Evolution Using Nanoparticles. *Chem. Rev.* **120,** 851–918 (2020).
8. Lyu, F., Wang, Q., Choi, S. M. & Yin, Y. Noble-Metal-Free Electrocatalysts for Oxygen Evolution. *Small* **15,** 1–17 (2019).
9. Spöri, C., Kwan, J. T. H., Bonakdarpour, A., Wilkinson, D. P. & Strasser, P. The Stability Challenges of Oxygen Evolving Catalysts: Towards a Common Fundamental Understanding and Mitigation of Catalyst Degradation. *Angew. Chemie - Int. Ed.* **56,** 5994–6021 (2017).
10. Han, B. *et al.* Screening Oxide Support Materials for OER Catalysts in Acid. *J. Electrochem. Soc.* **165,** 813–820 (2018).
11. Chung, D. Y. *et al.* Large-Scale Synthesis of Carbon-Shell-Coated FeP Nanoparticles for Robust Hydrogen Evolution Reaction Electrocatalyst. *J. Am. Chem. Soc.* **139,** 6669–6674 (2017).
12. Schipper, D. E. *et al.* Effects of Catalyst Phase on the Hydrogen Evolution Reaction of Water Splitting: Preparation of Phase-Pure Films of FeP, Fe_2P, and Fe_3P and Their Relative Catalytic Activities. *Chem. Mater.* **30,** 3588–3598 (2018).

13. Sun, J. *et al.* Robust Hydrogen-Evolving Electrocatalyst from Heterogeneous Molybdenum Disulfide-Based Catalyst. *ACS Catal.* **10,** 1511–1519 (2020).
14. Yu, J., Cheng, G. & Luo, W. Ternary nickel-iron sulfide microflowers as a robust electrocatalyst for bifunctional water splitting. *J. Mater. Chem. A* **5,** 15838–15844 (2017).
15. Kuo, D. Y. *et al.* Influence of Surface Adsorption on the Oxygen Evolution Reaction on IrO_2 (110). *J. Am. Chem. Soc.* **139,** 3473–3479 (2017).
16. Cherevko, S. *et al.* Oxygen and hydrogen evolution reactions on Ru, RuO_2, Ir, and IrO_2 thin film electrodes in acidic and alkaline electrolytes: A comparative study on activity and stability. *Catal. Today* **262,** 170–180 (2016).
17. Chen, S. *et al.* Mn-Doped RuO_2 Nanocrystals as Highly Active Electrocatalysts for Enhanced Oxygen Evolution in Acidic Media. *ACS Catal.* **10,** 1152–1160 (2020).
18. Shan, J., Zheng, Y., Shi, B., Davey, K. & Qiao, S. Z. Regulating electrocatalysts via surface and interface engineering for acidic water electrooxidation. *ACS Energy Lett.* **4,** 2719–2730 (2019).
19. Escudero-Escribano, M. *et al.* Importance of Surface IrOx in Stabilizing RuO_2 for Oxygen Evolution. *J. Phys. Chem. B* **122,** 947–955 (2018).
20. Seitz, L. C. *et al.* A highly active and stable $IrO_x/SrIrO_3$ catalyst for the Oxygen evolution reaction. *Science* **353,** 1011–1014 (2016).
21. Ouattara, L., Fierro, S., Frey, O., Koudelka, M. & Comninellis, C. Electrochemical comparison of IrO_2 prepared by anodic oxidation of pure iridium and IrO_2 prepared by thermal decomposition of H_2IrCl_6 precursor solution. *J. Appl. Electrochem.* **39,** 1361–1367 (2009).
22. Lyons, M. E. G. & Floquet, S. Mechanism of oxygen reactions at porous oxide electrodes. Part 2 - Oxygen evolution at RuO_2, IrO_2 and $Ir_xRu_{1-x}O_2$ electrodes in aqueous acid and alkaline solution. *Phys. Chem. Chem. Phys.* **13,** 5314–5335 (2011).
23. Stoerzinger, K. A. *et al.* Orientation-Dependent Oxygen Evolution on RuO_2 without Lattice Exchange. *ACS Energy Lett.* **2,** 876–881 (2017).
24. Rodríguez-García, B. *et al.* Cobalt hexacyanoferrate supported on Sb-doped SnO_2 as a non-noble catalyst for oxygen evolution in acidic medium. *Sustain. Energy Fuels* **2,** 589–597 (2018).

25. Li, A. *et al.* Stable Potential Windows for Long-Term Electrocatalysis by Manganese Oxides Under Acidic Conditions. *Angew. Chem. Int. Ed.* **58,** 5054–5058 (2019).
26. Moreno-Hernandez, I. A. *et al.* Crystalline nickel manganese antimonate as a stable water-oxidation catalyst in aqueous 1.0 M H_2SO_4. *Energy Environ. Sci.* **10,** 2103–2108 (2017).
27. Kwong, W. L., Lee, C. C., Shchukarev, A. & Messinger, J. Cobalt-doped hematite thin films for electrocatalytic water oxidation in highly acidic media. *Chem. Commun.* **55,** 5017–5020 (2019).
28. Zhou, L. *et al.* Rutile Alloys in the Mn–Sb–O System Stabilize Mn^{3+} to Enable Oxygen Evolution in Strong Acid. *ACS Catal.* **8,** 10938–10948 (2018).
29. Chatti, M. *et al.* Intrinsically stable in situ generated electrocatalyst for long-term oxidation of acidic water at up to 80 °C. *Nat. Catal.* **2,** 457–465 (2019).
30. Bloor, L. G., Molina, P. I., Symes, M. D. & Cronin, L. Low pH electrolytic water splitting using earth-abundant metastable catalysts that self-assemble in situ. *J. Am. Chem. Soc.* **136,** 3304–3311 (2014).
31. Mondschein, J. S. *et al.* Crystalline Cobalt Oxide Films for Sustained Electrocatalytic Oxygen Evolution under Strongly Acidic Conditions. *Chem. Mater.* **29,** 950–957 (2017).
32. Etzi Coller Pascuzzi, M., van Velzen, M., Hofmann, J. P. & Hensen, E. J. M. On the Stability of Co_3O_4 Oxygen Evolution Electrocatalysts in Acid. *ChemCatChem* **13,** 459–467 (2021).
33. Yang, X. *et al.* Highly acid-durable carbon coated Co_3O_4 nanoarrays as efficient oxygen evolution electrocatalysts. *Nano Energy* **25,** 42–50 (2016).
34. Yan, K. L. *et al.* Probing the active sites of Co_3O_4 for the acidic oxygen evolution reaction by modulating the Co^{2+}/Co^{3+} ratio. *J. Mater. Chem. A* **6,** 5678–5686 (2018).
35. A Li *et al.* Enhancing the stability of cobalt spinel oxide towards sustainable oxygen evolution in acid. *Nat. Catal.* **5**, 109–118 (2022).
36. Arens, J. T. *et al.* Water oxidation electrocatalysis in acidic media with Co-containing polyoxometalates. *J. Catal.* **389,** 345–351 (2020).

37. Yang, F., Chen, Y., Cheng, G., Chen, S. & Luo, W. Ultrathin Nitrogen-Doped Carbon Coated with CoP for Efficient Hydrogen Evolution. *ACS Catal.* **7,** 3824–3831 (2017).
38. Yang, F. *et al.* Design of active and stable oxygen reduction reaction catalysts by embedding Co_xO_y nanoparticles into nitrogen-doped carbon. *Nano Res.* **10,** 97–107 (2017).
39. Petzoldt, P. J., Kwan, J. T. H., Bonakdarpour, A. & Wilkinson, D. P. Deconvoluting Reversible and Irreversible Degradation Phenomena in OER Catalyst Coated Membranes Using a Modified RDE Technique. *J. Electrochem. Soc*. **168**, 026507 (2021).
40. Morales, D. M. & Risch, M. Seven steps to reliable cyclic voltammetry measurements for the determination of double layer capacitance. *J. Phys. Energy* **3,** 34013 (2021).
41. Shirley, D. A. High-resolution X-ray photoemission spectrum of the valence bands of gold. *Phys. Rev. B* **5**, 4709–4714 (1972).
42. Biesinger, M. C. *et al.* Resolving surface chemical states in XPS analysis of first row transition metals, oxides and hydroxides: Cr, Mn, Fe, Co and Ni. *Appl. Surf. Sci.* **257,** 2717–2730 (2011).
43. Park, K. S. *et al.* Exceptional chemical and thermal stability of zeolitic imidazolate frameworks. *Proc. Natl. Acad. Sci. U. S. A.* **103,** 10186–10191 (2006).
44. Anantharaj, S. *et al.* Recent Trends and Perspectives in Electrochemical Water Splitting with an Emphasis on Sulfide, Selenide, and Phosphide Catalysts of Fe, Co, and Ni: A Review. *ACS Catal.* **6,** 8069–8097 (2016).
45. Reier, T., Oezaslan, M. & Strasser, P. Electrocatalytic oxygen evolution reaction (OER) on Ru, Ir, and pt catalysts: A comparative study of nanoparticles and bulk materials. *ACS Catal.* **2,** 1765–1772 (2012).
46. Li, D., Shi, J. & Li, C. Transition-Metal-Based Electrocatalysts as Cocatalysts for Photoelectrochemical Water Splitting: A Mini Review. *Small* **14,** 1–22 (2018).
47. Tamirat, A. G., Rick, J., Dubale, A. A., Su, W. N. & Hwang, B. J. Using hematite for photoelectrochemical water splitting: A review of current progress and challenges. *Nanoscale Horizons* **1,** 243–267 (2016).
48. Oh, H. S., Nong, H. N., Reier, T., Gliech, M. & Strasser, P. Oxide-supported Ir nanodendrites with high activity and durability for the oxygen

evolution reaction in acid PEM water electrolyzers. *Chem. Sci*. **6**, 3321–3328 (2015).

49. Oh, H. S. et al. Electrochemical Catalyst-Support Effects and Their Stabilizing Role for IrO_x Nanoparticle Catalysts during the Oxygen Evolution Reaction. *J. Am. Chem. Soc*. **138**, 12552–12563 (2016).
50. Reier, T., Nong, H. N., Teschner, D., Schlögl, R. & Strasser, P. Electrocatalytic Oxygen Evolution Reaction in Acidic Environments – Reaction Mechanisms and Catalysts. *Adv. Energy Mater.* **7,** 1601275 (2017).
51. Ashton, S. J. & Arenz, M. A DEMS study on the electrochemical oxidation of a high surface area carbon black. *Electrochem. commun.* **13,** 1473–1475 (2011).
52. Hu, Q. *et al.* Coupling pentlandite nanoparticles and dual-doped carbon networks to yield efficient and stable electrocatalysts for acid water oxidation. *J. Mater. Chem. A* **7,** 461–468 (2019).
53. Cheng, W. *et al.* A metal-vacancy-solid-solution NiAlP nanowall array bifunctional electrocatalyst for exceptional all-pH overall water splitting. *J. Mater. Chem. A* **6,** 9420–9427 (2018).
54. Mondschein, J. S. *et al.* Intermetallic Ni_2Ta Electrocatalyst for the Oxygen Evolution Reaction in Highly Acidic Electrolytes. *Inorg. Chem.* **57,** 6010–6015 (2018).
55. McCrory, C. C. L., Jung, S., Peters, J. C. & Jaramillo, T. F. Benchmarking heterogeneous electrocatalysts for the oxygen evolution reaction. *J. Am. Chem. Soc.* **135,** 16977–16987 (2013).
56. Geiger, S. *et al.* The stability number as a metric for electrocatalyst stability benchmarking. *Nat. Catal.* **1,** 508–515 (2018).
57. Kim, Y. T. *et al.* Balancing activity, stability and conductivity of nanoporous core-shell iridium/iridium oxide oxygen evolution catalysts. *Nat. Commun.* **8,** 1–8 (2017).
58. An, L. *et al.* Recent Development of Oxygen Evolution Electrocatalysts in Acidic Environment. *Adv. Mater.* **33,** 1–31 (2021).
59. Díaz-Fernández, D. *et al.*, The growth of cobalt oxides on HOPG and SiO_2 surfaces: A comparative study. *Surface Science* **624,** 145–153 (2014).
60. Wang, J., Musameh, M. & Mo, J. W. Acid stability of carbon paste enzyme electrodes. *Anal. Chem.* **78,** 7044–7047 (2006).

61. Fang, Z. *et al.* Hybrid Organic-Inorganic Gel Electrocatalyst for Stable Acidic Water Oxidation. *ACS Nano* **13,** 14368–14376 (2019).
62. Sempionatto, J. R. *et al.* Enzymatic biofuel cells based on protective hydrophobic carbon paste electrodes: Towards epidermal bioenergy harvesting in the acidic sweat environment. *Chem. Commun.* **56,** 2004–2007 (2020).
63. Liang, Y. *et al.* Co_3O_4 nanocrystals on graphene as a synergistic catalyst for oxygen reduction reaction. *Nat. Mater.* **10,** 780–786 (2011).
64. Han, L. *et al.* Cobalt Hexacyanoferrate as a Selective and High Current Density Formate Oxidation Electrocatalyst. *ACS Appl. Energy Mater.* **3,** 9198–9207 (2020).
65. Blasco-Ahicart, M., Soriano-Lopez, J., Carbo, J. J., Poblet, J. M. & Galan-Mascaros, J. R. Polyoxometalate electrocatalysts based on earthabundant metals for efficient water oxidation in acidic media. *Nat. Chem.* **10,** 24–30 (2018).
66. Kumari, S. *et al.* A low-noble-metal W1-xIrxO3-δ water oxidation electrocatalyst for acidic media via rapid plasma synthesis. *Energy Environ. Sci.* **10,** 2432–2440 (2017).
67. Frydendal, R., Paoli, E. A., Chorkendorff, I., Rossmeisl, J. & Stephens, I. E. L. Toward an Active and Stable Catalyst for Oxygen Evolution in Acidic Media: Ti-Stabilized MnO2. *Adv. Energy Mater.* **5,** (2015).
68. Hu, F. *et al.* Amorphous Metallic NiFeP: A Conductive Bulk Material Achieving High Activity for Oxygen Evolution Reaction in Both Alkaline and Acidic Media. *Adv. Mater.* **29,** 1–9 (2017).
69. Kwong, W. L., Lee, C. C., Shchukarev, A., Björn, E. & Messinger, J. High-performance iron (III) oxide electrocatalyst for water oxidation in strongly acidic media. *J. Catal.* **365,** 29–35 (2018).
70. Feng, Q. *et al.* Highly active and stable ruthenate pyrochlore for enhanced oxygen evolution reaction in acidic medium electrolysis. *Appl. Catal. B Environ.* **244,** 494–501 (2019).
71. Wu, J. *et al.* Exfoliated 2D Transition Metal Disulfides for Enhanced Electrocatalysis of Oxygen Evolution Reaction in Acidic Medium. *Adv. Mater. Interfaces* **3,** 1–6 (2016).

72. Bernicke, M. *et al.* Tailored mesoporous Ir/TiO_x: Identification of structure-activity relationships for an efficient oxygen evolution reaction. *J. Catal.* **376,** 209–218 (2019).

Chapter 4. A survey of earth abundant metal oxides as oxygen evolution electrocatalysts in acidic media (pH <1)

4.1. Introduction

Electrolytic water splitting to obtain hydrogen is in high demand to support the deployment of renewable energy as energy storage media, in the required transition from fossil fuels[1,2]. One of the challenges in water electrolysis remains the catalysis of the anodic oxygen evolution reaction (OER). This 4-electron process is partially responsible for the slow kinetics and high overpotentials[3]. Competitive catalysts from earth abundant materials are required for the development and deployment of water electrolysers.

Numerous earth-abundant materials are able to work as OER electrocatalysts in neutral and alkaline media, reaching excellent performance in nickel-iron mixed oxides or (oxo) hydroxides[4-7]. But alkaline technologies have several disadvantages, such as the need for corrosive media (>30% hot KOH), and the low current densities achieved limited by the OH^- transport through the separator. Only noble metal-based catalysts (RuO_2 and IrO_2) are efficient, and stable in acidic conditions, where much higher current densities can be achieved thanks to the ultrafast proton transport through a solid electrolyte (proton exchange membrane). Furthermore, the high proton concentration speeds up hydrogen generation (HER)[8]. At low pH, inexpensive metal oxides suffer serious deactivation, particularly when working under high potentials/current densities[9-11].

Several strategies have been proposed to stabilize earth abundant metal oxides as OER electrocatalysts in acidic media[12-17]. Crystalline nickel manganese antimonate on on antimony tin oxide (ATO) becomes stable under current densities of 10 mA cm^{-2} for 168 h in 1 M H_2SO_4, finely tuning the metals ratio[12]. Co_2MnO_4 demonstrated robust performance (1500 h) at 200 mA cm^{-2} in pH 1 when supported on Pt/Ti mesh[14]. Although high overpotentials were needed, these reports are promising results towards earth abundant OER catalysis in acidic conditions.

Recently, we demonstrated that the use of a partially hydrophobic binder in the anode composition is able to stabilize Co_3O_4, otherwise unstable in these conditions[18,19]. A Co_3O_4@C/(graphitic carbon + paraffin oil, GPO) composite sustained a current density up to 100 mA cm^{-2} in 1 M H_2SO_4 electrolyte. Even when this electrode architecture cannot be scaled up to industrial applications, given the long-term instability of carbon conducting supports under OER, we confirmed with preliminary tests its general validity to stabilize a wide range of OER catalysts. Taking this advantage, here we report a wide screening of first row transition metal (Mn, Fe, Co, Ni and Zn) oxides as OER catalysts in 1 M H_2SO_4. We have investigated monometallic, binary and ternary compositions of equimolecular compositions. Surprisingly, we found that even Mn-based oxides may be stabilized, when these were characterized as highly unstable[20,21]. Indeed, Mn_2O_3 anodes showed the best performance in terms of overpotential to reach 10 mA cm^{-2}, with excellent stability (> 24 h) when working in 1 M sulfuric acid solution without a sign of fatigue or deactivation. The incorporation of a second or third metal did not improve the activity of the Mn-based oxide. Conversely, the Mn doping was critical to improve some oxides' OER activity, such as FeO_x, NiO_x and $FeNiO_x$, with at most 120 mV overpotential decrease under 10 mA cm^{-2} current density.

4.2. Experimental sections

4.2.1. Synthesis

All reagents were commercially available and used as received. Mixed metal oxides were prepared by modified method available in the literature[22]. The overall metal concentration of metal (Mn, Fe, Co, Ni and Zn) nitrates was fixed as 0.0125 M, and the corresponding amount of each metallic precursor was calculated in the equivalent ratio. They were dissolved in 50 mL distilled water with constant stirring. Then, glycine was added into above solutions (glycine/metal molar ratio was 1.2), and stirred until clear solutions were obtained. Afterwards, the solutions were heated up to 210 °C until total solvent evaporation and glycine combustion. The resulting porous dark solids were collected and calcined at 1100 °C in a tubular oven for 1 h. To obtain Mn_2O_3, the temperature was decreased to 600 °C. In the synthesis of Mn_3O_4, $Mn(NO_3)_2{\cdot}4H_2O$ (0.151 g) and benzimidazole (0.142 g) were

dissolved into 15 mL DMF and then the homogeneous solution was transferred into a Teflon-lined stainless autoclave. The sealed autoclave was put into an oven and kept at 140 °C for 24 h. After cooling down to room temperature, the brown product was filtered out and washed with acetone, and then dried at 60 °C.

The composite electrodes were prepared by 2-hour ball-milling at 20 s^{-1} of a mixture of paraffin oil (20 mg), graphite powder (80 mg) and oxides (40 mg), namely, MO_x/GPO, $MM'O_x$/GPO or $MM'M''O_x$/GPO (M, M', M'': Mn, Fe, Co, Ni, Zn). When the added amount of Mn_2O_3 was decreased to 10 and 20 mg, these electrodes were named as 10-Mn_2O_3/GPO and 20-Mn_2O_3/GPO, respectively.

4.2.2. Electrochemistry

All electrochemical experiments were performed under ambient conditions using a Bio-Logic VMP3 multichannel potentiostat and implemented with a three-electrode configuration using 1 M H_2SO_4 (pH 0.1) as filling solution, carbon rod as counter electrode, Ag/AgCl (3 M KCl) as reference electrode and a pocket working electrode (0.07 cm^2 surface area and 4 mm depth) filled with the GPO composites. The actual mass amounts of the MO_x/GPO, $MM'O_x$/GPO and $MM'M''O_x$/GPO composites in the electrode pocket were measured with an analytical weight balance and indicated in Table S1. All potentials were measured versus Ag/AgCl electrode and converted to the RHE reference scale using $E_{RHE} = E_{Ag/AgCl} + 0.21 + 0.059$ pH (V) while overpotentials $\eta = E_{RHE} - 1.23$ V. Every LSV (linear sweep voltammetry) curve was recorded with a 1 mV s^{-1} scan rate for activity comparison after 10-CV (cyclic voltammetry) cycle activation. All current densities were calculated based on the geometrical surface area of the electrodes. Ohmic drop was determined for all electrochemical data by using the automatic current interrupt (CI) software (Table 4.1). The iR drop, experimentally determined by CI technique, was corrected for all electrodes. Tafel slopes were estimated from the LSV curves by plotting overpotential η vs log *j* (*j* = current density). The potential vs RHE to drive 1 mA cm^{-2} was used to define onset potential. Chronopotentiometry tests were carried out at fixed current density of 10 mA cm^{-2}. For the electrochemical double-layer capacitance (EDLC) measurements, open circuit potentials (OCPs) vs. the Ag/AgCl were

firstly recorded for 30 mins to reach rather stable values. Then CV experiments were carried out with 10 mV s^{-1} scan rate. Combined with above CV measurements, the 100 mV potential windows centered at OCPs could be determined and cyclic voltammetry were then carried out under scanning rates of 20, 40, 60, 80 and 100 mV s^{-1}. The current density differences between the minimum and maximum values at OCPs vs. the Ag/AgCl and the corresponding scanning rates were plotted to calculate the EDLC value (1/2 of the slope of current density-scan rate plots)[23].

Table 4.1. The metal salt precursors of syntheses, corresponding XRD phases, Ohmic drop values determined by the automatic current interrupt (CI) software and actual mass of catalysts in working electrodes of different oxides.

Oxide	Precursor (mole ratio)	XRD phase	Ohmic drop (Ω)	Total composite mass in the electrode (mg)
MnO_x	$Mn(NO_3)_2{\cdot}4H_2O$	Mn_2O_3, Mn_3O_4	11	41
Mn_2O_3	-	Mn_2O_3	16	38
Mn_3O_4	-	Mn_3O_4	11	41
FeO_x	$Fe(NO_3)_3{\cdot}9H_2O$	Fe_2O_3	16	39
CoO_x	$Co(NO_3)_2{\cdot}6H_2O$	Co_3O_4	18	42
NiO_x	$Ni(NO_3)_2{\cdot}6H_2O$	NiO	15	47
ZnO_x	$Zn(NO_3)_2{\cdot}6H_2O$	ZnO	16	42
$MnFeO_x$	$Mn(NO_3)_2{\cdot}4H_2O$/ $Fe(NO_3)_3{\cdot}9H_2O$ (1:1)	$(Mn_{0.983}Fe_{0.017})_2O_3$	10	41
$MnCoO_x$	$Mn(NO_3)_2{\cdot}4H_2O$/$Co(NO_3)_2{\cdot}6H_2O$ (1:1)	$(Co, Mn)_3O_4$	22	44
$MnNiO_x$	$Mn(NO_3)_2{\cdot}4H_2O$/ $Ni(NO_3)_2{\cdot}6H_2O$ (1:1)	Ni_6MnO_8	9	44
$MnZnO_x$	$Mn(NO_3)_2{\cdot}4H_2O$/ $Zn(NO_3)_2{\cdot}6H_2O$ (1:1)	$ZnMnO_3$, $ZnMn_3O_4$	11	41
$FeCoO_x$	$Fe(NO_3)_3{\cdot}9H_2O$/$Co(NO_3)_2{\cdot}6H_2O$ (1:1)	Fe_2O_3	13	45
$FeNiO_x$	$Fe(NO_3)_3{\cdot}9H_2O$/$Ni(NO_3)_2{\cdot}6H_2O$ (1:1)	$NiFe_2O_4$	19	43
$FeZnO_x$	$Fe(NO_3)_3{\cdot}9H_2O$/$Zn(NO_3)_2{\cdot}6H_2O$ (1:1)	$ZnFe_2O_4$	21	43
$CoNiO_x$	$Co(NO_3)_2{\cdot}6H_2O$ / $Ni(NO_3)_2{\cdot}6H_2O$ (1:1)	CoO/NiO	14	44
$CoZnO_x$	$Co(NO_3)_2{\cdot}6H_2O$ / $Zn(NO_3)_2{\cdot}6H_2O$ (1:1)	$ZnCo_2O_4$, ZnO	10	41
$NiZnO_x$	$Ni(NO_3)_2{\cdot}6H_2O$ / $Zn(NO_3)_2{\cdot}6H_2O$ (1:1)	NiO, ZnO	9	45
$MnFeCoO_x$	$Mn(NO_3)_3{\cdot}4H_2O$/$Fe(NO_3)_3{\cdot}9H_2O$/$Co(NO_3)_2{\cdot}6H_2O$ (1:1:1)	$CoFe_2O_4$	18	38

$MnFeNiO_x$	$Mn(NO_3)_3{\cdot}4H_2O/Fe(NO_3)_3{\cdot}9H_2O/Ni(NO_3)_2{\cdot}6H_2O$ (1:1:1)	$NiFe_2O_4$, $MnNi_2O_4$	9	40
$MnFeZnO_x$	$Mn(NO_3)_3{\cdot}4H_2O/Fe(NO_3)_3{\cdot}9H_2O/Zn(NO_3)_2{\cdot}6H_2O$ (1:1:1)	$ZnMn_3O_4$, $Fe_{0.85-x}Zn_xO$, $MnFe_2O_4$	11	40
$MnCoNiO_x$	$Mn(NO_3)_3{\cdot}4H_2O/Co(NO_3)_2{\cdot}6H_2O/Ni(NO_3)_2{\cdot}6H_2O$ (1:1:1)	NiO, Ni_6MnO_8	15	39
$MnCoZnO_x$	$Mn(NO_3)_3{\cdot}4H_2O/Co(NO_3)_2{\cdot}6H_2O/Zn(NO_3)_2{\cdot}6H_2O$ (1:1:1)	$MnCo_2O_4$	10	42
$MnNiZnO_x$	$Mn(NO_3)_3{\cdot}4H_2O/Ni(NO_3)_2{\cdot}6H_2O/Zn(NO_3)_2{\cdot}6H_2O$ (1:1:1)	Ni_6MnO_8, NiO	8	44
$FeCoNiO_x$	$Fe(NO_3)_3{\cdot}9H_2O/Co(NO_3)_2{\cdot}6H_2O/Ni(NO_3)_2{\cdot}6H_2O$ (1:1:1)	$NiFe_2O_4$+$CoFe_2O_4$+$NiCo_2O_4$	23	44
$FeCoZnO_x$	$Fe(NO_3)_3{\cdot}9H_2O/Co(NO_3)_2{\cdot}6H_2O/Zn(NO_3)_2{\cdot}6H_2O$ (1:1:1)	Fe_2O_3, ZnO	26	41
$FeNiZnO_x$	$Fe(NO_3)_3{\cdot}9H_2O/Ni(NO_3)_2{\cdot}6H_2O/Zn(NO_3)_2{\cdot}6H_2O$ (1:1:1)	Fe_3O_4, ZnO	8	45
$CoNiZnO_x$	$Co(NO_3)_2{\cdot}6H_2O/Ni(NO_3)_2{\cdot}6H_2O/Zn(NO_3)_2{\cdot}6H_2O$ (1:1:1)	$CoNiO_2$, $ZnCo_2O_4$, ZnO	9	44

4.2.3. Faradaic efficiency

In order to evaluate the faradaic efficiency towards oxygen production, the chronopotentiometric experiment was carried out applying a fixed current while oxygen concentration in the headspace was in-situ measured by using an Ocean Optics NeoFOX sensing system equipped with an FOSPOR probe. The FOSPOR probe was calibrated with a two-point calibration, fixing 0% O_2 under N_2 flow and 20.9% O_2 in air. The experiment was performed in a personalized H-type cell with a frit glass separating both compartments and a connection for the sensor to be inserted in the anodic gas headspace (~2.5 mL) (Figure 4.1). The solution was completely deaerated by purging with N_2 before starting the experiment, for at least 1 h. Then N_2 flow was removed and a base line of 10 min was recorded before starting the chronoamperometry.

The mols of O_2 generated during the electrochemical experiment were calculated with the following equation, considering ideal gas behaviour:

$$\boldsymbol{n_{O_2,exp} = \%O_2 \cdot P_{total} \cdot V_{gas\ space} \cdot R^{-1} T^{-1}/100}$$

where $\%O_2$ is given by the FOSPOR probe, P_{total} is 1 atm, $V_{gas\ space}$ (litres) is measured for each experiment, R is 0.082 (atm l/K mol) and T is 293 K. The faradaic oxygen production curve was calculated taking into account the charge data from the chronoamperometry experiment as described in the following equation:

$$\boldsymbol{n_{O_2,far} = Q\, n_e^{-1}\, F^{-1}}$$

Where where Q (C) is the charge passed through the system, n_e is the number of mols of electrons involved in the water oxidation reaction to generate one mol of oxygen (4) and F is the Faraday constant (96485 C mol^{-1}).

Then Faradaic efficiency (in %), *FE*, is calculated as follows:

$$\boldsymbol{FE = \frac{100 \times n_{O_2,exp}}{n_{O_2,far}}}$$

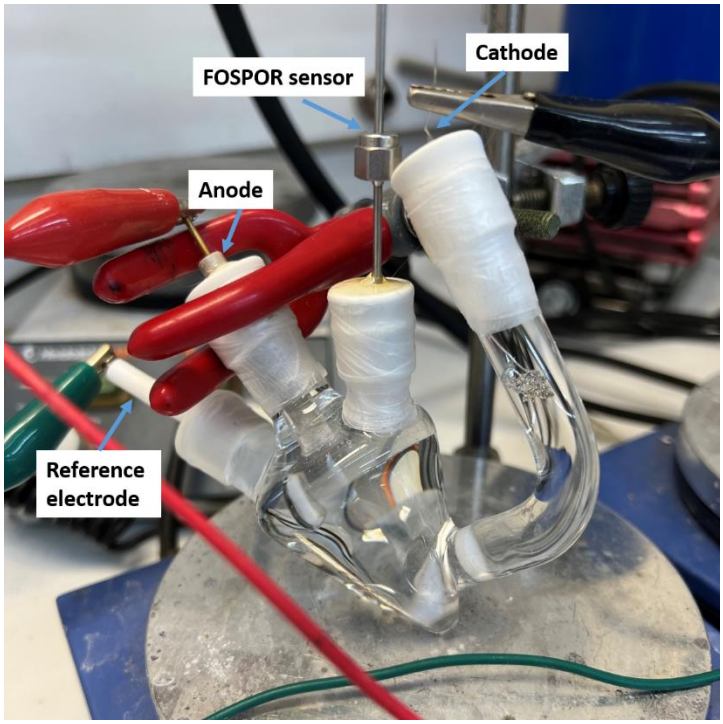

Figure 4.1. Setup for oxygen evolution measurement. It includes a personalized H-type cell containing the Mn_2O_3/GPO anode, Pt cathode and Ag/AgCl (3 M KCl) reference electrode connected to the potentiostat, the FOSPOR sensor connected to the anodic side headspace.

4.2.4. Physical characterization

Powder X-ray diffraction (PXRD) data were recorded with a Bruker D8 Advance Series equipped with a VANTEC-1 PSD3 detector. Elemental analyses were carried out with an Agilent (ICPMS7900) inductively coupled plasma spectrometer with mass detector (ICP-MS) at University of Valencia. X-ray photoelectron spectroscopy (XPS) has been carried out holding the sample at room temperature and illuminating it with monochromatized Al Kα light (hv = 1486.6 eV) from a microfocus setup (SPECS Focus 600). The excited photoelectrons were collected by a SPECS 150 hemispherical analyzer at emission and incidence angles of 40° and 60°, respectively. The powder electrodes were deposited on top of indium tape for the XPS measurements High resolution transmission electron microscopy (HRTEM) and scanning transmission electron microscopy (STEM) investigations were performed on a field emission gun FEI Tecnai F20 microscope. High angle

annular dark-field (HAADF) STEM was combined with electron energy loss spectroscopy (EELS) in the Tecnai microscopy by using a GATAN QUANTUM energy filter in order to obtain compositional maps.

4.3. Result and discussion

4.3.1. Metal oxide preparation

Table 4.2. The feeding metal ratio in syntheses and crystalline phases found by X-ray diffraction analysis.

Catalyst	Reagents metal ratio (%)					Phases found
	Mn	Fe	Co	Ni	Zn	
MnO_x	100	–	–	–	–	Mn_2O_3, Mn_3O_4
FeO_x	–	100	–	–	–	Fe_2O_3
CoO_x	–	–	100	–	–	Co_3O_4
NiO_x	–	–	–	100	–	NiO
ZnO_x	–	–	–	–	100	ZnO
$MnFeO_x$	50	50	–	–	–	$(Mn_{0.983}Fe_{0.017})_2O_3$
$MnCoO_x$	50	–	50	–	–	$(Co,Mn)_3O_4$
$MnNiO_x$	50	–	–	50	–	Ni_6MnO_8
$MnZnO_x$	50	–	–	–	50	$ZnMnO_3$, $ZnMn_3O_4$
$FeCoO_x$	–	50	50	–	–	Fe_2O_3
$FeNiO_x$	–	50	–	50	–	$NiFe_2O_4$
$FeZnO_x$	–	50	–	–	50	$ZnFe_2O_4$
$CoNiO_x$	–	–	50	50	–	CoO/NiO
$CoZnO_x$	–	–	50	–	50	$ZnCo_2O_4$, ZnO
$NiZnO_x$	–	–	–	50	50	NiO, ZnO
$MnFeCoO_x$	33	33	33	–	–	$CoFe_2O_4$
$MnFeNiO_x$	33	33	–	33	–	$NiFe_2O_4$, $MnNi_2O_4$
$MnFeZnO_x$	33	33	–	–	33	$ZnMn_3O_4$, $Fe_{0.85-x}Zn_xO$, $MnFe_2O_4$
$MnCoNiO_x$						Ni_6MnO_8, NiO
$MnCoZnO_x$						$MnCo_2O_4$
$MnNiZnO_x$						Ni_6MnO_8, NiO
$FeCoNiO_x$	–	33	33	33	–	$NiFe_2O_4$, $CoFe_2O_4$, $NiCo_2O_4$
$FeCoZnO_x$	–	33	33	–	33	Fe_2O_3, ZnO
$FeNiZnO_x$						Fe_3O_4, ZnO
$CoNiZnO_x$	–	–	33	33	33	$CoNiO_2$, $ZnCo_2O_4$, ZnO

It has been well documented that catalyst preparation and processing may affect electrochemical performance[24-27]. To minimize synthetic effects, all oxides for this survey were prepared by the very combustion methodology[22]. In general, this method yields highly homogeneous materials corresponding to the thermodynamically stable phases for each composition (Table 4.2), and allegedly avoiding the presence of minor phases that may be catalytically active. The phase of the MO_x, $MM'O_x$ and $MM'M''O_x$ oxides (25

in total) were measured by the X-ray powder diffractometer and determined with Powder Diffraction File (PDF) cards (Figure 4.2-4.5). According to structural data, most of the materials contained single crystalline phases (Table 4.2) with few exceptions.

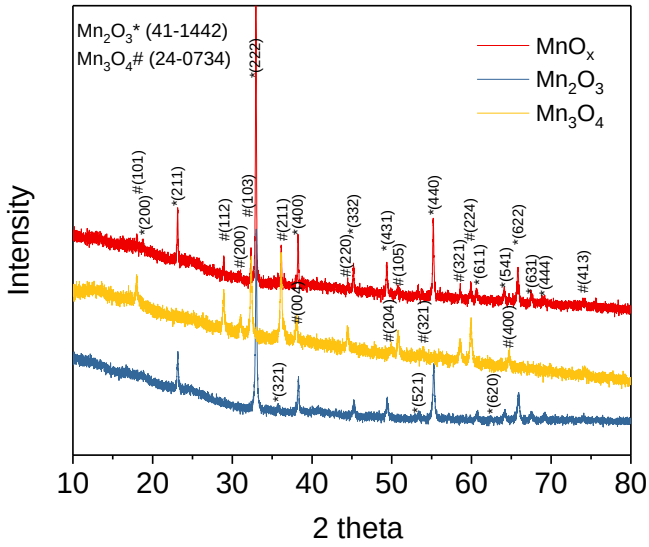

Figure 4.2. PXRD pattern for MnO_x, Mn_2O_3 and Mn_3O_4.

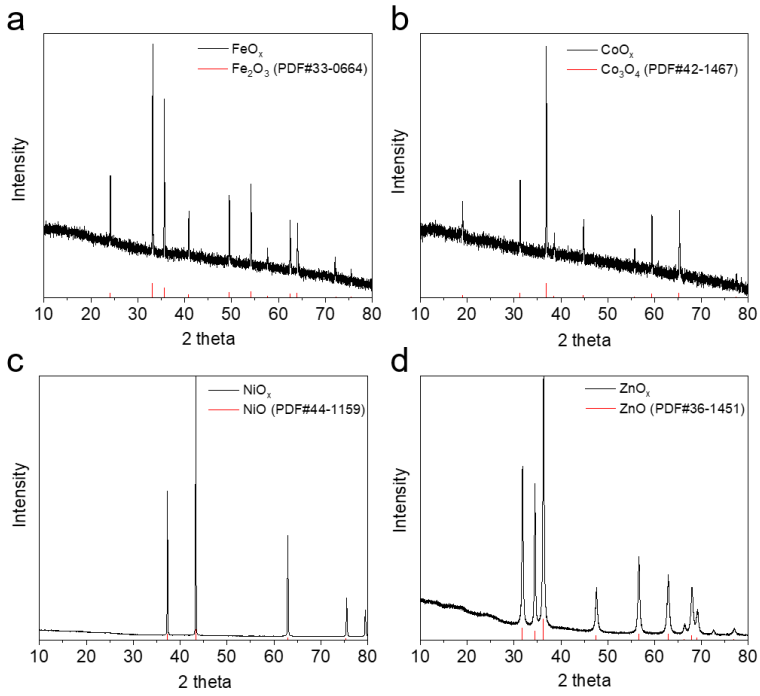

Figure 4.3. PXRD pattern for (a) FeO_x, (b) CoO_x, (c) NiO_x, (d) ZnO_x.

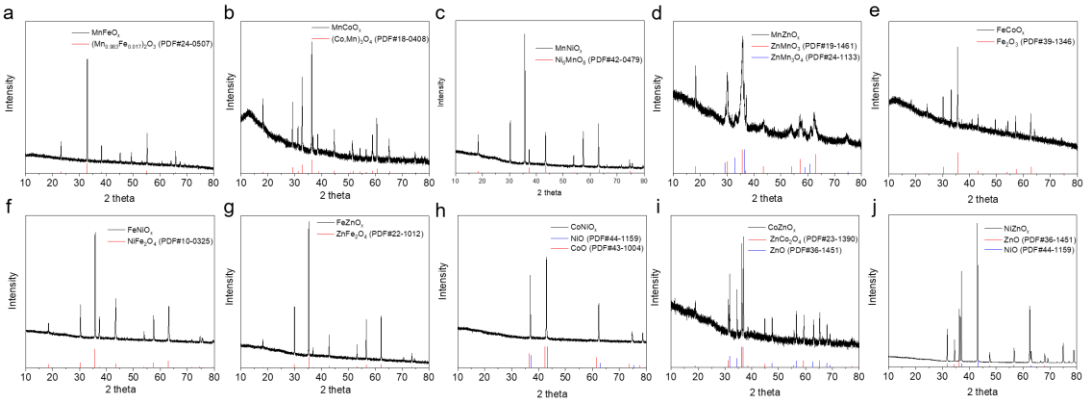

Figure 4.4. PXRD pattern for (a) $MnFeO_x$, (b) $MnCoO_x$, (c) $MnNiO_x$, (d) $MnZnO_x$, (e) $FeCoO_x$, (f) $FeNiO_x$, (g)$FeZnO_x$, (h) $CoNiO_x$, (i) $CoZnO_x$, (j) $NiZnO_x$.

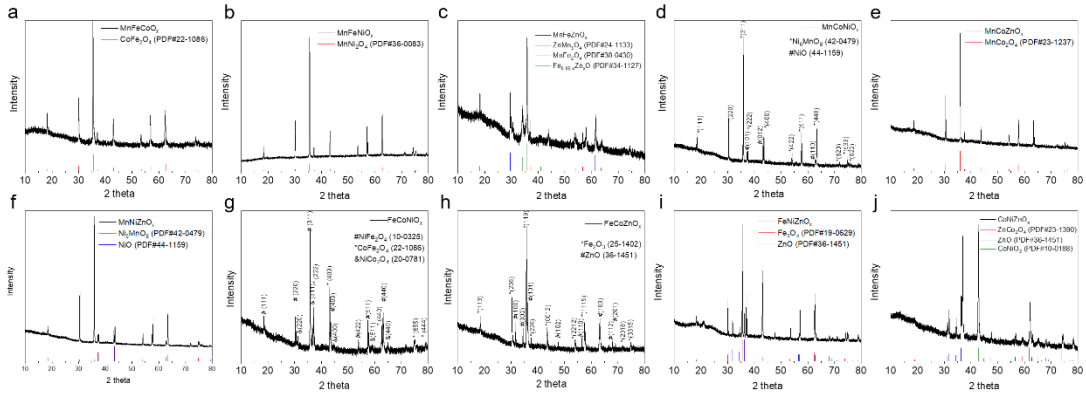

Figure 4.5. PXRD pattern for (a) $MnFeCoO_x$, (b) $MnFeNiO_x$, (c) $MnFeZnO_x$, (d) $MnCoNiO_x$, (e) $MnCoZnO_x$, (f) $MnNiZnO_x$, (g)$FeCoNiO_x$, (h) $FeCoZnO_x$, (i) $FeNiZnO_x$, (j) $CoNiZnO_x$.

To prepare the anodes, the oxides were mixed with graphite (G) and paraffin oil (PO) in the desired ratio (see **Experimental sections**) to obtain homogeneous composites (MO_x/GPO, $MM'O_x$/GPO and $MM'M''O_x$/GPO) to be inserted into the pocket of working electrodes.

4.3.2. Comparative OER performance

We applied the same experimental protocol to collect the linear sweep voltammetry (LSV) for all of the oxide electrodes in 1 M H_2SO_4 electrolyte (Figure 4.6). In the monometallic series, we observed that MnO_x shows a pre-catalytic event, that we assigned to a Mn^{3+}/Mn^{4+} oxidation (Figure 4.6a). MnO_x@GPO offered the best voltage efficiency, reaching ≈ 50 mA cm^{-2} at 1.73 V although the pre-catalytic event does not allow to directly estimate the onset potential. All other oxides showed onset potentials > 1.55 V (vs RHE) with current densities below ≈ 20 mA cm^{-2} at 1.73 V (Figure 4.6b, Table 4.2), with decreasing activity as: Co > Fe > Zn > Ni. The H_2SO_4 electrolyte has no metallic impurities, precluding Fe uptake, well known to enhance the activity of NiO_x phases[28].

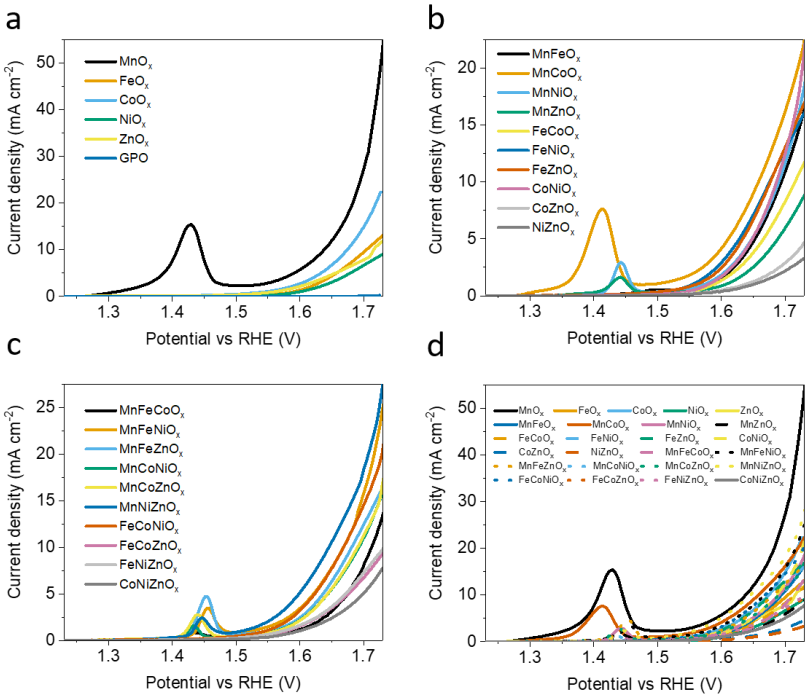

Figure 4.6. LSV curves in 1 M H_2SO_4 electrolyte (pH 0.1) with 1 mV s^{-1} scan rate of (a) MO_x/GPO, (b) MM'O_x/GPO, (c) MM'M''O_x/GPO and (d) all prepared electrodes.

In the bimetallic oxides series, the best activity was found for the $MnCoO_x$, reaching ≈20 mA cm^{-2} at 1.73 V (Figure 4.6b), still far from the activity found in MnO_x/GPO electrodes. Meanwhile, pre-catalytic oxidation peaks were found for all Mn-containing catalysts. The rest of the series exhibited lower performance (Table 4.3). The FeNi oxide, which is regarded as most efficient OER electrocatalysts in alkaline media, appeared to offer the second-best performance in these conditions, almost identical to $FeZnO_x$, suggesting again the positive effect of Zn centers towards OER[29,30].

The trimetallic series (Figure 4.6c), followed the same trend. With the appearance of a pre-catalytic event in Mn-containing oxides. In this case, the highest activity was found for $MnNiZnO_x$, reaching 27 mA cm^{-2} at 1.73 V, isostructural to the $FeNiZnO_x$ analogue, which showed the highest performance in alkaline OER[30]. Still, no other materials exhibited an

electrocatalytic OER performance close to MnO_x/GPO electrodes (Figure 4.6d).

Table 4.3. Electrochemical parameters for the different metal oxide/GPO electrodes. From linear sweep voltammetry: overpotential (η_{10}) to reach j = 10 mA cm^{-2} and current density (j_{500}) at 500 mV overpotential (≈ 1.73 V vs RHE). From chronopotentiometry under j = 10 mA cm^{-2}: initial overpotential ($\eta_{t=0.1h}$) and overpotential after 2 h ($\eta_{t=2h}$).

Electrode	η_{10} (V) @ 10 mA cm^{-2}	j_{500} (mA cm^{-2}) @ η = 500 mV	$\eta_{t=0.1h}$ (V)	$\eta_{t=2\ h}$ (V)
MnO_x	0.407	52	0.421	0.425
FeO_x	0.473	13	0.544	0.536
CoO_x	0.443	22	0.468	0.466
NiO_x	~	9	0.596	0.604
ZnO_x	0.486	12	0.582	0.591
$MnFeO_x$	0.465	17	0.485	0.466
$MnCoO_x$	0.427	22	0.469	0.470
$MnNiO_x$	0.459	18	0.488	0.480
$MnZnO_x$	~	9	0.546	0.488
$FeCoO_x$	0.485	11	0.550	0.537
$FeNiO_x$	0.448	16	0.537	0.548
$FeZnO_x$	0.446	17	0.507	0.521
$CoNiO_x$	0.454	20	0.496	0.488
$CoZnO_x$	~	5	0.565	0.528
$NiZnO_x$	~	3	0.617	0.588
$MnFeCoO_x$	0.484	13	0.499	0.478
$MnFeNiO_x$	0.437	24	0.467	0.462
$MnFeZnO_x$	0.453	16	0.511	0.476
$MnCoNiO_x$	0.462	16	0.502	0.477
MnCoZnO	0.462	17	0.497	0.468
x				
$MnNiZnO_x$	0.417	27	0.472	0.470
$FeCoNiO_x$	0.437	20	0.487	0.516
$FeCoZnO_x$	~	9	0.537	0.518
$FeNiZnO_x$	~	10	0.568	0.564
$CoNiZnO_x$	~	8	0.558	0.533
Mn_2O_3	0.309	97	0.358	0.365
Mn_3O_4	~	64	0.438	0.432

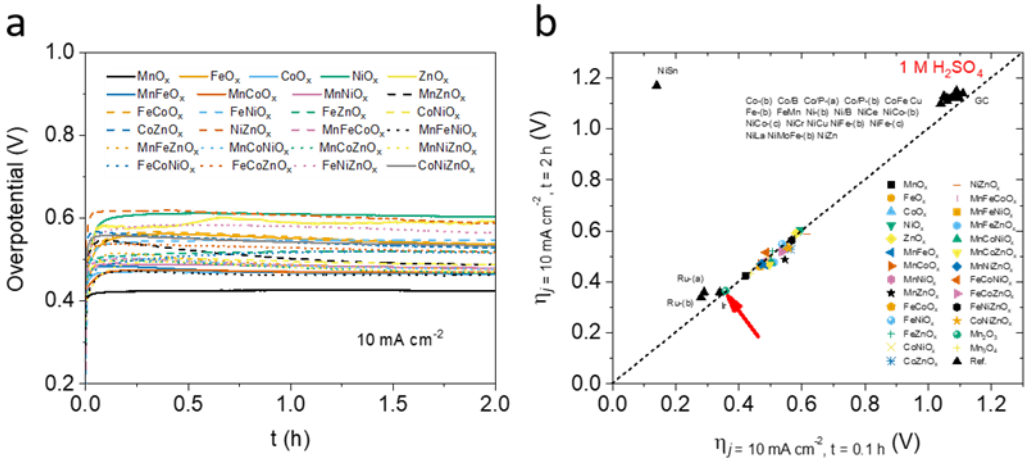

Figure 4.7. (a) stability tests of the MO_x/GPO, $MM'O_x$/GPO and $MM'M''O_x$/GPO electrodes in chronopotentiometry measurements at 10 mA cm^{-2} in 1 M H_2SO_4 electrolyte; (b) benchmarking of the activity/stability features according to the study of Jaramillo et al.[6].

Beyond activity, stability is a crucial feature required for OER electrocatalysts. We applied the benchmarking protocol proposed by Jaramillo et al.[6,31], to address this issue, comparing the evolution of overpotential during a 2 h chronopotentiometry at 10 mA cm^{-2}. The results for the most active electrodes are shown in Figure 4.7a, with their benchmarking comparison with other electrocatalysts in recent literature (Figure 4.7b). We found good stability for all oxides examined in this survey, suggesting the validity of the approach: a partially hydrophobic binder/surface confers great stability to (almost) all metal oxides during OER in extremely acidic conditions, opening an interesting strategy towards future applications. Some oxides (such as $MnZnO_x$, $CoZnO_x$) actually improved their activity during the tests. We then selected MnO_x@GPO as the model electrode for further studies, to better define structure/performance correlations.

4.3.3. OER with Mn oxides in 1 M H_2SO_4

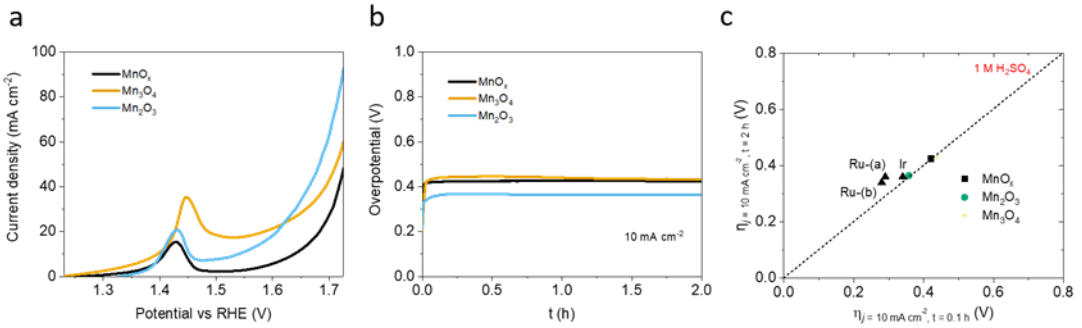

Figure 4.8. (a) electrocatalytic activity of MnO_x/GPO, Mn_3O_4/GPO and Mn_2O_3/GPO; (b) stability tests of MnO_x/GPO, Mn_3O_4/GPO and Mn_2O_3/GPO in chronopotentiometry measurements at 10 mA cm^{-2}; (c) benchmarking of the activity/stability features between our Mn-based oxide and noble metal-based electrocatalysts according to the study of Jaramillo et al.[6].

As described before (Table 4.2 and Figure 4.2), the MnO_x obtained with our standardized synthetic method was indeed a mixture of two crystalline phases, Mn_2O_3 and Mn_3O_4. We prepared the Mn_2O_3 and Mn_3O_4 single phases to identify their actual OER catalytic activity. We used two different synthetic protocols to obtain pure phases of each. GPO electrodes were prepared and characterized following the same previous protocols.

The LSV data confirmed that Mn_2O_3/GPO offered significantly better OER activity with higher current density of > 80 mA cm^{-2} at 1.72 V (Figure 4.8a). This better performance might be partially due to the higher density of active sites found in Mn_2O_3/GPO. The electrochemical double-layer capacitance (EDLC) were calculated as 29 and 10 mF cm^{-2} for Mn_2O_3/GPO and Mn_3O_4/GPO respectively (Figure 4.9), respectively. In addition, intrinsically faster performance could also be assigned to the Mn_2O_3/GPO, since it exhibited a lower Tafel slope of 144 mV dec^{-1} than 176 mV dec^{-1} for Mn_3O_4 (Figure 4.10), which was independent of the number of available active sites. It was interesting to confirm that the MnO_x@GPO electrodes showed an intermediate Tafel slope (154 mV dec^{-1}), as expected for a mixture of the two phases.

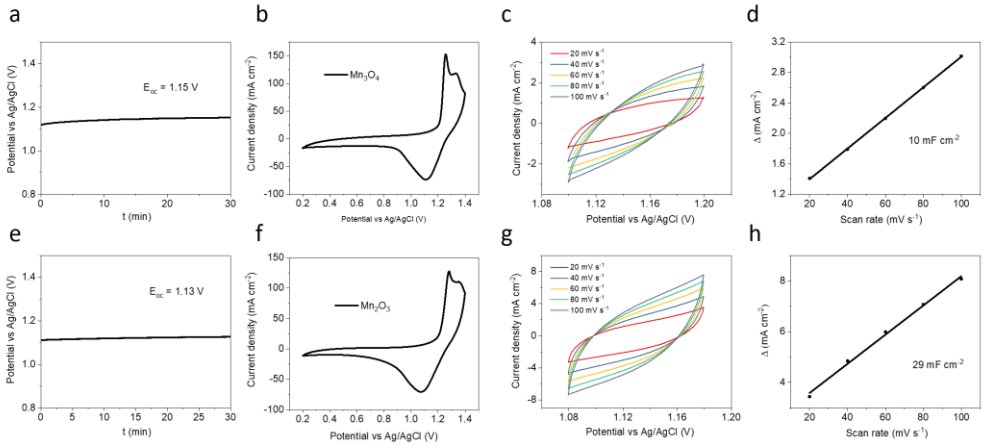

Figure 4.9. Electrochemical double-layer capacitance (EDLC) measurements: OCP (vs Ag/AgCl) values recording within 30 mins of (a) Mn_3O_4/GPO and (e) Mn_2O_3/GPO; CV curves under 10 mV s^{-1} scan rate of (b) Mn_3O_4/GPO and (f) Mn_2O_3/GPO; CV curves under different scan rates of (c) Mn_3O_4/GPO and (g) Mn_2O_3/GPO; The scan rate dependences of the current density differences Δ of (d) Mn_3O_4/GPO and (h) Mn_2O_3/GPO.

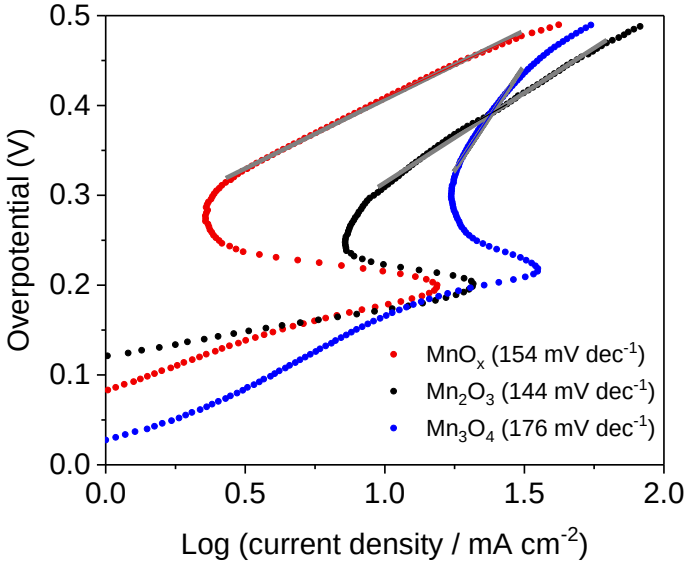

Figure 4.10. Tafel plots of MnO_x/GPO, Mn_2O_3/GPO and Mn_3O_4/GPO extracted from LSV data.

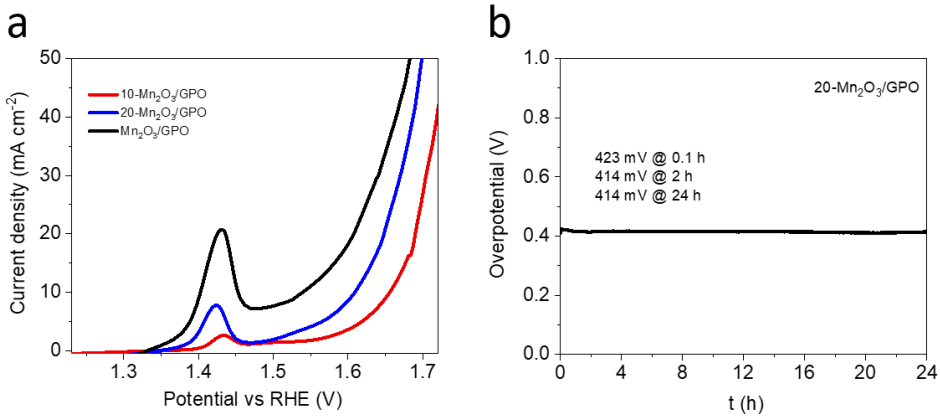

Figure 4.11. (a) electrocatalytic activity of Mn_2O_3/GPO, 10-Mn_2O_3/GPO and 20-Mn_2O_3/GPO; (b) stability tests of 20-Mn_2O_3/GPO in chronopotentiometry measurements at 10 mA cm^{-2} for 24 h.

In addition, applying the 2 h at 10 mA cm^{-2} benchmarking protocol, Mn_2O_3/GPO just needed a stable, low overpotential of ≤365 mV, comparable to the performance of noble metal (Figure 4.8b and 4.8c). Even when we decreased the amount of Mn_2O_3 addition in the composite, it also showed high performance for 20-Mn_2O_3/GPO, catalyzing OER with ≤423 mV overpotentials to deliver the current density of 10 mA cm^{-2} for 24 h without any evident changes (Figure 4.11). Stability number (*S*-number) and Activity-Stability Factor (ASF) were also proposed as key metrics for estimating lifetime and long-term stability for electrocatalysts[32,33]. Thus, we analyzed the electrolyte after stability tests to check for Mn leaching (Table 4.4). We found the presence of Mn but at the ppb level, corresponding to just ≈ 0.38 % of the total. Based on this number, we can estimate a 130 *S*-number, an ASF of 52 and a lifetime of 3914 h. These estimations are comparable to noble metal-based catalysts in analogous conditions, and confirm the promising performance/stability of these electrodes.

Finally, we measured anodic oxygen evolution during chronopotentiometry experiments with Mn_2O_3/GPO electrodes (Figure 4.12). >99% of Faradaic efficiency was obtained, confirming that the dominant catalysis process was the OER in these conditions.

Table 4.4. Elemental analysis (ICP-MS) of manganese before and after 2 h electrocatalytic water oxidation at a constant current density of 10 mA cm^{-2} in 1 M H_2SO_4 of 40 mL.

	Mn amount (μg/L)
1 M H_2SO_4 before	–
1 M H_2SO_4 after	102

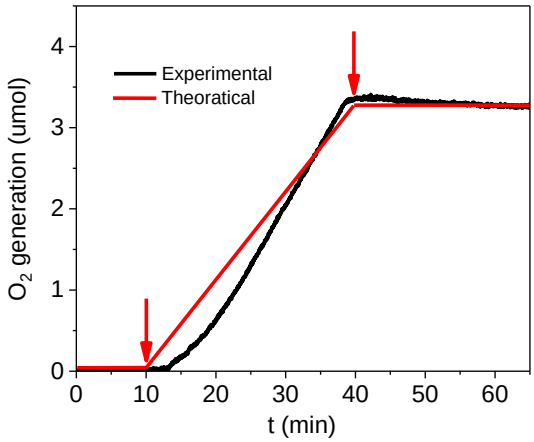

Figure 4.12. Time evolution of oxygen production amount in the anode headspace during a chronopotentiometry at the constant current density of 10 mA cm^{-2} for 30 minutes. The arrows indicate initial and final electrolysis times. 3 mins after the chronopotentiometry starts, the O_2 signal rapidly increases, reaching a total ~3.26 umol production of O_2 in steady state conditions. This corresponds to a >99% Faradaic efficiency.

4.3.4. Post-electrolysis Mn_2O_3/GPO characterization

We characterized the structural and chemical evolution of the **Mn_2O_3/GPO** electrode s after these 2 h electrolysis at 10 mA cm^{-2} in 1 M H_2SO_4, further confirming the stability of Mn_2O_3 as a genuine OER catalyst. The PXRD patterns did not show any significant change nor shift in the observed peaks, still typical Mn_2O_3 (Figure S4.31). This suggests no evident structural changes are occurring to the bulk of the material Mn_2O_3.

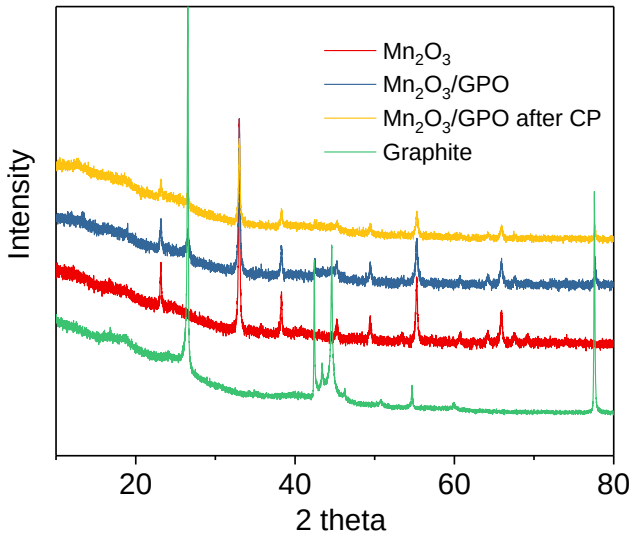

Figure 4.13. PXRD patterns of commercial graphite, Mn_2O_3, Mn_2O_3/GPO and Mn_2O_3/GPO after 2h catalysis (washed with acetone to remove paraffin oil).

We also investigated the Mn_2O_3/GPO composite after 2 h electrolysis at 10 mA cm^{-2} by means of HRTEM (Figure 4.14). The HRTEM images and STEM-EELS analyses also confirmed a high structural and chemical stability (Figure 4.15-4.). As we can observe in Figure 3a, the NPs still have the orthorhombic Pcab α-Mn2O3 atomic structure (S.G.: 61) imaged along its [101] zone axis. The presence of crystalline graphite has been also evidenced with the 2H oriented structure along its [0001] zone axis. In Figure 3b both a top and side views are reported and highlighted in the frequency filtered map, in red and yellow respectively. In Figure 3c the STEM-HAADF image and STEM_EELS analysis is reported observing that the elements are homogeneously distributed confirming the atomic ratio evaluated from the HRTEM analysis. The crystalline nature of the graphite is also evidenced as it has been possible to extrapolate its contribution from the amorphous C arising from the TEM grid support. By comparing the HRTEM and STEM-EELS analysis from all the investigated samples we can observe

that neither crystallinity nor particle size are affected by the electrochemical process.

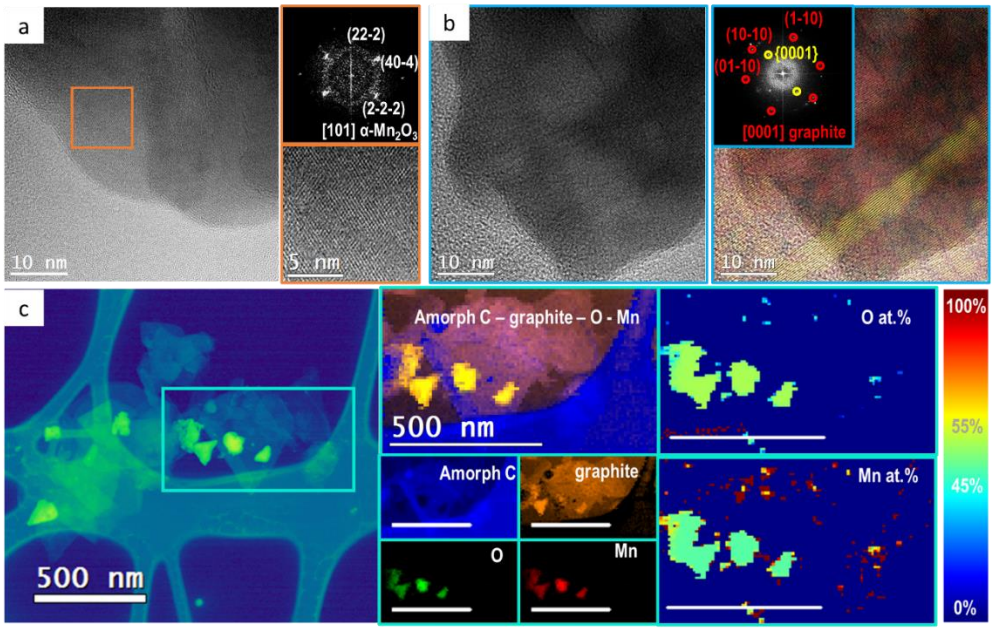

Figure 4.14. (a) HRTEM general image of a Mn_2O_3 nanocrystal, with a magnified view on the bottom right and its corresponding indexed power spectrum. (b) HRTEM image showing the lattice fringes corresponding to the graphite-like structures. On the right side we present an indexed power spectrum from the same area, superposed to the obtained frequency filtered image where the found graphitic structures are shown in red and yellow, respectively. (c) False color HAADF STEM general view and the corresponding EELS composition maps. On the right side we show the percentage composition for both Mn and O.

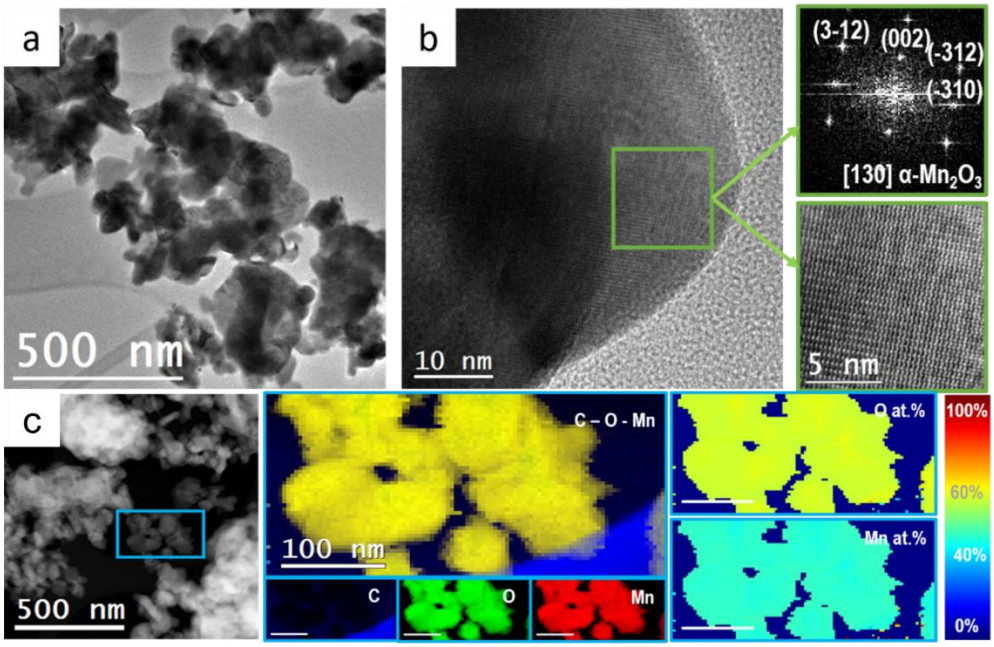

Figure 4.15. Low mag TEM (a) and HRTEM (b) micrographs from as-prepared Mn_2O_3. It was found that the NPs possess orthorhombic Pcab α-Mn2O3 phase (S.G.: 61) here imaged along its [130] zone axis. (c) STEM-HAADF and STEM-EELS analysis of as-prepared Mn_2O_3 considering C K edge at 284 eV (blue), O K edge at 532 eV (green) and Mn L edge at 640 eV (red). All the Mn nanoparticles are fully oxidized, confirming the stoichiometry found from HRTEM. Carbon signal comes from the support, a lacey carbon with an ultrathin carbon layer supported on a Cu mesh, from Ted Pella. (all scale bars correspond to 100 nm).

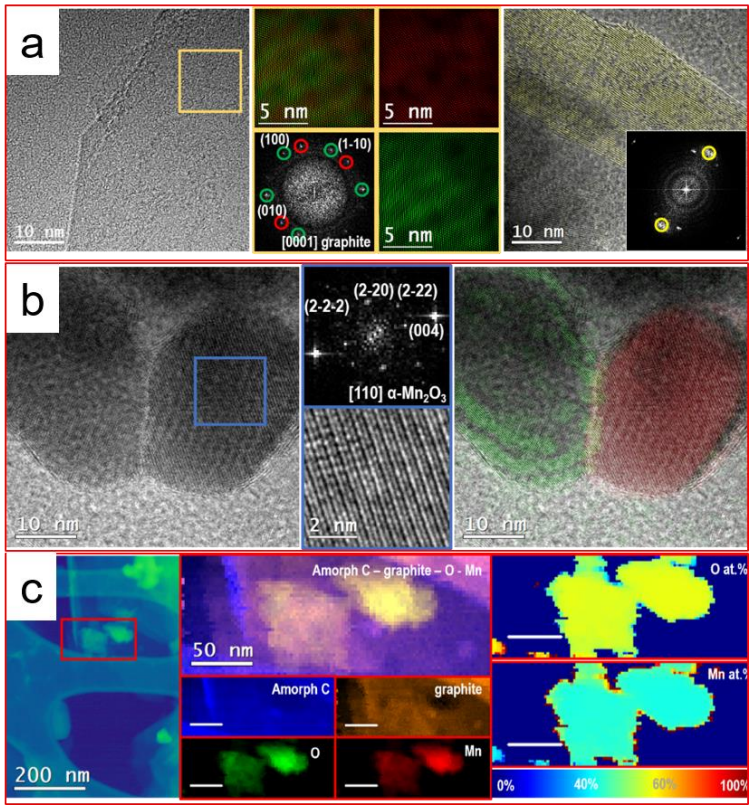

Figure 4.16. (a) HRTEM analysis of Mn_2O_3/GPO. We could identify the presence of crystalline graphite, as here evidenced. In particular, from the power spectrum analysis we can distinguish two layers 22° rotated one with respect to the other, in red and green, respectively. Here the structure is 2H oriented along its [0001] zone axis. In the image on the right the graphite is imaged along the side, evidencing an interplanar distance of around 3.4 nm. (b) HRTEM analysis of Mn_2O_3/GPO. The NPs posses orthorhombic Pcab α-Mn_2O_3 atomic structure (sg 61) here imaged along its [110] zone axis. Here the presence of two nanoparticles possessing the same atomic structure is highlighted in the frequency filtered map reported on the right side in green and red, respectively. (c) STEM-HAADF and STEM-EELS analysis of Mn_2O_3/GPO considering C K edge at 284 eV (blue), O K edge at 532 eV (green) and Mn L edge at 640 eV (red). We could separate the graphitic typical peak arising from C edge, from the C amorphous from the TEM grid support. All the Mn nanoparticles are fully oxidized, confirming the stoichiometry evaluated in HRTEM (all scale bars correspond to 50 nm).

4.3.5. Conclusions

In summary, we have carried out a survey of earth abundant transition metal oxides as oxygen evolution electrocatalysts under acidic conditions using a conductive and partially hydrophobic support to confer them good stability. This reliable strategy has allowed us to compare their electrochemical performance despite their intrinsic instability. Among the 25 oxides tested, Mn_2O_3-based anodes successfully passed the benchmarking protocol in acidic media and were able to deliver 10 mA cm^{-2} in 1 M sulfuric acid solution (pH < 0.1) at very low overpotential of $\eta < 365$ mV. Besides, the critical role of Mn doping was also found to greatly improve the acidic OER performance. These comprehensive and interesting findings would be helpful in the exploitation of earth-abundant electrocatalysts for acidic OER.

4.4. References

1. Seh, Z. W. *et al.* Combining theory and experiment in electrocatalysis: Insights into materials design. *Science* **80**, 355 (2017).
2. Nnabuife, S. G., Ugbeh-Johnson, J., Okeke, N. E. & Ogbonnaya, C. Present and Projected Developments in Hydrogen Production: A Technological Review. *Carbon Capture Sci. Technol.* **3,** 100042 (2022).
3. Chen, Z. *et al.* Advances in Oxygen Evolution Electrocatalysts for Proton Exchange Membrane Water Electrolyzers. *Adv. Energy Mater.* **2103670,** 1–47 (2022).
4. Ding, H., Liu, H., Chu, W., Wu, C. & Xie, Y. Structural Transformation of Heterogeneous Materials for Electrocatalytic Oxygen Evolution Reaction. *Chem. Rev.* **121,** 13174–13212 (2021).
5. Yu, J., Cheng, G. & Luo, W. Hierarchical NiFeP microflowers directly grown on Ni foam for efficient electrocatalytic oxygen evolution. *J. Mater. Chem. A* **5,** 11229–11235 (2017).
6. McCrory, C. C. L. *et al.* Benchmarking Hydrogen Evolving Reaction and Oxygen Evolving Reaction Electrocatalysts for Solar Water Splitting Devices. *J. Am. Chem. Soc.* **137,** 4347–4357 (2015).

7. Gong, M. & Dai, H. A mini review of NiFe-based materials as highly active oxygen evolution reaction electrocatalysts. *Nano Res.* **8,** 23–39 (2015).
8. Spöri, C., Kwan, J. T. H., Bonakdarpour, A., Wilkinson, D. P. & Strasser, P. The Stability Challenges of Oxygen Evolving Catalysts: Towards a Common Fundamental Understanding and Mitigation of Catalyst Degradation. *Angew. Chemie - Int. Ed.* **56,** 5994–6021 (2017).
9. Reier, T., Nong, H. N., Teschner, D., Schlögl, R. & Strasser, P. Electrocatalytic Oxygen Evolution Reaction in Acidic Environments – Reaction Mechanisms and Catalysts. *Adv. Energy Mater.* **7,** 1601275 (2017)
10. Lei, Z. *et al.* Recent Progress in Electrocatalysts for Acidic Water Oxidation. *Adv. Energy Mater.* **10,** 1–18 (2020).
11. Liu, Y. *et al.* Iridium-containing water-oxidation catalysts in acidic electrolyte. *Chinese J. Catal.* **42,** 1054–1077 (2021).
12. Moreno-Hernandez, I. A. *et al.* Crystalline nickel manganese antimonate as a stable water-oxidation catalyst in aqueous 1.0 M H_2SO_4. *Energy Environ. Sci.* **10,** 2103–2108 (2017).
13. Chatti, M. *et al.* Intrinsically stable in situ generated electrocatalyst for long-term oxidation of acidic water at up to 80 °C. *Nat. Catal.* **2,** 457–465 (2019).
14. Li, A. *et al.* Enhancing the stability of cobalt spinel oxide towards sustainable oxygen evolution in acid. *Nat. Catal.* **5,** 109–118 (2022).
15. Pan, S. *et al.* Efficient and stable noble-metal-free catalyst for acidic water oxidation. *Nat. Commun.* **13,** 1–10 (2022).
16. Huang, J., Sheng, H., Ross, R.D. *et al.* Modifying redox properties and local bonding of Co_3O_4 by CeO_2 enhances oxygen evolution catalysis in acid. *Nat Commun* **12**, 3036 (2021).
17. Blasco-Ahicart, M., Soriano-Lopez, J., Carbo, J. J., Poblet, J. M. & Galan-Mascaros, J. R. Polyoxometalate electrocatalysts based on earthabundant metals for efficient water oxidation in acidic media. *Nat. Chem.* **10,** 24–30 (2018).
18. Yu, J., Garcés-Pineda, F.A., González-Cobos, J. *et al.* Sustainable oxygen evolution electrocatalysis in aqueous 1 M H_2SO_4 with earth abundant nanostructured Co_3O_4. *Nat Commun* **13**, 4341 (2022).

19. Etzi Coller Pascuzzi, M., van Velzen, M., Hofmann, J. P. & Hensen, E. J. M. On the Stability of Co3O4 Oxygen Evolution Electrocatalysts in Acid. *ChemCatChem* **13,** 459–467 (2021).
20. Zhou, L. *et al.* Rutile Alloys in the Mn-Sb-O System Stabilize Mn^{3+} to Enable Oxygen Evolution in Strong Acid. *ACS Catal.* **8,** 10938–10948 (2018).
21. Bloor, L. G., Molina, P. I., Symes, M. D. & Cronin, L. Low pH electrolytic water splitting using earth-abundant metastable catalysts that self-assemble in situ. *J. Am. Chem. Soc.* **136,** 3304–3311 (2014).
22. Chen, J. Y. C., Miller, J. T., Gerken, J. B. & Stahl, S. S. Inverse spinel $NiFeAlO_4$ as a highly active oxygen evolution electrocatalyst: Promotion of activity by a redox-inert metal ion. *Energy Environ. Sci.* **7**, 1382–1386 (2014).
23. Morales, D. M. & Risch, M. Seven steps to reliable cyclic voltammetry measurements for the determination of double layer capacitance. *J. Phys. Energy* **3,** 34013 (2021).
24. Govind Rajan, A., Martirez, J. M. P. & Carter, E. A. Why Do We Use the Materials and Operating Conditions We Use for Heterogeneous (Photo)Electrochemical Water Splitting? *ACS Catal.* **10,** (2020).
25. Wang, P. & Wang, B. Designing Self-Supported Electrocatalysts for Electrochemical Water Splitting: Surface/Interface Engineering toward Enhanced Electrocatalytic Performance. *ACS Appl. Mater. Interfaces* **13,** 59593–59617 (2021).
26. Xu, Q. *et al.* Atomic heterointerface engineering overcomes the activity limitation of electrocatalysts and promises highly-efficient alkaline water splitting. *Energy Environ. Sci.* **14,** 5228–5259 (2021).
27. Li, S. *et al.* Transition metal-based bimetallic MOFs and MOF-derived catalysts for electrochemical oxygen evolution reaction. *Energy Environ. Sci.* **14,** 1897–1927 (2021).
28. Trotochaud, L., Young, S. L., Ranney, J. K. & Boettcher, S. W. Nickel-Iron oxyhydroxide oxygen-evolution electrocatalysts: The role of intentional and incidental iron incorporation. *J. Am. Chem. Soc.* **136,** 6744–6753 (2014).
29. Zhou, L., Zhang, C., Zhang, Y., Li, Z. & Shao, M. Host Modification of Layered Double Hydroxide Electrocatalyst to Boost the

Thermodynamic and Kinetic Activity of Oxygen Evolution Reaction. *Adv. Funct. Mater.* **31,** 1–9 (2021).

30. Garcés-Pineda, F. A. *et al.* Push-Pull Electronic Effects in Surface-Active Sites Enhance Electrocatalytic Oxygen Evolution on Transition Metal Oxides. *ChemSusChem* **14,** 1595–1601 (2021).
31. McCrory, C. C. L., Jung, S., Peters, J. C. & Jaramillo, T. F. Benchmarking heterogeneous electrocatalysts for the oxygen evolution reaction. *J. Am. Chem. Soc.* **135**, 16977–16987 (2013).
32. Geiger, S. *et al.* The stability number as a metric for electrocatalyst stability benchmarking. *Nat. Catal.* **1,** 508–515 (2018).
33. Kim, Y. T. *et al.* Balancing activity, stability and conductivity of nanoporous core-shell iridium/iridium oxide oxygen evolution catalysts. *Nat. Commun.* **8,** 1–8 (2017).

Chapter 5. General conclusion

PEM electrolyzer is one of the the most promising and sustainable technologies for hydrogen production. Proton-rich environment is favorable for hydrogen evolution reaction on the cathode but a challenge for oxygen evolution reaction on the anode. To lower the cost of PEM electrolyzer for large-scale application, it is necessary to develop efficient electrocatalytic materials based on inexpensive elements.

In the terms of HER, non-noble transition metal-based electrocatalysts have been widely researched and reported as alternate and economically viable catalysts using diverse techniques to optimize electrocatalytic property. Material heterostructuring is considered as a most effective approach. In **chapter 2**, we introduced a viable strategy to anchor Co containing POM molecular catalysts on 2D MXene nanosheets with high surface area and good conductivity. With the help of this unique heterostructure, the composite showed Pt-like activity and excellent stability.

A variety of efficient OER electrocatalysts based on low-cost materials, could work well in alkaline media but would lose their high activities and be dissolved in acid under high potentials. To solve this problem, in the **Chapter 3**, we present a promising processing protocol, incorporating a highly active nanostructured MOF-derived OER catalyst from earth-abundant metals and a conducting, partially hydrophobic protection binder into one anode. It exhibited superb acidic OER performances with high activity, selectivity and excellent stability, comparable to those of IrO_2.

In the **Chapter 4**, we have been able to conduct an extensive survey of the activity and stability of monometallic, binary and ternary earth-abundant transition metal oxides during electrocatalytic OER in acidic conditions. Our results confirm the general validity of the processing strategy in using a partially hydrophobic electrode to confer high stability to common metal oxides under these harsh conditions. These comprehensive and interesting findings would be helpful in the exploitation of earth-abundant electrocatalysts for acidic OER.


UNIVERSITAT
ROVIRA i VIRGILI


ICIQ
Institute
of Chemical
Research
of Catalonia